Dissertation
submitted to the
Combined Faculties for the Natural Sciences and for Mathematics
of the Ruperto-Carola University of Heidelberg, Germany
for the degree of
Doctor of Natural Sciences

presented by
Dipl.-Phys. Hjalmar Bruhns
born in Heidelberg

Oral examination: 21.12.2005

High precision x-ray spectroscopy on highly charged argon ions

Referees: Prof. Dr. Joachim Ullrich
Prof. Dr. Dirk Schwalm

Zusammenfassung:

In dieser Arbeit wurden Hochpräzisionsmessungen der Wellenlängen der $1s2s\ ^3S_1 \rightarrow 1s^2\ ^1S_0$ ("z") und $1s2p\ ^1P_1 \rightarrow 1s^2\ ^1S_0$ ("w") Übergänge in Ar^{16+}, sowie des Lyman-α_1 Übergangs in Cl^{16+} unter Nutzung der Lyman-α_1 Übergangswellenlänge in Ar^{17+} als Referenz mit einem neuen Flachkristallröntgenspektrometer an der Heidelberg Elektronenstrahlionenfalle (HD-EBIT) durchgeführt. Ein neuartiges, hochpräzises Verfahren zur Braggwinkelbestimmung wurde entwickelt, welches zwei Strahlen sichtbaren Lichts zur Feststellung des Reflektionsorts der Röntgenstrahlung nutzt, wodurch der Gebrauch von Eingangsspalten vermieden wird, durch welche sonst ein nicht hinnehmbarer Verlust an Röntgenstrahlung durch Kollimation entstünde. Relative Genauigkeiten besser als $\Delta\lambda/\lambda < 10^{-5}$ wurden für die Messung aller drei Linien erzielt. Die gemessene Energie des Cl^{16+} Lyman-α_1 Übergangs ist in hervorragender Übereinstimmung mit der theoretischen Vorhersage sowie früheren experimentellen Arbeiten, jedoch 4 mal genauer. Die Energie des z-Übergangs, welche nie zuvor in Argon gemessen wurde, stimmt mit den Vorhersagen innerhalb des Fehlerbalkens überein. Die w-Übergangsenergie, obschon doppelt so genau wie und in hervorragender Übereinstimmung mit früheren experimentellen Werten, weicht von der Vorhersage um mehr als 2σ ab und deutet auf deren Unvollständigkeit hin.

Abstract:

High-precision wavelength measurements on the $1s2s\ ^3S_1 \rightarrow 1s^2\ ^1S_0$ ("z") and $1s2p\ ^1P_1 \rightarrow 1s^2\ ^1S_0$ ("w") transitions in Ar^{16+} as well as of the Lyman-α_1 transition in Cl^{16+} with respect to the Lyman-α_1 transition in Ar^{17+} were carried out, using a new flat crystal spectrometer installed at the Heidelberg electron beam ion trap (HD-EBIT). A novel, highly accurate technique of Bragg-angle determination was developed, employing two beams of visible light reflected on the x-ray crystal to mark the x-ray reflection position. The need for collimating entrance slits causing unacceptable x-ray flux losses is thereby avoided. Relative uncertainties of better than $\Delta\lambda/\lambda < 10^{-5}$ were achieved in the measurement of all three lines. The measured Cl^{16+} Lyman-α_1 transition energy is in perfect agreement with the theoretical prediction and previous experimental work, however 4 times more accurate. The z transition energy, never measured before in argon, agrees with predictions within its error bar. The w transition energy, while in perfect agreement with but two times more accurate than earlier experimental results, disagrees with by 2σ with predictions, pointing at their possible incompleteness.

Contents

Introduction

X-rays play an important role in a large variety of applications. Their ability to penetrate deeply into matter in combination with the strong dependence of their absorption on the material makes them an unique tool for high-contrast transillumination imaging, as used *e.g.* in medicine and for material analysis. In addition, this method is largely non-destructive, making it an important technique to study invaluable ancient objects and, by using x-ray diffraction techniques even old, once erased layers in reused paintings and books can be revealed. In biology their short wavelength allows high resolution microscopy, e.g. to investigate the inner structures of cells, and x-ray protein structure determination at modern synchrotrons has become a standard tool. X-rays emitted by astrophysical plasmas shed light on the composition and temperature of stars and cosmic nebulae. With x-ray spectroscopy, the distribution of elements in matter as well as the atomic structure can be determined. This versatility makes x-rays one of the most important tools for many research fields like material science, biology, chemistry and physics and, consequently, sources of ever increasing brilliance like 3rd generation synchrotrons or free-electron x-ray lasers, planned at Hamburg and Stanford, are continuously being developed.

Wilhelm Conrad Röntgen described his discovery of x-rays in 1895 in a publication in Würzburg's Physical-Medical Society journal. The importance of his findings for medical purposes was soon realized, and Röntgen was the first to be awarded the Nobel Prize in physics in 1901. In 1912 Max von Laue simultaneously proved the symmetrical atomic arrangement in crystals and that x-rays are part of the electromagnetic spectrum by studying their diffraction in crystals, for which he received the Nobel Prize in 1914. William L. Bragg and his father were given this honour in 1915 for the description of the diffraction process, commonly known as Bragg's law, and for laying the foundation of crystallography and crystal x-ray spectroscopy. Even after more than 90 years the crystal spectrometer is still the most commonly used tool for high-precision x-ray measurements in the energy region of $1 - 10\,\mathrm{keV}$. X-ray spectroscopy is mainly used for chemical analysis in industrial applications, however the highest precision is needed in physics, e.g. in astrophysics and fusion research or to test state-of-the-art atomic structure calculations. In the following it will be shown that in all these applications in physics, highly charged ions (HCI) are the key objects to study.

In the past, ground-based telescopes have accumulated a tremendous amount of data on cosmological objects in the visible range. Due to absorption in the atmosphere the x-ray spectrum emitted by these objects has become accessible only recently by means of space-telescopes, like Chandra and XMM-Newton. The x-ray images obtained with the instruments installed in those satellites exhibit remarkable differences to those showing only the visible spectrum, opening up new possibilities to a deeper understanding of these objects' formation and composition. Properties like temperature, density and matter composition of stars are determined by spectroscopic means via line intensities emitted by different ion species, the solar wind composition may be analysed from x-rays emitted when hitting atoms of cold comets etc., making the availability of precise laboratory data indispensable for a reliable deduction of such properties from the spectra.

Stellar conditions inside stars are certainly best reproduced on earth in nuclear fusion reactors like tokamaks, which have undisputably contributed most to the laboratory data available to astrophysics today. Moreover, great hopes are pinned to these devices, as they may provide the solution to the energy problem in the future, and not surprisingly a lot of effort is put into the development of the required technology. The physical processes in magnetically confined plasmas are highly complicated to understand and control, and it has been shown that spectroscopic measurements on both artificial and natural plasma impurities, like argon and tungsten, allow characterisation of the plasma and, thus, enable the operators to establish reproducible conditions. In fact, just as spectroscopic measurements on tokamak plasmas help understanding stellar plasmas, high-precision spectroscopy on highly charged ions prepared in a well-defined environment yields the fundamental basis for modelling and understanding magnetically confined fusion plasmas.

Modelling a plasma requires taking into account as many ionic states as possible at a given or assumed temperature. Unfortunately, accurate data are available only for a very limited amount of transitions in few ion species since highly charged ions are difficult to produce in the laboratory. Thus, a reliable theoretical description of atomic and ionic states is required to fill the unavoidable gaps where no experimental value can be found.

The modern theoretical framework for an accurate description of the atom was created with the development of quantum mechanics. A self-consistent mathematical representation of quantum mechanics including special relativity was formulated by Dirac in 1928. It was not until 1947 that this theory's limitations were revealed, when Lamb and Retherford discovered that the states $2p_{1/2}$ and $2s_{1/2}$ are not degenerate, as opposed to Dirac's prediction. A new field theoretical approach, quantum electrodynamics (QED), was developed, yielding the corrections necessary to bring theory into accordance with the experimental results. Indeed, it is the mathematical treatment of these corrections that constitute the difference between various models. For simple systems with a configuration isoelectronic to that of hydrogen ("hydrogen-like or H-like"), the necessary corrections are well known: even for the most extreme of all hydrogen-like benchmark systems, U^{91+}, the current theoretical predictions for the ground state Lamb shift are in good agreement with the experimental results, and their estimated uncertainty is tenfold smaller than the present error bar of the most precise experiments. However, already the accurate description of helium-like ions increases the theoretical challenge tremendously, for the electron-electron interaction needs to be taken into account. As the predictions of different theoretical approaches do not always agree on the level of their claimed accuracy, high-precision measurements on electronic transitions in helium- and lithium-like systems are required to test them. Only when a precise understanding of these few-electron ions is eventually achieved more complicated systems can be addressed on a similar level of accuracy.

When measuring reference data for astrophysics, plasma physics and theory, it is of vital importance to prepare the sample in a pure state to be able to reach the necessary accuracy. Of all existing devices giving access to radiation from highly charged ions, this requirement is nowadays best achieved by the Electron Beam Ion Trap (EBIT) and in large storage rings. Whereas with both technologies similar luminosities and, thus, x-ray yields are achieved and clean ionic excited states can be prepared, the EBIT, apart from being factors of 10 to 100 less expensive, offers further advantages making it a very competative, and sometimes even a superior tool for precision-spectroscopy, mainly for two reasons: First, often large solid angles and, therefore good statistical significance can be achieved and second, most important in the present context, since the ions are essentially trapped at rest in the laboratory frame, no Doppler shift corrections are needed at all. In contrast to many previous investigations, both technologies often enable to prepare very clean, singly excited states, leading to highly symmetrical lineshapes that have not to be corrected for on the basis of sometimes quite vague assumptions. Consequently, only the detector system, the available measuring time under stable conditions and the uncertainty of the reference chosen for absolute calibration limit the achievable accuracy.

For all these above mentioned reasons it is worthwhile to perform high-precision x-ray spectroscopic measurements on electronic transitions in highly charged ions with an EBIT. Many of them occurring in the hydrogen- and helium-like charge states of the elements from $_{11}$Na up to $_{36}$Kr emit radiation in the energy range easily accessible by crystal spectrometers. As an EBIT can produce all of these ion species, it is of great advantage to use a spectrometer that can cover a wide range of energies. Of all the different crystal spectrometer types that have been developed over the years, the flat crystal spectrometer is the one that poses the least restrictions on the coverable energy range. However, flat crystal spectrometers need collimated x-ray beams to be able to reach high accuracy. Because of the generally rather low x-ray flux emitted from an EBIT, this would be a strong argument against their use. Consequently, curved crystal spectrometers have been preferred for high-precision measurements with EBITs in the past. These devices offer considerably larger collection efficiency than flat crystal spectrometers, with the drawback of being able to cover only a small part of the available spectrum in one measurement and complications in both setup and data analysis.

Therefore, in the present work a novel method was developed that renders collimation for flat crystal spectrometers unnecessary, with emphasis on the particular aspects of data acquisition[1] and the analysis of relative wavelength measurements. Transitions in helium-like argon, an important artificial impurity in fusion plasmas, were investigated in detail and unprecedented relative accuracies have been achieved, sensitively testing state-of-the-art theoretical predictions.

The first chapter of this dissertation addresses explaining the theoretical description of electronic states in few-electron ions and gives an overview over the different calculation methods, the necessary corrections involved and the approximations made within them. In the second chapter, an introduction to x-ray spectrometry is given, and reference standards as well as advantages and disadvantages of different HCI sources are discussed. The third chapter gives a detailed description of the new method, its implementation in the spectrometer and the data acquisition process. The fourth chapter is devoted the data analysis procedure, the results obtained for He-like argon and their discussion. As an outcome, different calculations are compared to the new data, and their limitations are discussed. The disagreement with some of the predictions is significant, and is all the more pronounced the more the mutual interaction of the two electrons appears in the studied transition energies. A conclusion and an outlook are given at the end of this work.

---

[1] A more detailed description of mechanical aspects of the spectrometer than given in this work, as well as a geometrical simulation of the spectrometer and the preparation of absolute wavelength measurements is found in [Bra06].

Chapter 1

Theory of the atomic structure

One major achievement of atomic physics research until the present day is the enhancement of our knowledge and control of the macroscopic world by explaining the working principles of its microscopic building blocks, the atoms. Improved instrumentation, along with growing understanding of the fundamental laws that govern the atomic structure fuelled the interest to investigate it more and more closely. The insights gained and the means of investigation used in this process led to the development of the laser, nuclear spin tomography and electron microscopes, to name but a few. Today, the hydrogen atom with a recently achieved absolute accuracy in the determination of the $1s-2s$ transition frequency of $1.4 \cdot 10^{-14}$ [Fis04,NHR$^+$00,FKZ$^+$04] (Nobel prize 2005 for T.W. Hänsch) might be considered as basically understood, and the discrepancies found between theory and experiment seem to be attributed to the amount of computational effort put into the numerical calculations. To test the validity of the computational methods used to account for different effects arising from *e.g.* relativity or QED in strong fields, it is of paramount importance to not only study the hydrogen atom with the highest possible precision, but to explore systems with higher nuclear charges, where these effects are significantly boosted in their relative contribution to the level energies, without abandoning the simplicity of a one- or two-electron structure.

Strong-field and relativistic effects can be studied in great detail in highly charged ions, *i.e.* hydrogenic ions with only one single bound electron. The investigation of such ions as a function of different nuclear charges Z gives insight into strong-field QED as well as into the scaling laws of the various effects, thus helping to clarify the underlying physics. Hydrogen-like systems have been explored both experimentally and theoretically in recent years, and by now even for extreme cases like hydrogen-like uranium U^{91+} the theoretical calculations agree well with the measurements [YAB$^+$03]. However, for the complete range of Z, the situation has become interesting as the accuracy of the theoretical prediction is now often limited by parameters which depend on the strong interaction, like the proton radius, the nuclear charge and magnetisation distribution or on nuclear excitations. Vice versa, atomic experimental high-precision studies on hydrogen-like ions can be used to measure those parameters.

The addition of one more electron to form a so-called helium-like system introduces new difficulties for the theoretical description. The "many-body" problem per se is already challenging and defies an analytical description; but more than that, the electron-electron interaction is even more demanding to evaluate since relativistic and QED effects have to be taken into consideration. At present, a variety of theoretical approaches to calculate the energy levels of atoms with more than one electron exists, all of which involve advantages and deficiencies in comparison to the others.

This chapter is dedicated to provide an overview on the theoretical description of the atomic structure to be able to put the experimental results of this work into perspective. After a short introduction to theory's most important milestones, the different theoretical methods to describe few-electron atoms will be presented. Where possible, formulae that allow approximate calculations of the level energies, or corrections to refine those calculations, are given.

1.1 Modelling an atom

In 1859 Kirchhoff and Bunsen found that the emission spectra of atoms show distinct lines which are characteristic for the atom under study [Dem00]. Studying the spectrum of atomic hydrogen, Balmer realised in 1885 that the observed wavelengths could be calculated using

$$\frac{1}{\lambda} = R_y \left(\frac{1}{n_1^2} - \frac{1}{n_2^2} \right) , \tag{1.1}$$

with the Rydberg constant R_y and n_1, n_2 being positive integer numbers that were later found to be the main quantum numbers of the energy levels involved in the transition.

The first atomic model predicting this line spectrum was the planetary model developed by Bohr in 1913 [Boh13, Boh14]. Bohr postulated that an electron with mass m_e is moving on circular orbits in the Coulomb field of the nucleus with mass m_N without emitting radiation, except when changing orbits. Furthermore, he demanded that the total orbital angular momentum $|L| = \mu \cdot r \cdot v = n \cdot \hbar$ of the system with the reduced mass $\mu = m_e \cdot m_N/(m_e + m_N) \approx m_e$ must be quantised, *i.e.* be an integer multiple n of Planck's constant $\hbar$. These postulates allow only orbits with radii $r = a_0 \cdot n^2/Z$, where $a_0 = 5.2917 \cdot 10^{-11}$ m is the so-called Bohr radius.

Following de Broglie's idea of the wave-matter dualism, Schrödinger, Heisenberg, Dirac and others developed the much more stringent theory of quantum mechanics [Sch26], footing on the description of particles by their wave function $\psi(\mathbf{r}, t)$. The absolute square $\psi(\mathbf{r}, t) \cdot \psi^*(\mathbf{r}, t)$ is then interpreted as the probability to find the particle at the position $\mathbf{r}$ at the time t. Observables are represented as operators acting on the wave function. The expectation values of those operators can be related to the possible results obtained in their physical measurements.

The evaluation of the time-independent Schrödinger equation

$$\hat{H}\psi_{nlm}(\mathbf{r}) = \left(-\frac{\hbar^2}{2\mu}\Delta - \frac{Ze^2}{r}\right)\psi_{nlm}(\mathbf{r}) = E_{nlm}\psi_{nlm}(\mathbf{r}) \tag{1.2}$$

describing the electron with charge e and the operator for the momentum $p \equiv -i\hbar\vec{\nabla}$ in the potential of the nucleus with the charge Ze yields the energy E_{nlm} of the electronic level with the quantum numbers n, l, m which is described by the wave function $\psi_{nlm}(\mathbf{r})$. These are the main quantum number $n = 1, 2, 3, \ldots$, the orbital momentum quantum number $l = 0, 1, \ldots, n-1$ and the projection of the orbital angular momentum onto the quantisation axis, the magnetic quantum number $m = -l, \ldots, l$. In the following, atomic units, *i.e.* $\hbar = 1$, $e = 1$ will be used. The energy E_{nlm} in Eq. (1.2) is an eigenvalue to the system's wave function $\psi_{nlm}(\mathbf{r})$ when applying the Hamilton operator (or "Hamiltonian") $\hat{H}$. The first term of $\hat{H}$ corresponds to the kinetic energy $p^2/2\mu$ and the second term to the potential energy of the electron. An analytical solution to this equation can be found only for one-electron systems, by separating the wave function $\psi_{nlm}(\mathbf{r})$ into the product of a radial component $R_{nl}(r)$ and a spherical component $Y_{lm}(\theta, \phi)$. According to the Schrödinger equation, all energy levels with the same main quantum number n are degenerate, *i.e.* they have the same energy $E_n = E_{nlm}$. For one-electron systems the level energies are given by $E_n = -R_y \cdot Z^2/n^2$. This formulation explains the Balmer series *ab intio*, *i.e.* from fundamental principles.

The most important limitation in the Schrödinger theory is that it is not relativistically covariant, hence it does not take into account relativistic effects. A stringent way of including special relativity into the Schrödinger equation was developed by Dirac in 1928 [Dir28], treating the wave function $\psi(\mathbf{r}, t)$ as a 4-component tensor (rather than a scalar). This representation turned out to describe particles with an intrinsic spin, a new degree of freedom, which is of purely relativistic nature. The Dirac equation for a particle with spin $s = \frac{1}{2}$ in a potential $\hat{V}(\mathbf{r})$ is written as

$$\left(-i\hbar c\vec{\alpha}\vec{\nabla} + \beta m_0 c^2 + \hat{V}(\mathbf{r})\right)\psi(\mathbf{r},t) = i\hbar\frac{\partial\psi(\mathbf{r},t)}{\partial t} \ , \tag{1.3}$$

with the 4×4 Dirac matrices (or spinors)

$$\alpha_i = \begin{pmatrix} 0 & \sigma_i \\ \sigma_i & 0 \end{pmatrix} \quad \text{and} \quad \beta = \begin{pmatrix} I & 0 \\ 0 & -I \end{pmatrix} \tag{1.4}$$

that contain the 2×2 identity matrix I and the 2×2 Pauli matrices σ_i $(i = 1, 2, 3)$:

$$\sigma_1 = \begin{pmatrix} 0 & 1 \\ 1 & 0 \end{pmatrix} \ , \quad \sigma_2 = \begin{pmatrix} 0 & -i \\ i & 0 \end{pmatrix} \ , \quad \sigma_3 = \begin{pmatrix} 1 & 0 \\ 0 & -1 \end{pmatrix} \ . \tag{1.5}$$

For the hydrogen atom with the potential $V(\mathbf{r}) = -Z/r$, Eq. (1.3) can be solved analytically and yields the energy levels

$$E_{n,j} = m_0 c^2 \left\{ \left[1 + \left(\frac{Z\alpha}{n - (j+\frac{1}{2}) + \sqrt{(j+\frac{1}{2})^2 - (Z\alpha)^2}} \right)^2 \right]^{-\frac{1}{2}} - 1 \right\} \ , \tag{1.6}$$

where $j = |l-s|, \ldots, l+s$ is the total angular momentum, $\alpha = e^2/(4\pi\epsilon_0\hbar c) \approx 1/137$ is Sommerfeld's fine-structure constant and $m_0c^2 \approx 511\,\mathrm{keV}$ is the rest mass of the electron. The fine structure splitting between levels with different j values is reproduced by Dirac theory without any further corrections to a very high accuracy.

As a complete relativistic treatment of the atomic system under study may not always be applicable, and since the relativistic corrections to the energy levels are very small (provided that Z is not too large), it is sometimes convenient to use perturbation theory to account for relativistic effects. Up to order v^2/c^2 the relativistic Dirac Hamiltonian $\hat{H}_{REL}$ can be approximated as

$$\hat{H}_{REL} = \hat{H}_{NR} + \hat{H}_{MREL} + \hat{H}_{SO} + \hat{H}_{Darwin} \tag{1.7}$$

with the non-relativistic Hamiltonian $\hat{H}_{NR}$ and three correction terms. Here, $\hat{H}_{MREL}$ accounts for the relativistic mass gain of the electron on its movement around the nucleus, and the spin-orbit interaction $\hat{H}_{SO}$ describes the interaction between the orbital and spin magnetic moments. The so-called Darwin term $\hat{H}_{Darwin}$ can be understood as the consequence of the inability to localise the electron better than its Compton wavelength $\hbar/m_0c$ such that it interacts with the average of an extended electric field rather than the potential at its point-like position ("Zitterbewegung").

These operators acting on hydrogenic wave functions of the form $\psi_{nlm_lm_s}(q) = \psi_{nlm_l}(\mathbf{r})\chi_{1/2,m_s}$, where q denotes space and spin variables collectively, $\psi_{nlm_l}(\mathbf{r})$ is a one-electron Schrödinger wave function ($m_l = -l, \ldots, +l$ is the magnetic quantum number denoted previously by m) and $\chi_{1/2,m_s}$ are the spin eigenfunctions for spin one-half, yield corrections to the non-relativistic energy. The total relativistic level energy $E^{\text{approx}}_{n,j}$ approximated in first order of the perturbation expansion is then obtained [BJ03] as

$$E^{\text{approx}}_{n,j} = E_n \left[1 + \frac{(\alpha Z)^2}{n^2} \left(\frac{n}{j + \frac{1}{2}} - \frac{3}{4} \right) \right] \; . \tag{1.8}$$

It is seen from Eq. (1.8) that the binding energy $|E_{n,j}|$ is increased with respect to the non-relativistic value $|E_n|$, with larger relativistic contributions for higher Z and lower total angular momentum j. Up to order $(\alpha Z)^2$ Eq. (1.8) agrees with the exact relativistic formula (1.6) obtained by solving the Dirac equation for the nuclear potential.

As a side remark regarding the results of Dirac theory, it is noteworthy that apart from the expected positive energy eigenvalues also an equal amount of negative energy eigenvalues are obtained [Dir30]. Since there is no reason to omit the mathematically allowed negative eigenvalues, the consequence is that an electron in the lowest positive state - the ground state - should be able to make a transition to these negative energy states emitting the energy difference as a photon. Following the Pauli principle and the observation that the ground state is stable, Dirac reasoned that all negative states (the so-called Dirac sea) were already occupied by electrons. As a consequence he concluded that a vacancy (hole) in this Dirac sea would manifest itself as an electron with positive charge, thus predicting the existence of the positron. Only few years later, in 1932, the positron was experimentally observed by Anderson [And33], confirming Dirac's prediction.

1.2 The Lamb shift

The first experimental observation of a deviation from Dirac theory was made by Lamb and Retherford in 1947 [LR47]. As opposed to the prediction by Dirac theory where levels with the same main quantum number n and j but different quantum number $l = j \pm \frac{1}{2}$ are degenerate, Lamb and Retherford found a splitting between the $2s_{1/2}$ and $2p_{1/2}$ states. The total difference between the "real" level energy and the corresponding Dirac value is commonly referred to as the Lamb shift. Generally, finding these deviations is not surprising, as the Dirac theory assumes a point-like

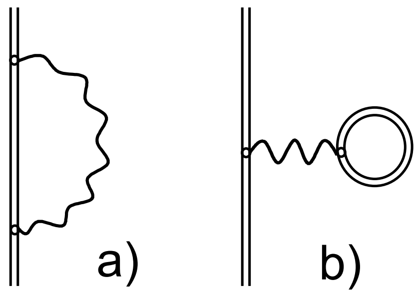

Figure 1.1: Feynman diagrams of the first-order QED corrections: a) the self energy (SE) and b) the vacuum polarisation (VP). The vertical axis indicates time, straight double lines represent electrons interacting with the nucleus (bound electron, electron propagator), wavy lines correspond to virtual photons. Both SE and VP are explained in the text.

nucleus of infinite mass. Still, only adding corrections addressing nuclear size and recoil effects cannot give rise to an effect of the Lamb shift's magnitude.

1.2.1 Quantum electrodynamics

The theoretical framework explaining the Lamb shift is quantum electrodynamics (QED). Beyond the principles of quantum mechanics, QED is a quantum field theory of electromagnetism, and describes the interaction of charged particles with the radiation field and with each other by the emission, absorption or exchange of virtual photons. The complex mathematical formalism of QED processes is commonly depicted by the illustrative Feynman diagrams (Fig. 1.1).

In a simplified picture, within the scope of Heisenberg's uncertainty principle [Hei26, Hei27] an electron in the Coulomb field of the nucleus can, over a time $\Delta t < \hbar/\Delta E = 1/\omega$, absorb and reemit a (virtual) photon of the energy $\hbar\omega$ without violation of energy conservation. The continuous emission and absorption processes lead to a 'smearing out' of the electron charge distribution over a finite volume as a result of the virtual photon's momentum, thus modifying the electron's potential energy. This effect is called the self energy (SE) interaction. The magnitude of this shift depends on the probability distribution of the electron in the Coulomb field of the nucleus and, thus, on the quantum numbers n and l. A rough estimation [EGS01] of the SE contribution to the $2s$-level Lamb shift in hydrogen taking into account only the change in the charge distribution,

$$\Delta E_{2s(SE)} \approx \frac{4m_0c^2(Z\alpha)^4}{n^3}\frac{\alpha}{3\pi}\ln\left[(Z\alpha)^{-2}\right] \approx 5.5\cdot 10^{-6}\,\mathrm{eV}, \tag{1.9}$$

already gives a result of the experimental value's magnitude found by Lamb and

Retherford (about $4 \cdot 10^{-6}$ eV). Due to the stronger nuclear field experienced by an electron in the $1s$ state, the ground state Lamb shift is larger and amounts to about $3.4 \cdot 10^{-5}$ eV in hydrogen.

Excitations from the above mentioned negative energy states that are solutions to the Dirac equation can be seen as virtual electron-positron pairs. Within QED the creation and annihilation of particles from the vacuum field is possible, and interactions of a bound electron with such virtual electron-positron pairs can take place. This effect is called vacuum polarisation (VP). A rough estimation of the influence of the VP on the $2s$ level of hydrogen,

$$\Delta E_{2s(VP)} \approx -\frac{4m_0c^2(Z\alpha)^4}{n^3}\frac{\alpha}{15\pi} \approx -1.24 \cdot 10^{-7}\,\mathrm{eV}, \tag{1.10}$$

shows that while it cannot be neglected for an accurate prediction of the Lamb shift, it is still of lower magnitude than the SE contribution (the contribution to the 1s level in atomic hydrogen is about $-8.9 \cdot 10^{-7}$ eV). Hence, the SE is the dominant contribution in the total Lamb shift in hydrogen.

The straight double-lines in Fig. 1.1 represent the interaction of the electron with the nuclear field. The standard theoretical approach in the case of light ions is to treat the nuclear Coulomb field as a perturbation, with the nuclear coupling constant (αZ) being the expansion parameter. This approach works well for light ions where $(\alpha Z) \ll 1$ but breaks down for heavy systems where the parameter (αZ) approaches unity. Instead, in heavy ions the Coulomb interaction of the electron with the nucleus has to be incorporated to all orders from the beginning, making the corresponding consideration far more difficult.

The one-photon Feynman diagrams in Fig. 1.1 have been calculated to high precision by a number of authors (see *e.g.* [YAB$^+$03] and references therein) and can be considered to be well established. Since both SE and VP are interactions of the electron with the surrounding electromagnetic field, it is not surprising that these effects scale strongly with the nuclear charge Z. In hydrogen-like argon (Ar^{17+}), the total ground state Lamb shift is already about 1.14 eV. In hydrogen-like uranium (U^{91+}), the $1s$ Lamb shift accumulates to 460.2 ± 4.6 eV [GSB$^+$05], with a calculated SE contribution of 355.05 eV [YAB$^+$03]. At the level of experimental accuracy in reach for these heavy ions, it is necessary to include second order diagrams (Fig. 1.2) in the calculation of their energy levels. In the case of the ground-state Lamb shift in U^{91+} the corrections of second-order in α amount to 0.6 ± 1.3 eV [YAB$^+$03]. The large error assigned to this value is due to the complexity in the calculation of the SESE diagrams (b) and (c) in Fig. 1.2 in heavy ions, which has been calculated only by Goidenko *et al.* [GLN$^+$01], a value that still has to be independently confirmed.

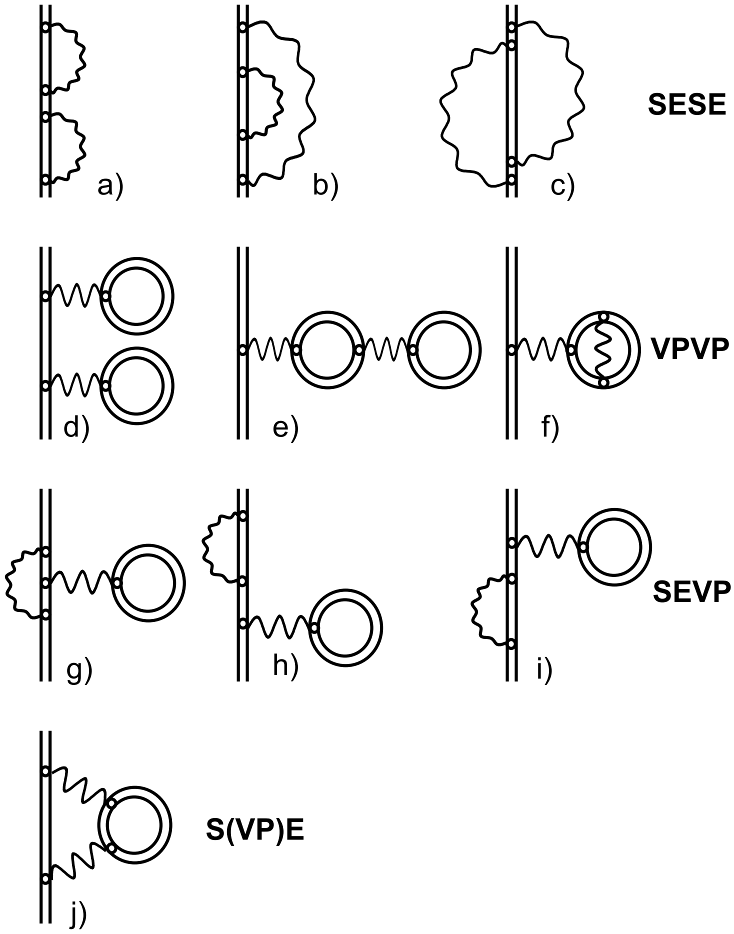

Figure 1.2: Feynman diagrams of the second-order QED corrections.

1.2.2 Nuclear size effects

Naturally, in heavy ions the contributions originating from the finite nuclear size are of greater magnitude than in hydrogen and, hence, cannot be neglected even though the experimental accuracy reached in the study of heavy ions is by far lower than in hydrogen. The electric and magnetic field generated by an extended charge and magnetisation distribution, respectively, is obviously different from a perfect central potential generated by a point-like nucleus, as it is assumed in the Dirac theory. A modified Dirac equation incorporating an extended nuclear charge distribution can be solved analytically with sufficient precision when the simplest model of the nuclear structure, the homogeneously charged sphere, is used [Sha93a]. On the basis of these calculations, for hydrogenic ions approximate expressions describing the energy shift (the so-called nuclear size effect) of the levels with $j = 1/2$ to an accuracy of 0.2% can be derived:

Table 1.1: The coefficients $b_0 - b_3$ as defined in Eq. (1.12) for the states $n = 1, 2, 3$ and the root mean square charge radius for selected elements (all values taken from [Sha93a]).

	b_0	b_1	b_2	b_3	Z	$\langle r^2 \rangle^{1/2}$ [fm]	$\Delta E_{1s_{1/2}}$ [eV]
$1s_{1/2}$	1.380	−0.162	1.612	0	1	0.809(20)	$4.247 \cdot 10^{-9}$
$2s_{1/2}$	1.508	0.215	1.332	0	10	3.024(20)	$6.176 \cdot 10^{-4}$
$2p_{1/2}$	1.615	4.319	−9.152	11.87	20	3.476(7)	$1.456 \cdot 10^{-2}$
$3s_{1/2}$	1.299	−1.010	3.897	−3.046	50	4.655(1)	1.9647
$3p_{1/2}$	1.730	0.493	0.091	2.358	90	5.707(50)	157.73

$$\Delta E(ns_{1/2}) = \frac{(\alpha Z)^2}{10n}\left[1 + (\alpha Z)^2 f_{ns_{1/2}}(\alpha Z)\right]\left(2\frac{\alpha Z}{n}\frac{R}{\hbar/m_e c}\right)^{2\gamma} m_0 c^2 \tag{1.11}$$

$$\Delta E(np_{1/2}) = \frac{(\alpha Z)^4}{40n}\frac{n^2-1}{n^3}\left[1 + (\alpha Z)^2 f_{np_{1/2}}(\alpha Z)\right]\left(2\frac{\alpha Z}{n}\frac{R}{\hbar/m_e c}\right)^{2\gamma} m_0 c^2 \ ,$$

$$\gamma = \sqrt{1-(\alpha Z)^2}$$

$$f_{nlj}(\alpha Z) = b_0 + b_1(\alpha Z) + b_2(\alpha Z)^2 + b_3(\alpha Z)^3 \ . \tag{1.12}$$

In these formulae, $R = \sqrt{5/3}\langle r^2 \rangle^{1/2}$ is the sphere's radius approximated to first order in terms of the root-mean-square radius ($\langle r^2 \rangle^{1/2}$), which is known from muonic atom x-ray measurements and electron scattering data [Ang04]. Table 1.1 lists the parameters $b_0 - b_3$ in Eq. (1.12) for the states $s_{1/2}$ and $p_{1/2}$ in $n = 1, 2, 3$ as well as nuclear radii for selected elements and the corresponding energy shift of the $1s_{1/2}$ level.

Two other, much smaller effects on the electronic energy levels arising from the nucleus have to be taken into account in a high-precision calculation: The recoil effect, which accounts for the finite mass and thus the movement of the nucleus, and the nuclear polarisability, which depends on the internal structure of the nucleus. In a non-relativistic theory the recoil effect is included simply via the reduced mass and is called the normal mass shift (NMS). This treatment is incomplete, as relativistic recoil contributions are already measurable in mid Z HCI. A full relativistic theory of the nuclear recoil in hydrogenic systems was formulated from an *ab initio* QED treatment [SAB$^+$98]. The nuclear polarisability has been evaluated *e.g.* in [NLPS96].

1.3 Complex systems

Within the error margins of even the most accurate experimental data, the theoretical predictions for the energy levels in hydrogen-like systems are confirmed when all above mentioned corrections are accounted for. Therefore, at the current level of experimental precision all important effects can be calculated to a sufficient level of accuracy. Hence, it is necessary to strive to further improve the experiments on hydrogenic systems in order to study the interplay of nuclear and atomic physics. Moreover, the investigation of more complex systems than hydrogen is essential, where theoretical predictions are less precise. HCI enable one to systematically study *e.g.* two-electron systems within a large range of nuclear charges.

Due to the introduction of a second electron into the Coulomb field of the nucleus one has to deal with a three-body system, for which generally no analytical solution can be found. Many theoretical approaches have been developed by introducing different approximations. Their applicability can only be tested experimentally. For an accurate description, the additional electrons have to be taken into account in both the Hamiltonian of the system as well as its wave function, which will be described in the following. Then, an introduction to the two major groups of approaches used, namely perturbation theory and variational methods, will be given, followed by an explanation of how the nuclear size, nuclear recoil and QED corrections are accounted for.

1.3.1 Many-body Hamiltonian

Similar to the hydrogen-like systems, the first step is to consider the non-relativistic Hamiltonian $\hat{H}$ for a system with the reduced mass μ consisting of n electrons in the Coulomb field of a nucleus:

$$\hat{H} = \sum_{i=1}^{n} -\frac{1}{2\mu}\Delta_i + \sum_{i=1}^{n} -\frac{Z}{r_i} + \sum_{i<j}^{n} \frac{1}{r_{ij}} \ . \tag{1.13}$$

In this equation the first term represents the single electron's kinetic energy, the second term is their respective potential energy and the last term corresponds to the potential originating from the mutual electrostatic repulsion of the electrons i and j, with r_{ij} being their distance. In an analogue way, the many-electron Dirac Hamiltonian is obtained by adding n one-particle Dirac Hamiltonians and the last two terms of Eq. (1.13). In either case, the Hamiltonian implies an instantaneous Coulomb interaction between the involved particles. This means that neither the retardation of the potential, *i.e.* the time it takes for the interaction to occur due to the finite value of the speed of light, nor the magnetic interaction that plays a role when describing moving charges are accounted for.

The lowest order relativistic correction to account for both the magnetic interaction and the retardation is obtained by introducing the so-called Breit interaction into the relativistic Dirac Hamiltonian through the Breit operator

$$\hat{V}_B = -\frac{1}{2r_{12}}\left(\vec{\alpha}_1 \cdot \vec{\alpha}_2 + \frac{(\vec{\alpha}_1 \cdot \vec{r}_{12})(\vec{\alpha}_2 \cdot \vec{r}_{12})}{r_{12}^2}\right) , \tag{1.14}$$

where $\vec{\alpha}_j$ is the vector of the Dirac matrices α_i as defined in Eq. (1.4) acting on the wave function of the electron j. The new, total Hamiltonian $\hat{H}_{tot}$ is also called the Dirac-Coulomb-Breit or the Breit-Pauli Hamiltonian. For more convenience, up to order $(v/c)^2$ this operator can be split into single components that describe the different electronic interactions:

$$\hat{H}_{tot} = \hat{H}_{NR} + \hat{H}_{MREL} + \hat{H}_{SO} + \hat{H}_{Darwin} + \hat{H}_{OO} + \hat{H}_{SS} + \hat{H}_{SOE} + \hat{H}_{SOO}. \tag{1.15}$$

Here, $\hat{H}_{NR}$ is the non-relativistic Hamiltonian and $\hat{H}_{MREL}$, $\hat{H}_{SO}$ and $\hat{H}_{Darwin}$ are the one-electron relativistic correction terms introduced in Chapter 1.1. The last three terms correspond to the many-electron relativistic corrections. $\hat{H}_{OO}$, the orbit-orbit interaction, reflects the interaction of the electronic charges through their dipole moments in the orbital movement, which to some extent also includes the retardation. $\hat{H}_{SS}$ describes the spin-spin interaction, $\hat{H}_{SOE}$ accounts for the interaction of spin and magnetic moments with an external magnetic field, and $\hat{H}_{SOO}$ (spin-other orbit) corresponds to the interaction of an electronic spin with the orbital movement of another electron.

1.3.2 Many-body wave functions

The simplest ansatz for a many-electron wave-function is to use the product of two one-electron wave functions $\Psi(\mathbf{x}_1, \mathbf{x}_2) = \varphi_1(\mathbf{x}_1)\varphi_2(\mathbf{x}_2)$, where $\mathbf{x}$ is the so-called spinorbital, containing the position and the spin of the electron. However, the resulting two-electron wave function is not antisymmetric, $\Psi(\mathbf{x}_1, \mathbf{x}_2) \neq -\Psi(\mathbf{x}_2, \mathbf{x}_1)$, meaning that it does not satisfy Pauli's exclusion principle. Therefore, the antisymmetric linear combination

$$\Psi(\mathbf{x}_1, \mathbf{x}_2) = \frac{1}{\sqrt{2}}\left(\varphi_1(\mathbf{x}_1)\varphi_2(\mathbf{x}_2) - \varphi_1(\mathbf{x}_2)\varphi_2(\mathbf{x}_1)\right) \tag{1.16}$$

with the normalisation factor $1/\sqrt{2}$ is used, which becomes zero when both wave functions are equal as required by the Pauli principle. Generalised to n electrons, the linear combination of the products of single-electron wave functions can be written as the Slater determinant

$$\Psi(\mathbf{x}_1, \mathbf{x}_2, \ldots, \mathbf{x}_n) = \frac{1}{\sqrt{n!}} \begin{vmatrix} \varphi_1(\mathbf{x}_1) & \varphi_2(\mathbf{x}_1) & \ldots & \varphi_n(\mathbf{x}_1) \\ \varphi_1(\mathbf{x}_2) & \varphi_2(\mathbf{x}_2) & \ldots & \varphi_n(\mathbf{x}_2) \\ \vdots & \vdots & \ddots & \vdots \\ \varphi_1(\mathbf{x}_n) & \varphi_2(\mathbf{x}_n) & \ldots & \varphi_n(\mathbf{x}_n) \end{vmatrix} . \tag{1.17}$$

The level energies of the system described by such a wave function are commonly computed using perturbative or variational approaches.

1.3.3 Solving the many-body problem: perturbation theory

Perturbative approaches to the many-body problem, like the relativistic many-body perturbation theory (RMBPT) and the 1/Z method, are very successful in the description of heavy few-electron atomic systems. This becomes clear in the example of the 1/Z method applied to heavy many-electron ions. The expansion parameter for the electron-nucleus interaction is the nuclear coupling constant αZ, whereas, due to the single charge of an electron, the electron-electron interaction is accounted for in terms of α only. If the number of electrons is much smaller than the nuclear charge Z, to zeroth approximation the electrons interact mostly with the Coulomb field of the nucleus, and their mutual interaction is represented by a rapidly converging perturbation expansion in $\alpha/(\alpha Z) = 1/Z$. However, with this (and likewise with the RMBPT) approach the description of light ions is difficult, since an accurate result requires evaluating very high orders of the expansion.

Other perturbative approaches, the so-called bound state QED (BSQED) methods, also work best for simple heavy systems. Generally, for relativistic calculations the aforementioned negative energy states are problematic, and in fact they can be included properly only with BSQED, by treating the negative energy states as positive energy positrons. However, BSQED is very impractical in the many-electron problem, and until the present day direct QED approaches have been applied only to heavy two-electron ions [Moh85] and three-electron ions [ASS$^+$03].

For light or complex ions, so-called all-order methods are best suited, where the name is derived from their capability to calculate parts of the electron-electron interaction (interactions through exchange of virtual photons) to all orders. Most of these methods are based on variational principles, which will be explained in the following.

1.3.4 Solving the many-body problem: variational methods

The optimal total wave function of the system can be determined by iteratively finding the set of wave functions forming the total wave function (Eq. 1.17) that minimises the system's energy, *i.e.* the expectation value of the Hamiltonian used in the calculation. The process is stopped when the result of an iteration no longer significantly deviates from the previous iteration, meaning that the result has converged.

One of the first variational approaches that was developed is the Hartree-Fock method, where the so-called Fock-operator is constructed for each iteration. The Fock operator is based on the one-electron non-relativistic Hamiltonian which contains the electron's kinetic energy and the nuclear Coulomb potential. Additionally, the mutual repulsion of the electrons is accounted for in a sum, where each term is the averaged potential acting on an electron generated by all other electrons. Thus, all but one active electron are considered static. Although it is only a rather simple approach, the Hartree-Fock method reaches reasonable accuracy of 1 % or better in the determination of the energy levels. Still, the electron-electron interaction is considered only through its central field monopole contribution and the antisymmetrisation (exchange energy or exchange potential), and relativistic effects are completely neglected. In a modification of the original method, the relativistic Hartree-Fock method also includes magnetic interactions, increasing the overall precision. Further effects can then be included as perturbations. A similar approach that includes relativistic effects from the beginning is the Dirac-Fock method, which uses a one-electron Dirac Hamiltonian as the basis for the modification to become the Fock operator.

For a more accurate prediction it is necessary to also include the electronic interaction with unoccupied states (mixing of states) or, in other words, to account for angular correlations in addition to the modification of the central potential by the presence of further electrons. In order to include this one can add extra configurations to the system by using linear combinations of Slater determinants or configuration state functions (CSF) Ψ_i to build the correlated n-electron atomic state function (ASF) Φ:

$$\Phi = \sum_{i=1}^{N} c_i \Psi_i \tag{1.18}$$

with the iteratively optimised mixing coefficients c_i. The configurations underlie the restriction that the total angular momentum quantum number J, the magnetic quantum number M and the parity P are shared. As an example, the He-like ground state ASF can be described by the configuration expansion

$$|\Phi(\mathrm{He}_{gs})\rangle = c_1|1s^2_{1/2}\rangle + c_2|2s^2_{1/2}\rangle + c_3|2p^2_{1/2}\rangle + c_4|(2p^2_{3/2})_0\rangle + \dots \ , \tag{1.19}$$

where the last subscript indicates $J = 0$. If only the first term $|1s^2_{1/2}\rangle$ is used, the method is equivalent to the above mentioned ("single-configuration") Dirac-Fock method. The mixing coefficients can then be determined for a given set of CSFs by diagonalising the Hamiltonian:

$$\sum_{j=1}^{N} \left(\langle \Psi_i | \hat{H} | \Psi_j \rangle - E_{ASF} \delta_{ij} \right) c_j = 0 \ , \tag{1.20}$$

with the Kronecker delta δ_{ij}. If the mixing coefficients are optimised this way the method is called configuration interaction method (CI or RCI for the relativistic counterpart). The more configurations one includes in the correlated wave function the higher the accuracy of the calculation becomes, at the price of computational time.

The more advanced multi-configuration Hartree-Fock (non-relativistic) or multi-configuration Dirac-Fock (MCHF or MCDF, respectively) methods start off from such a CI calculation that generates estimate intial wave functions, potential and mixing coefficients. Then, the electron-electron interaction is evaluated and accounted for by creating new wave functions and restarting the process. This cycle is repeated until convergence of eigenvalues and wave functions is reached. As the wave functions are optimised in the process, less configurations than in a pure CI method are needed to reach an accurate result, and the MCDF method is more efficient in describing electron correlation effects.

Both the RCI and the MCDF depend only on the single electron coordinates $|\mathbf{r}_i|$ but not directly on the relative coordinates $r_{ij} = |\mathbf{r}_i - \mathbf{r}_j|$. If the ASF also explicitly involves the complete position information of the single electrons, *i.e.*

$$\begin{array}{ll} s = r_1 + r_2 & 0 \leq s \leq \infty \\ t = r_1 - r_2 & -\infty \leq t \leq \infty \\ u = r_{12} & 0 \leq u \leq \infty \quad , \end{array} \tag{1.21}$$

so-called Hylleraas type ASFs

$$\Phi(s,t,u) = e^{-ks} \sum_{l,m,n=0}^{N} c_{l,2m,o} s^l t^{2m} u^n \tag{1.22}$$

that offer a huge amount of parameter combinations for the optimisation process can be constructed, and of all techniques the electron-electron correlation is reproduced best this way. On the other hand, the Hylleraas technique cannot be directly applied to the relativistic problem, yet it gives very accurate results for light systems where correlation is strong and relativistic and QED effects play a minor role, such that they can be included as perturbations.

1.3.5 Solving the many-body problem: nuclear size and recoil corrections

The description of the few-electron atom is not complete once the many-body problem has been evaluated. While *e.g.* finite nuclear size effects can be included in the Hamiltonian by replacing the nuclear Coulomb field with the field of a distributed nuclear charge, corrections due to the nuclear recoil (finite nuclear mass) and QED-effects have to be evaluated independently and added later. A common way to account for the nuclear recoil is to perform the calculation with an infinitely heavy nucleus, and then to simply use the finite-mass Rydberg constant when converting from atomic units to eV (normal mass shift, NMS). Additionally, the recoil effects of the mutually interacting correlated electrons, known as the specific mass shift (SMS) has to be included in a high-precision calculation of ions of certain isoelectronic sequences, since its contribution can be of the same order as the NMS [Sor05]. In the case of two-electron ions of medium nuclear charge Z as they are studied in this work the SMS contributes only very little to the total level energies and cannot be resolved experimentally. The SMS in helium-like ions from a relativistic calculation are tabulated in [BBP01].

1.3.6 Solving the many-body problem: QED approaches

The two-electron QED corrections pose additional problems and are an active field of research [Sha02]. They can be divided into “non-radiative” and “radiative” QED effects. The former are part of the ladder and crossed-photons diagrams shown in Fig. 1.3, and can to some extent already be accounted for in the electron-electron interaction terms included in all-order methods. The latter are those classes of diagrams that include a vacuum polarisation or self energy contribution, as depicted in Fig. 1.4. These are also called the “two electron Lamb-shift”.

In first approximation, the many-body Lamb shift can be regarded as a screening of the single-electron Lamb shift, and is often considered as a modification of

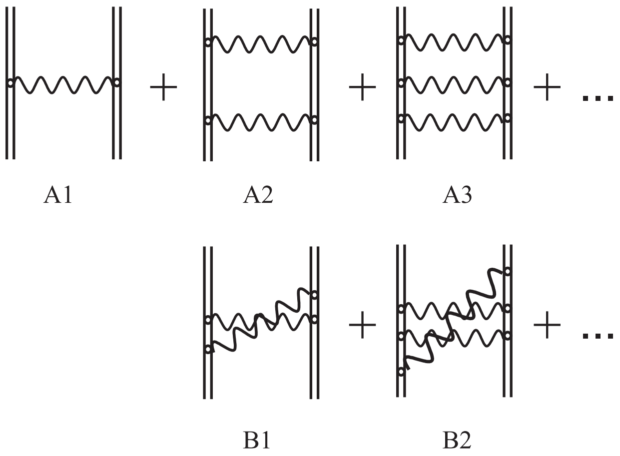

Figure 1.3: Ladder (A2, A3) and crossed-photons (B1, B2) diagrams of the electron-electron interaction.

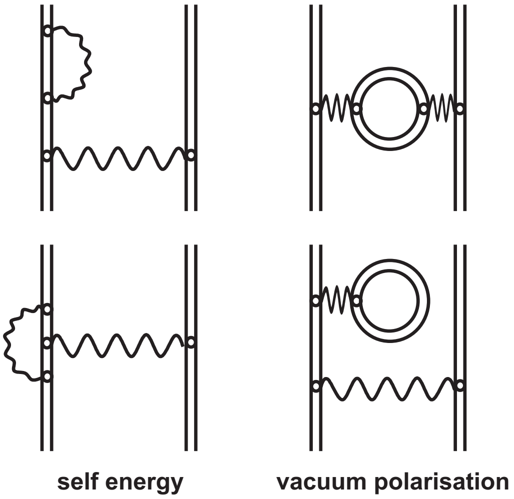

Figure 1.4: Feynman diagrams of 2-electron radiative QED effects.

the nuclear potential. Due to their elaborate treatment, the QED parts of a calculation by Drake [Dra88] have been used by many other groups (*e.g.* [PJS94]). Drake obtained QED contributions to the energy levels by using the leading terms of an expansion in αZ. These QED corrections are best applicable for low-Z, as for higher Z the expansion parameter αZ is larger and higher orders need to be considered in the calculation. The leading non-radiative, two-electron vacuum polarisation and two-electron self energy QED terms for the ground state energy of He-like ions are [PSS^{+}97, LPS95]:

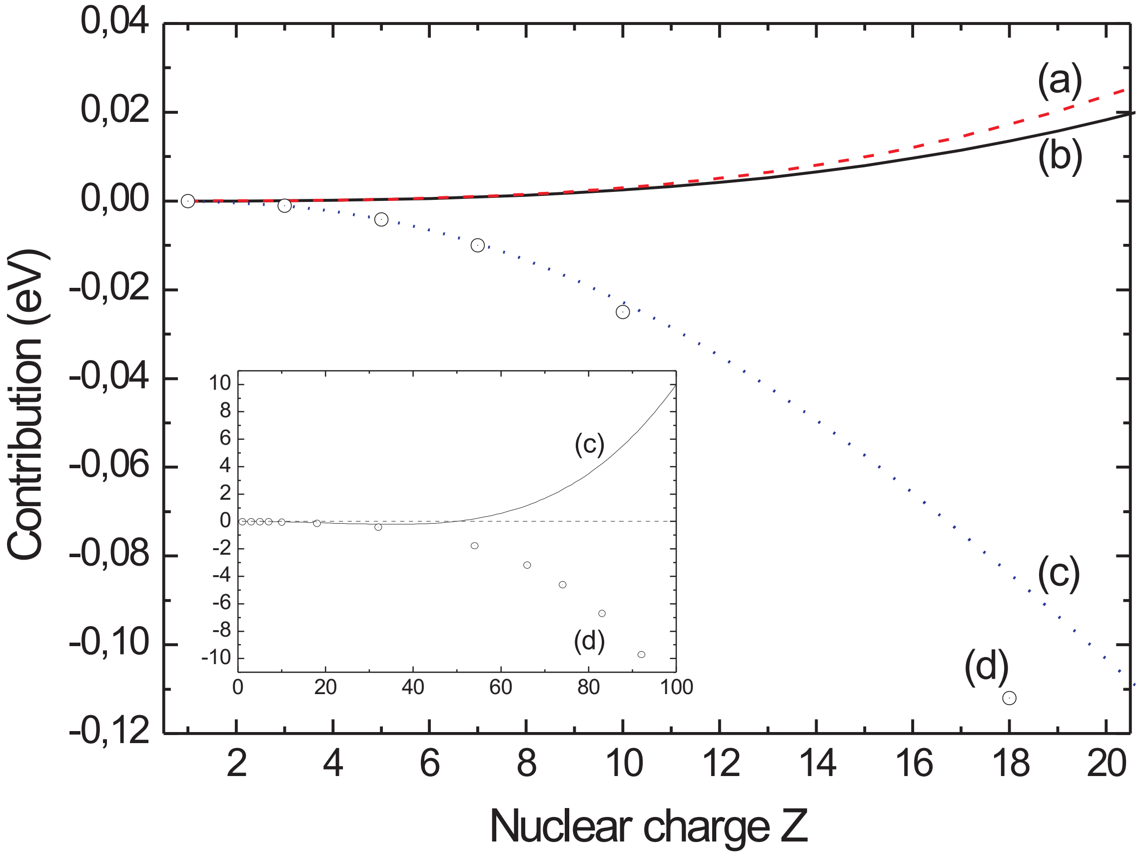

Figure 1.5: Two-electron QED contributions calculated from Eqs. (1.23 to 1.25): (a) non-radiative, (b) vacuum polarisation, and (c) self energy. The points (d) are all-order numerical results for the 2-electron SE-contribution from [PSS$^+$97]. The insert also shows the self energy calculations (c) and (d), but for elements up to uranium.

$$\Delta E_{NR} = \alpha^2 \frac{(\alpha Z)^3}{8\pi}\left[-\frac{2}{3}\ln(\alpha Z) + \frac{14}{3} + 2\ln 2 - 1.9091\right] m_0 c^2 \tag{1.23}$$

$$\Delta E_{VP} = \alpha^2 \frac{(\alpha Z)^3}{\pi}\left[\frac{3}{5} + \frac{2}{5}\ln 2\right] m_0 c^2 \tag{1.24}$$

$$\Delta E_{SE} = \alpha^2 \frac{(\alpha Z)^3}{\pi}\left[\left(\frac{7}{2} - 2\ln 2\right)\ln\left[2(\alpha Z)^2\right] + 2.8388\right] m_0 c^2 \tag{1.25}$$

The functions 1.23 to 1.25 are graphically depicted in Fig. 1.5, along with numerical all-order calculations from [PSS$^+$97] for the two-electron self energy contributions. While the two-electron vacuum polarisation is well described by Eq. (1.24) [PSS$^+$97], for the self energy the agreement between Eq. (1.25) and the numerically obtained results is good only at low nuclear charge Z. For higher Z the (αZ)-expansion method is not meaningful anymore, as the higher order contributions that were not included become more important. An overview over different calculations performed over the years is found in [ASY$^+$05].

Meanwhile, with the more and more refined techniques developed for bound-state QED, it has now become possible to calculate *ab initio* two- and three-electron ions [MPS98, ALPS04, ASY$^+$05]. The biggest problems restricting a full QED description of the ground state arise from "quasi-degenerate levels", *i.e.* closely spaced excited states (the levels $(1s2p)\,^1P_1$ and $(1s2p)\,^3P_1$ are standard examples for quasi-degenerate levels). Techniques to solve these problems have recently been developed, like the covariant evolution-operator procedure [LASM01], the line profile approach [ALPS04] and the two-times Green's function method (TTGF) [Sha90, Sha93b, Sha02].

The most complete many-body *ab initio* QED calculation to date has been performed by Artemyev *et al.* [ASY$^+$05] for the $n = 1$ and $n = 2$ energy levels in He-like ions, employing the TTGF procedure. All contributions up to three-photon exchange QED effects, $\alpha^3(\alpha Z)^2$ and higher, and higher-order one-electron two-loop QED corrections, $\alpha^2(\alpha Z)^7$ and higher, have been given in that work.

1.3.7 Experimental tests

Strong field QED contributions can best be measured in heavy, highly charged ions. Concerning electronic correlation, in helium-like ions with $Z \geq 32$ the two-electron contributions to the ground state have been measured directly by comparing the ionisation energy of a He-like system with that of a H-like system with the same nucleus, by studying radiative recombination processes into bare and hydrogen-like ions [MES95, GSB$^+$04]. For the two-electron contributions, it is also interesting to go to lower nuclear charges, where the mutual interaction of the electrons appears more clearly due to the weaker field generated by the nucleus. Here, laser-spectroscopic measurements of helium have revealed a discrepancy between theory and experiment for the helium fine-structure splitting if higher-order QED corrections are taken into account (see [Dra02, PS03, CGD$^+$04, MWD$^+$04]). It seems judicious to complement the measurements in helium and heavy two-electron ions with high-precision measurements of transition energies in helium-like ions with moderate nuclear charge Z.

For ions of medium and low Z, photon spectroscopy yields very accurate differences between the involved states' energies and, hence, also provides access to excited states that are impossible to explore in ionisation potential measurements of the type mentioned above. Thus, it allows one to probe different aspects of relativity and interelectronic correlation by comparing the energies of transitions from excited levels that are affected in a different way and strength by these effects. For example, for an excited electron the expectation value of its distance $< r >$ from the nucleus is smaller for s states than for p states. Hence, the nuclear field acts stronger on a $2s$ electron than a $2p$ electron and, thus, for the former QED and relativistic effects play a larger role while the interaction with the electron in the $1s$ orbital is less apparent. Furthermore, in the case of parallel orientation of the electrons' spins the spatial wave function has to be antisymmetric, leading to a smaller spatial overlap of the electrons than in the case of antiparallel spins (symmetric spatial wave function) and, thus, less mutual interaction between the electrons in the state $1s2s\ ^3S_1$ than in the state $1s2s\ ^1S_0$. Consequently, by comparing the energies of transitions from the $1s2s\ ^3S_1$ and the $1s2p\ ^1P_1$ states to the ground state in helium-like ions, the contributions of relativistic, QED and correlation effects can be effectively disentangled, yielding seperate information about all effects and their contribution to both the ground state and excited level energies. The experimental challenges and reasons to perform spectroscopic measurements of helium-like ions with respect to transitions in hydrogen-like ions will be subject of the following chapter.

Chapter 2

X-ray spectroscopy on highly charged ions

Aiming at performing high-precision wavelength measurements on transitions in highly charged ions emitting radiation in the soft x-ray region, there are three main issues that need to be considered: The device giving access to the ions, the spectroscopic technique and the reference standard used. This chapter discusses the different possibilities one has for each of the three items and the limitations they pose on the achievable accuracy.

2.1 The source

In [FKKM01], a table listing the most accurate x-ray measurements on Lyman-α transition energies in one-electron ions with a nuclear charge $Z > 12$ is given. According to this table, five measurements have reached an accuracy of better than 50 ppm with a record of 5 ppm [BDFL85] until the present day. Interestingly, no less than four different techniques were used to prepare the ions for these measurements, such that no ad hoc answer can be given to the question which ion source one should use. The four different techniques are the following:

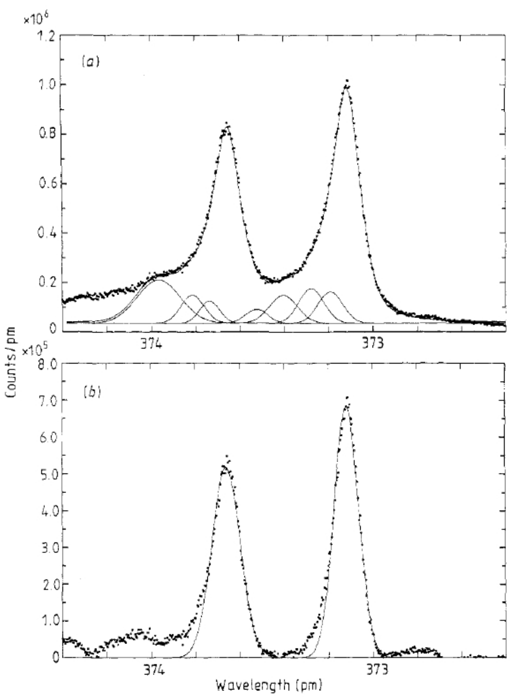

Figure 2.1: An Ar^{17+} Lyman-α spectrum obtained using the recoil ion technique. "(a): Experimental Lyman-α profile (dots) and empirical fit (full curve) using seven satellite components (b): Experimental Lyman-α profile with theoretical satellite background subtracted (dots) and single-component fit to the lines (full curve)." In (a), only the fitted satellite components are depicted. Figure and citation are taken from [BDFL85]

The *recoil ion technique* is described in detail in [BDFL85]. The basic principle of this method is shooting heavy ions with a velocity of a few percent of the speed of light, generated in an accelerator, through a gas cell. In the encounter with the heavy ion, the gas atoms will be ionised and excited, and the photons emitted upon deexcitation can be studied. The advantage of this technique in comparison to earlier techniques used at accelerator facilities is that the ions of interest are basically at rest, thus the Doppler-shift does not limit the achievable accuracy. The main disadvantage of this technique is a direct consequence of the ion production mechanism. Many transitions occur in multiply excited ions in which a second, passive electron is present on an outer shell: $2p\ nl \rightarrow 1s\ nl$. This so-called spectator electron leads to a partial screening of the nuclear potential, lowering the energy difference between the inner shells and, consequently, reducing the energy of the emitted photon. The spectral quality of the observed lines is, thus, tremendously impaired, as can be seen from figure 2.1.

The accuracy reached with this technique is obviously limited by the modelling of those satellite contributions to the spectrum. Still, the most accurate wavelength measurements of the resonance transitions in both H- and He-like ions have been measured with this method [BDFL85, DBF84].

Tokamak plasmas [MRK+86] quickly ionise intentionally introduced impurities to the highest charge states, and recombination as well as electron impact leads to a strong excitation of the ions produced. In these thermal plasmas, emission lines of interest are very intense, and excellent statistical significance can be achieved within a typical measuring time. However, similarly to the recoil ion technique, the observed emission lines are not free of satellites, although the contamination is of much lower extent (see Fig. 2.2). Additionally, due to a possible bulk movement of the ions in the line of sight of the spectrometer, Doppler shift must be accounted for in the error estimation.

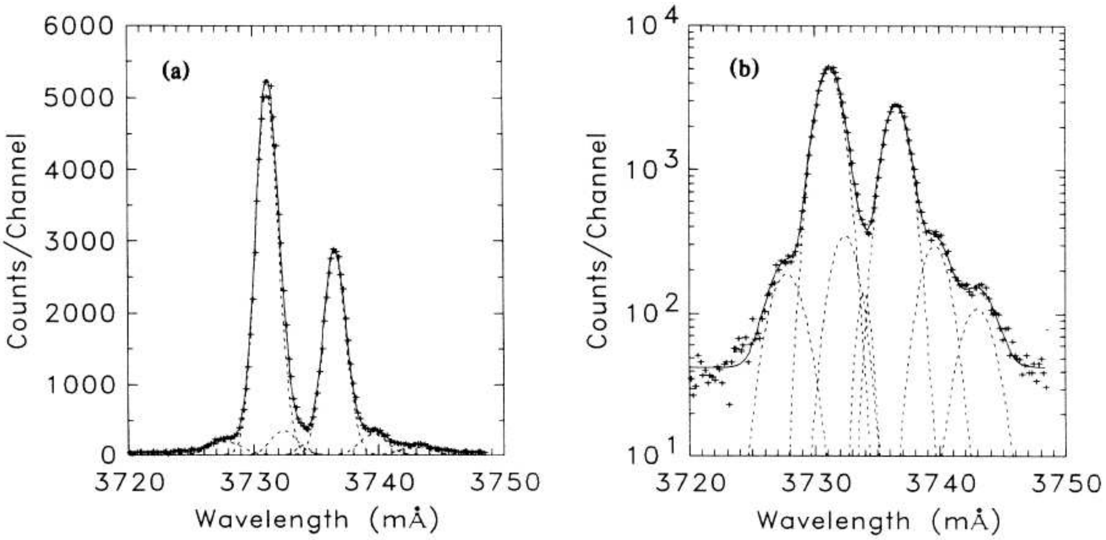

Figure 2.2: An Ar^{17+} Lyman-α spectrum obtained at the Alcator C tokamak“(a): A portion of the spectrum in the vicinity of the Ar^{17+} Lyα doublet together with the Gaussian line fits. (b): Same as (a) but on a semilogarithmic scale.” Figure and citation are taken from [MRK+86]

To solve the satellite contamination and Doppler-shift problems, another accelerator-based method was developed, using ion *deceleration and electron capture in a gas jet target* as described in e.g. [BIF+91]. Here, the ions of interest are first stripped of all electrons in a beam foil before they capture an electron from a neutral atom in a gas jet. The peak positions are measured at several different beam velocities, allowing to monitor the Doppler shift quite precisely. In contrast to the recoil ion technique, the spectra obtained are of high purity (see Fig. 2.3), such that using this method does not pose other limitations to the total achievable accuracy than those arising from the Doppler-shift corrections and from modelling the apparatus profile asymmetry.

The device closest to a tabletop experiment in this compilation is the *Electron Beam Ion Trap* (EBIT). In an EBIT, the ions are radially and axially confined by the space charge of a monoenergetic electron beam and a set of cylindric electrodes (drift tubes), respectively. As the trap volume is small and clearly defined, preventing bulk movements of the ion cloud, no Doppler shift needs to be taken into account. Due to the sequential ionisation process and the sharp electron energy distribution function the trapped ions have a narrow charge state distribution. The lifetimes of excited states in an EBIT are typically orders of magnitude smaller than the time between two successive electron-impact excitation processes. The probability for transitions to occur in multiply excited ions is therefore very low, and the obtained spectra are found to be free of satellite contaminations within the statistical accuracy, as

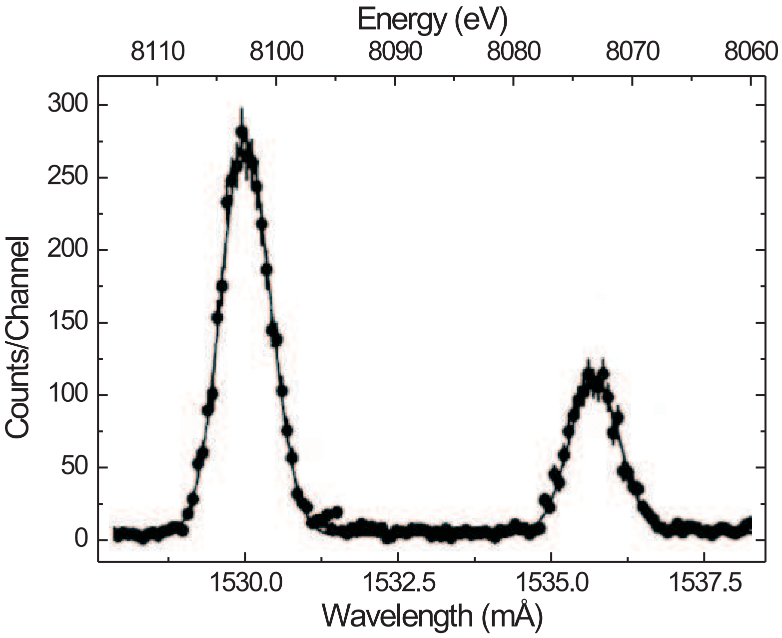

Figure 2.3: A Ni^{27+} spectrum obtained using the deceleration and electron capture in a gas jet target technique (from [BIF+91], axes modified).

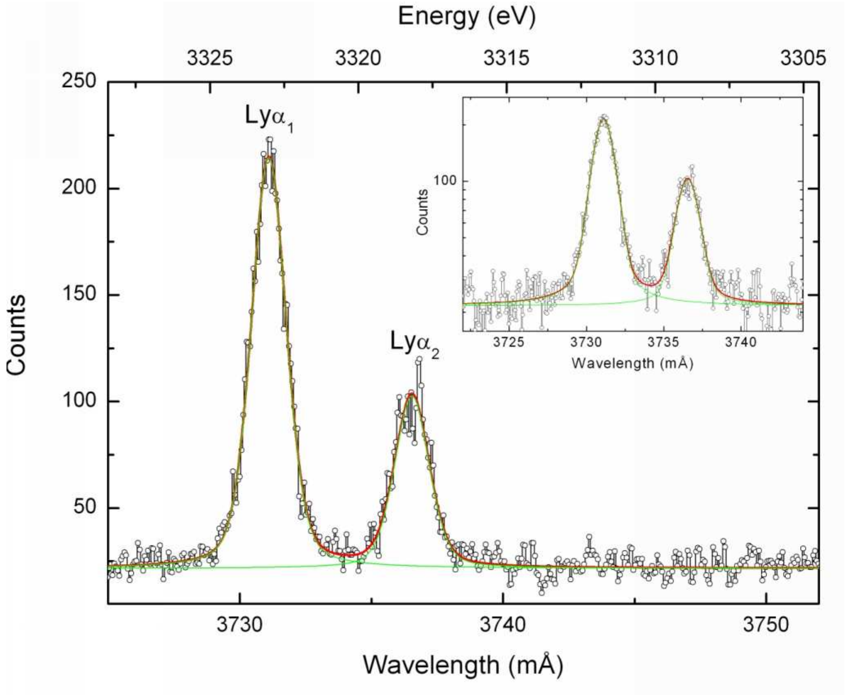

Figure 2.4: Datapoints (dots) and Voigt fit (solid line) of an Ar^{17+} spectrum obtained at the HD-EBIT (this work). The insert shows the same spectrum on a logarithmic scale.

illustrated in Fig. 2.4. The low excitation rate is, at the same time, the greatest disadvantage of an EBIT, as it leads to a comparatively low x-ray flux.

As any corrections to the acquired spectra immediately limit the achievable accuracy, the recoil ion technique and tokamak plasmas are unfavourable choices for high-precision spectroscopy[1]. Comparing the EBIT with the deceleration and electron capture method, important advantages are the comparatively small size of an EBIT and the negligibly small Doppler shift, whereas the spectral quality is similarly good in both methods. The small size and the purity of the obtained spectra have led to EBITs becoming the tool of choice for transition wavelength measurements in few-electron ions. Since this work was conducted at the Heidelberg-EBIT, before addressing possible detector systems a more detailed description of the EBIT working principle is given in the following.

2.1.1 The Heidelberg-EBIT

An EBIT is a device for the creation and trapping of highly charged ions. In addition to the spectroscopic study of transition energies in these ions, an EBIT provides the possibility to measure further important and interesting quantities, like the lifetimes of metastable excited states with high precision [LJ$^+$], to gain insight in dynamic effects like quantum interferences [GCB$^+$05] and, last not least, also to deliver extracted ions to other experiments [FFD$^+$02].

The working principle of an EBIT is sketched in Fig. 2.5. An electron beam is emitted by a Pierce-geometry cathode, accelerated towards a set of three or more cylindric electrodes (drift tubes), then decelerated and dumped into a collector electrode. A strong magnetic field generated by two superconducting magnet coils in a Helmholtz-configuration compresses the electron beam to typically few ten micrometers diameter. The negative space charge of the electron beam acts attractive on the positive charge of ions created by impact ionisation of neutral gas injected into the electron beam, causing the ions to be trapped radially. To also obtain trapping in the axial direction, a repelling positive voltage is applied to the outer drift tubes with respect to the central one.

In experiments requiring hydrogen-like and helium-like ions of medium nuclear charge Z at the Heidelberg-EBIT for either spectroscopy or extraction, respectively, the electron beam current is commonly set to $I_e \approx 300-400\,\mathrm{mA}$ at an electron beam energy of $E_e \approx 10-15\,\mathrm{keV}$ to obtain good ionisation and excitation rates. With these parameters and the magnetic field of 8 Tesla, the radial trapping potential (in

---

[1] There is of course also scientific interest in the processes involved in the creation of satellites, in which a satellite-rich spectrum may be welcome.

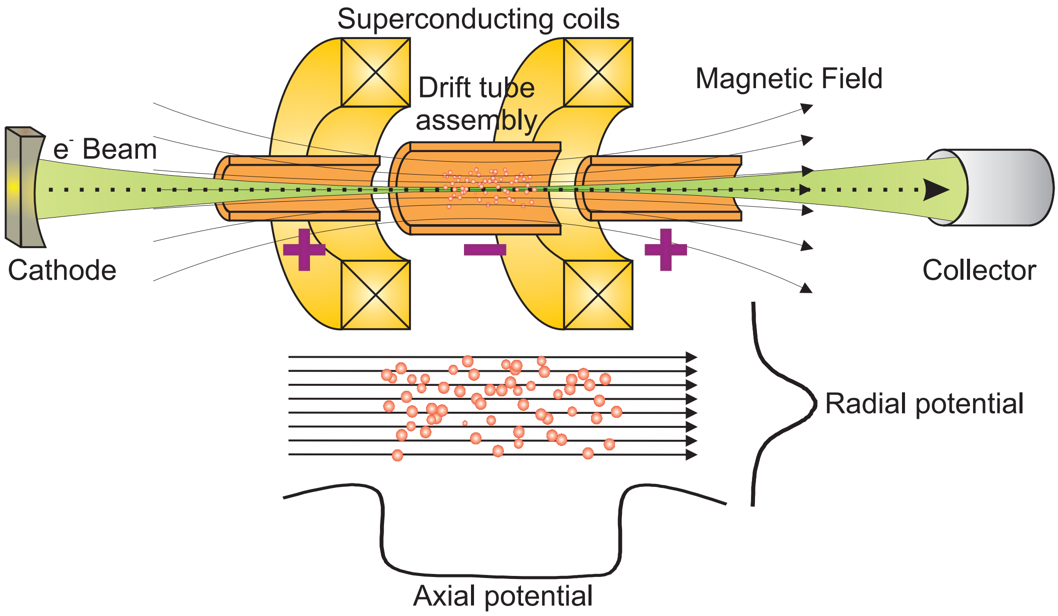

Figure 2.5: Principle of an electron beam ion trap.

the center of the electron beam) is of the order of $(250 \cdot q)\,\mathrm{eV}$, where q is the charge state of the trapped ion. The axial potential $U \cdot q$ is defined by the positive voltage U applied to the drift tubes, which is typically about 100 V. With these settings, the axial trapping potential is lower than the radial trapping potential, and ions that overcome the axial barrier, *i.e.* that evaporate from the trap, follow the electron beam to the cylindrical collector electrode and can be extracted from the EBIT.

The trap is deeper for ions with higher charge state q, and, hence, ions of interest can be cooled evaporatively by adding gas with low nuclear charge Z (*e.g.* neon or nitrogen). In any case also barium ($Z = 56$) and tungsten ($Z = 74$) ions originating from the hot cathode material slowly accumulate in the trap with time. To prevent these ions from supplanting the ions of interest, in experiments investigating ions with lower Z it is necessary to completely clear the trap in regular intervals (10−20 s). This so-called “dumping ” is achieved by lowering the axial trapping potential and can also be used for a pulsed extraction of the ions.

The ion cloud diameter is much larger than that of the electron beam. However, since ions can only be excited within the electron beam, the diameter of the luminous part of the ion cloud depends on the lifetime of the excited states and the velocity of the ions. In the experiments performed in this work, the lifetimes of the excited states of interest are of the order of 10^{-13} s [JS85], and so only ions located within the electron beam emit the detected radiation. A more detailed description of the Heidelberg-EBIT is found in [Gon05].

2.2 The detector

The future of high precision wavelength measurements in the x-ray region certainly belongs to microcalorimeters. These devices basically consist of a small amount of material that is connected to a thermal bath held at a temperature of several 10 mK. At these temperatures the heat capacity is very low, and the small amount of heat introduced to the system by absorption of a photon leads to a measurable temperature change. Its value can be determined very precisely, and a resolution of 3.4 eV at 5.9 keV has been achieved [FLD⁺04] with these devices, which is competitive with that obtained with modern crystal spectrometers. At the same time, the absorption efficiency is high (99.9 % at 6 keV). However, the time constant of reaching thermal equilibrium with the heat bath is of the order of 300 μs, limiting the currently achieved maximum counting rates. With these parameters it is clear that even coincidence measurements are feasible with these devices, without the need for a compromise in energy resolution. Unfortunately, the absorber material needs to have a very small mass to be able to effectively measure temperature changes, thus limiting the detector size. Array detectors are being developed to overcome these inconveniences.

Until microcalometry becomes widely applicable, crystal spectrometers will maintain their current lead in high-precision wavelength measurements in the x-ray region. Although 90 years old, there is still progress being made in the development of these devices, the most prominent of which has been the determination of the crystal lattice constant of silicon using optical wavelength standards. The Si lattice constant is now coupled to the meter with a relative standard uncertainty of only $\frac{\delta d}{d} = 2.9 \cdot 10^{-8}$ (see [MT00] and references therein), opening the opportunity to measure x-ray wavelengths with unprecedented precision.

All different crystal spectrometer types share the method of transforming wavelength/energy information into a geometrical quantity by applying Bragg's law:

$$n\lambda = 2d\sin\theta\,, \text{ and } E = \frac{hc}{\lambda}$$

After the reflection of radiation with the wavelength λ on a crystal with the lattice spacing d under the Bragg-angle θ, one can either derive the spectral line's wavelength by measuring the Bragg angle (usually with respect to a reference line) or by using a position sensitive detector (PSD) or a photographic recording and comparing the spatial position of the unknown line with the position of one or more reference lines in the spectrum.

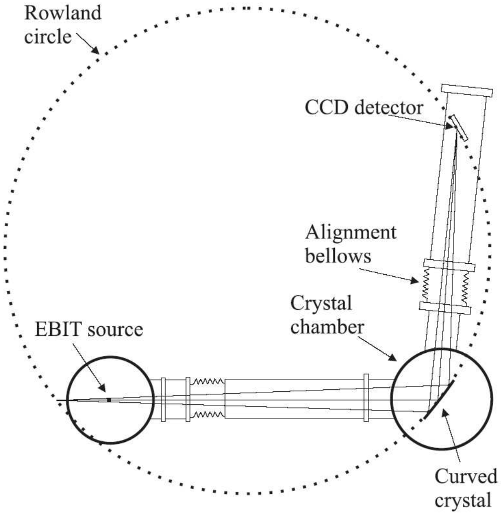

Figure 2.6: Schematics of a Johann-geometry spectrometer at an EBIT (from [TCM$^+$00]).

The flat crystal spectrometer should in principle allow to directly exploit the high accuracy to which the crystal lattice spacing is known. However, the reflection position of the x-rays on the crystal must be well defined, since otherwise the Bragg angle cannot be directly derived from the measured crystal angle. Depending on the collimation, it may be necessary to scan the crystal angle to find the intensity maximum of the reflected x-ray line, limiting its use to high-flux applications. But also without collimation, as the Bragg relation is fulfilled only on a narrow region on the crystal surface, the overall efficiency of a flat crystal setup is low.

To overcome those disadvantages, experiments with low x-ray flux have mostly been performed using curved crystal spectrometers. Prominent properties of these spectrometer types are their high reflection efficiency (due to focusing of the incident x-rays) and their usually high spectral resolution. The most common curved crystal spectrometers are of the Johann-geometry as shown in Fig. 2.6. In this geometry, the crystal is cylindrically bent to a curvature radius of R. If both the x-ray source and the crystal are placed on the so-called Rowland circle with the radius $R/2$, only a very small bandwidth of wavelengths are reflected, but the Bragg relation is fulfilled across all the crystal surface, resulting in high reflection efficiency. Placing the x-ray source inside the Rowland circle decreases the collection efficiency of the crystal but also increases the accessible bandwidth. The downside of using a bent crystal is that the curvature of the crystal cannot be manipulated accurately enough to allow for angular changes during the experiment. Consequently, close-lying reference lines are needed to measure a transition wavelength using the dispersion relation on the PSD for each measurement.

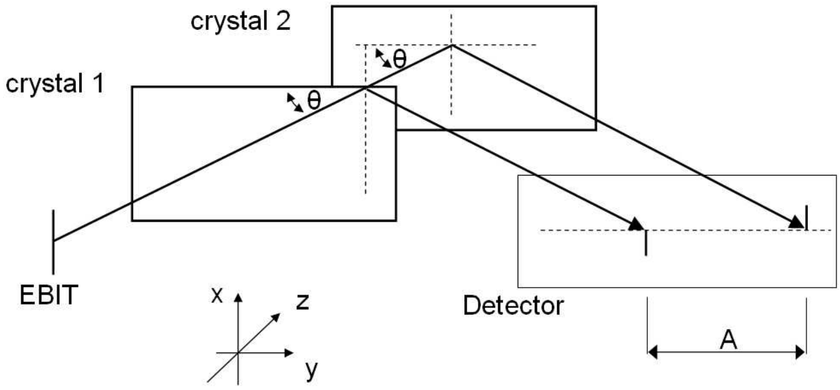

Figure 2.7: Principle of a quasimonolithic crystal arrangement for absolute wavelength measurements (from [KHFB97], modified). The Bragg angle and thus the wavelength of the radiation under study can be determined from the crystal lattice constant, the distance L of the reflecting surfaces and the distance A of the reflected x-rays.

An interesting possibility is the application of monolithic or "quasimonolithic" crystals [KHFB97, HFK$^+$98, TKB$^+$02]. In this setup, the reflecting surfaces of two flat crystals with the same lattice spacing are arranged in parallel at a short distance. X-rays are reflected on both surfaces, but as the x-rays reflected on the rear surface travel a longer distance before the reflection, two parallel beams are reflected for each incoming x-ray beam (see Fig. 2.7). With precise knowledge of the lattice spacing and the distance L of the two reflecting surfaces, one can accurately determine the Bragg angle θ and, thus, the wavelength of the incoming radiation from the parallel shift of the two reflected beams without the need for a calibration line by means of the relation

$$\sin\theta = \sqrt{1 - \left(\frac{A}{2L}\right)^2}\ . \tag{2.1}$$

Although flat crystals are used in this configuration, no collimation of the incoming radiation is necessary. The so-far best measurement using this technique was performed on Mg^{11+} [HFK$^+$98] at an EBIT, reaching an accuracy of 24 ppm. It is interesting to note that the measurement's uncertainty is dominated by limited counting statistics, and that systematic effects can be reduced below 1 ppm with this technique. Drawbacks of the method are that the detector position information needs to be known with high precision to accurately measure the distance of the two incoming beams, and that with decreasing Bragg angle the seperation of the reflected x-ray beams becomes larger, such that detector size limits the range of accessible energies.

In most cases, curved crystal spectrometers are preferred over flat crystal spectrometers for their $10 - 100$ times higher luminosity. On the other hand, it is worthwhile to exploit the fact that a flat crystal can be rotated without having to adjust other parameters, as it would be the case in a Rowland geometry. This allows the reference line to be separated from the transition of interest by several hundred eV. While the possibility to perform absolute wavelength measurements with a quasimonolithic setup is intriguing, the very limited spectral range is only one of the reasons why there are such few measurements performed using this technique. Nevertheless, two different schemes are presently prepared at the HD-EBIT to perform absolute wavelength measurements, one of which is using a quasimonolith and the other an improved version of the flat crystal spectrometer type described in this work. These schemes are discussed in detail in [Bra06].

Eventually, a flat crystal spectrometer type was used in the present work, the benefits of which will become more clear in the discussion of the choice of reference lines.

2.3 Choice of reference lines

When performing relative wavelength measurements, a reference standard needs to be chosen. The most easily accessible x-ray lines are emitted by K_α transitions in atoms that were excited by electron or photon impact. In fact, the wavelengths of the $K_{\alpha 1}$ transitions of copper (Cu), molybdenum (Mo) and tungsten (W) have been assigned defined values and act as x-ray wavelength standards in their respective energy range [MT00]. As the K_α transition energy from a neutral element with the nuclear charge Z lies very close to the Lyman-α transition energy in a hydrogenic ion with the nuclear charge $Z-1$, $E_{K_\alpha}(Z) \approx E_{Ly\alpha}(Z-1)$, these very accurately known lines are commonly used for calibration in x-ray spectroscopic measurements of the Lyman-α transition energies in H-like ions. However, the usefulness of K_α transitions as reference lines is limited despite the fact that some of these wavelengths are known with an accuracy approaching 1 ppm [HFD$^+$97]. As seen in Fig. 2.8 (data taken from [HFD$^+$97]), the K_α lineshapes are asymmetric due to a considerable amount of transitions occurring either in the presence of a so-called spectator hole (i.e. a missing electron) in an outer shell or with simultaneous shake-up or shake-off processes (i.e. creating additional vacancies) taking place. These multi-electron effects lead to satellites with only slightly different energies than the one of the unperturbed transition. Additionally, the relative line strength of the satellites is sensitive to parameters like surface pureness and the excitation mechanism [SOT$^+$04]. Some analytical techniques such as EXAFS, NEXAFS, etc. even make use of such de-

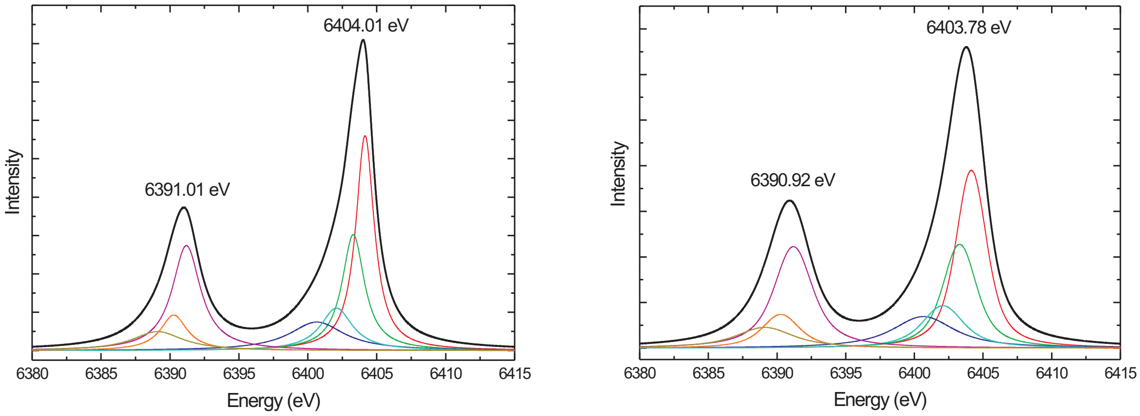

Figure 2.8: Left: empirical description of the Fe K_α lines using 7 Lorentz profiles to describe the satellites. Right: the same spectrum convoluted with a gaussian of 0.5 eV width to simulate the spectrometer response function. The energy values within the figures are the positions of the peak maxima.

pendencies for material studies. This line asymmetry, in combination with source broadening and the point spread function of the detection device, leads to shifts of the peak maxima that are hardly predictable or correctable. These shifts can easily become an order of magnitude larger than the error bar of the literature value of the line, as is shown at the example of the K_α spectrum of iron in Fig. 2.8, one of the elements with the most satellite-rich K_α lines. While most elements exhibit a lower degree of satellite contamination, the uncertainty values given in most of the high-precision wavelength measurements found in the literature that used these lines for wavelength calibration still have sizeable contributions from the reference lines.

This leads to the ironic situation that problems in the analysis of the accepted reference standard can eventually limit the achievable precision for a line needing sophisticated instrumentation to become accessible. This issue is already discussed in the literature, and there are proposals (e.g. [FKKM01, AGIS03] and references therein) to resolve the problem by changing the set of standard lines e.g. to Lyman-α transitions in hydrogenlike ions. The energy of these transitions can already be calculated with high precision, and the agreement between experimental data available and the predictions is very good, such that these calculations can be considered highly accurate.

In addition to this inherent problem of the current set of standard lines, these lines are difficult to access experimentally in an EBIT, for they have to originate from the same volume in space as the radiation under study when no entrance slits are used. In accelerator-based techniques one can place the source emitting the reference lines close to the ion beam. In an EBIT however, the magnetic field coils that are used to compress the electron beam, the cooling for the coils and the vaccuum assembly for the ion trap require much space, such that quite some experimental effort is necessary to integrate the reference source into the trap volume. For example, Tarbutt *et al.* [TCM$^+$00] inserted a vanadium wire probe into the Oxford-EBIT trapping region with the electron beam grazing the wire tip to produce the characteristic vanadium lines. Here, the line profile problem is compounded with limitations arising from the positioning accuracy of the wire, as two very different electron beam settings have to be used for calibration and measurement. A displacement of only $1\,\mu$m between the wire tip acting as calibration source and the trapped ions would lead to a systematic error of about 1 to 1.5 ppm if the setup of this work was used with this calibration scheme.

2.4 Finding an advantageous experimental setup

After the discussion of the available possibilites for all three components that are required for a high-precision measurement, the source, the spectrometer and the reference lines, the complete experimental setup can be addressed.

Using an EBIT to study highly charged ions by spectroscopic means is an obvious choice to make. With an EBIT giving access to essentially all charge states of all elements, the constraint of being limited to a small spectral range around an available reference line when using a curved crystal spectrometer is certainly unsatisfactory. This limitation effectively prevents one from studying many interesting transitions in helium- and lithiumlike ions which are the current benchmark systems for theory. Disregarding their low reflection efficiency, flat crystal spectrometers allow to use the EBIT to its full potential, and the possibilities they offer should be explored in more detail.

With interest in helium-like ions and the ability to cover a wide range of energies when using a flat crystal spectrometer, one should consider Lyman-α transitions in hydrogenlike ions as reference lines rather than the K_α transitions from neutrals. Recalling the need for corrections due to the asymmetric lineshapes of the K_α lines and the effort necessary to have them emitted from the EBIT trap volume, it is certainly more fruitful to abandon this reference standard entirely and use Lyman-α transitions instead. The Lyman-α spectra obtained at an EBIT are free of satellites (see Chapter 4.5.2), and no corrections or assumptions are involved when determining the line centroids. Studying transitions in helium-like ions at an EBIT, the Lyman-α transitions of the according element are available as well, without any further setup to be involved. Moreover, from atomic theory's point of view, electron correlation effects can best be studied by comparing transition energies in hydrogen-and helium-like systems with the same nucleus. It is therefore reasonable to use these lines as natural reference standard and a flat crystal spectrometer when measuring transition energies in the region of $1 - 10\,\mathrm{keV}$ at an EBIT.

In terms of electron beam current I_e, the HD-EBIT is at present the leading machine worldwide. I_e essentially defines the ionisation and excitation rates, as well as the number of ions that can be stored in the trap. As a result, the expected x-ray flux is comparatively high at the HD-EBIT, and the low reflectivity of the flat crystal is countered to some extent. Still, collimation of the incoming x-rays would lead to an unacceptable loss of intensity.

For this reason, a novel method for Bragg angle determination in flat crystal spectroscopy replacing entrance slits was developed and implemented in the flat crystal spectrometer built in [Bra03]. This new method is explained in the following chapter.

Chapter 3

The novel x-ray spectrometer

In order to reach an accuracy of better than $\delta\lambda/\lambda < 10^{-5}$ in measurements that require movements of both crystal and camera, the spectrometer built in [Bra03] had to be modified, implementing the novel method of position calibration developed cooperatively in this work and in [Bra06]. This chapter is devided into four parts, describing the general features of the spectrometer, the new method, its implementation and the data acquisition procedure.

3.1 The spectrometer setup

The x-ray spectrometer was designed to be directly attached to the EBIT to minimize x-ray absorption through window foils and to maximize the solid angle. Minimal x-ray absorption is reached by evacuating the spectrometer. To make it compatible with the EBIT vacuum it is designed as a ultra-high vacuum device. Figure 3.1 shows a schematic drawing with the most important components. The x-ray detector is a position sensitive charge coupled device detector (CCD or CCD camera) from Roper Scientific. The CCD chip contains 1024×1024 pixels ($24.6 \times 24.6\,\mathrm{mm}^2$ imaging area) with good to high quantum efficiency for photons of $300 - 5000\,\mathrm{eV}$ energy (Fig. 3.2). This detector is temperature stabilised to $-110°$C by a liquid nitrogen cooled Peltier element to suppress thermal noise well below the readout noise level. Besides the limited detector efficiency and the unavoidable loss of intensity by reflection from a crystal, the only additional loss of x-rays within the spectrometer is due to a $25\,\mu$m thin Be-window used to seperate the spectrometer vacuum from the several orders of magnitude better EBIT vacuum. The transmittivity of this window is shown in dependence of the incident x-ray energy in Fig. 3.3. A bypass valve ensures that the Be foil stays intact when evacuating the spectrometer.

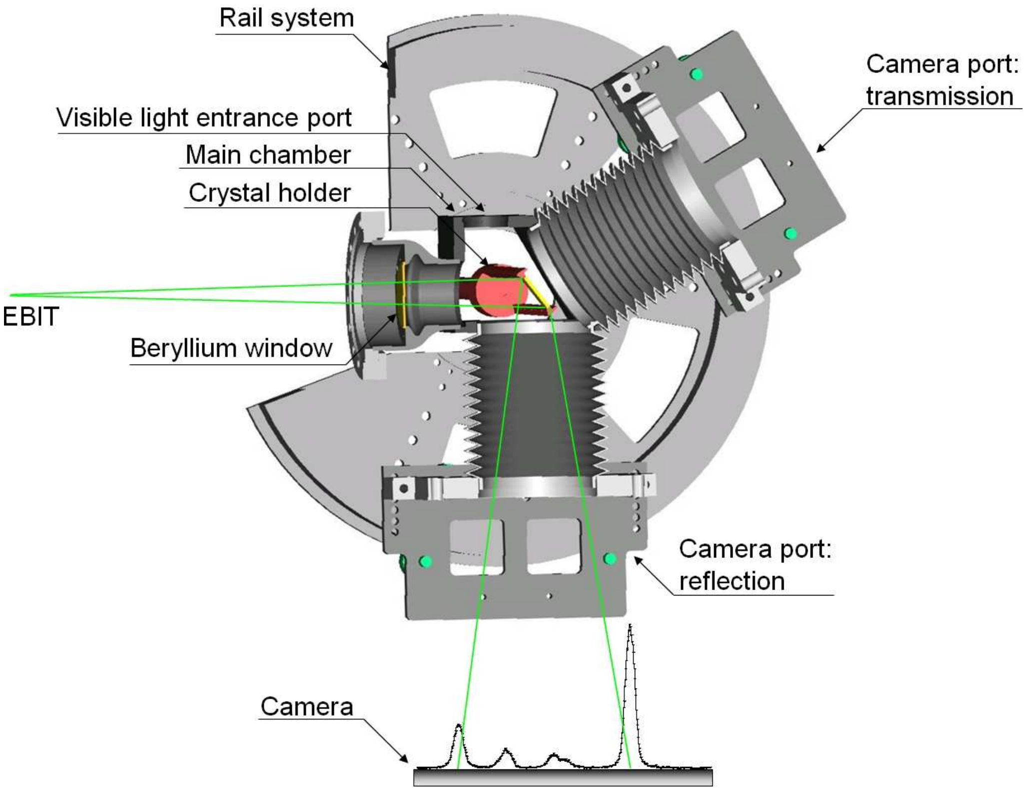

Figure 3.1: Schematic of the x-ray spectrometer. X-rays enter the main chamber of the spectrometer through a thin Be-foil. The x-rays are reflected (or transmitted) on a crystal which is positioned by the rotatable crystal holder. The CCD camera is mounted to either one of the movable camera adapters which are connected to the main chamber via bellows. In this work the spectrometer was used only in reflection mode. In this mode, the visible light beams needed for the position reference (see chapter 3.2) are coupled into the system through the top opening and reflected towards the crystal by a small mirror (not included in the figure). The exemplary spectrum in the figure was obtained with this configuration.

To maximize the energy range covered with one crystal, the CCD camera is connected to the rigid main chamber by either one of two flexible stainless steel bellows of large diameter, which are used as ports for the reflected or transmitted x-rays, respectively. Due to the flexible bellows, the CCD camera can be positioned according to the crystal's orientation by the use of stepper motors and a rail system, with the camera and the crystal rotating coaxially. On the top of the spectrometer chamber, an additional port originally intended for the connection of a pressure gauge is located. In this work, this port was used for the implementation of the new method of position calibration in the spectrometer.

The standard crystal holder is manufactured of high-strength aluminium alloy and holds up to six crystals, either of which can be selected without breaking the vacuum

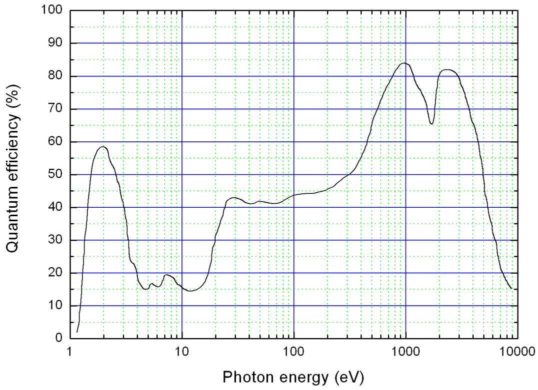

Figure 3.2: Typical quantum efficiency of CCD cameras of the type used in this work.

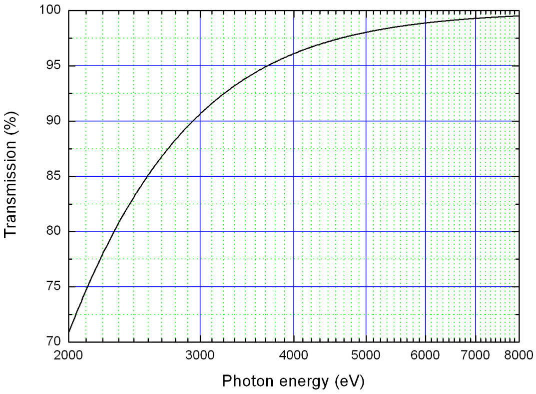

Figure 3.3: Transmittivity of a 25 μm thick Be-foil in dependence of the photon energy.

by the use of a vacuum Z-manipulator. The ability to change the crystals in measurements was intended to further extend the energy range covered by the spectrometer, but cannot be used in high-precision wavelength measurements due to the limited positioning reproducibility during crystal change. The Z-manipulator (and thus the crystal holder) is mounted on an ultra high vacuum (UHV) rotating platform driven by a stepper motor. The camera position is measured with a Heidenhain ERA 880C incremental ruler as described in [Bra03]. Originally the angular measurement system of the crystal angle was of the same type but had to be exchanged in order to reach an accuracy of better than $\delta\lambda/\lambda < 10^{-5}$. The new readout system of the crystal angle is an absolute angular encoder (Heidenhain RON 905) with a specification of $(5 \cdot 10^{-5\circ})$ absolute accuracy. A more detailed description of the mechanical setup of the spectrometer is found in [Bra03].

3.2 A novel method of x-ray reflection position calibration

The normal operational modes for a flat crystal spectrometer are to either use the energy dispersive mode, where a position sensitive detector is used to simultaneously record a spectrum of only a few 10 eV range, or to use entrance slits to define the x-ray reflection position on the crystal, and then to rotate the crystal and the detector in order to reflect another x-ray line that may be seperated from the first one by several 100 eV. As discussed in Chapter 2.2 neither mode is a favourable choice, since using the energy dispersion imposes strong limits on the covered energy range, while entrance slits allow coverage of a wide range of energies but lead to unacceptable losses of x-ray intensity through collimation.

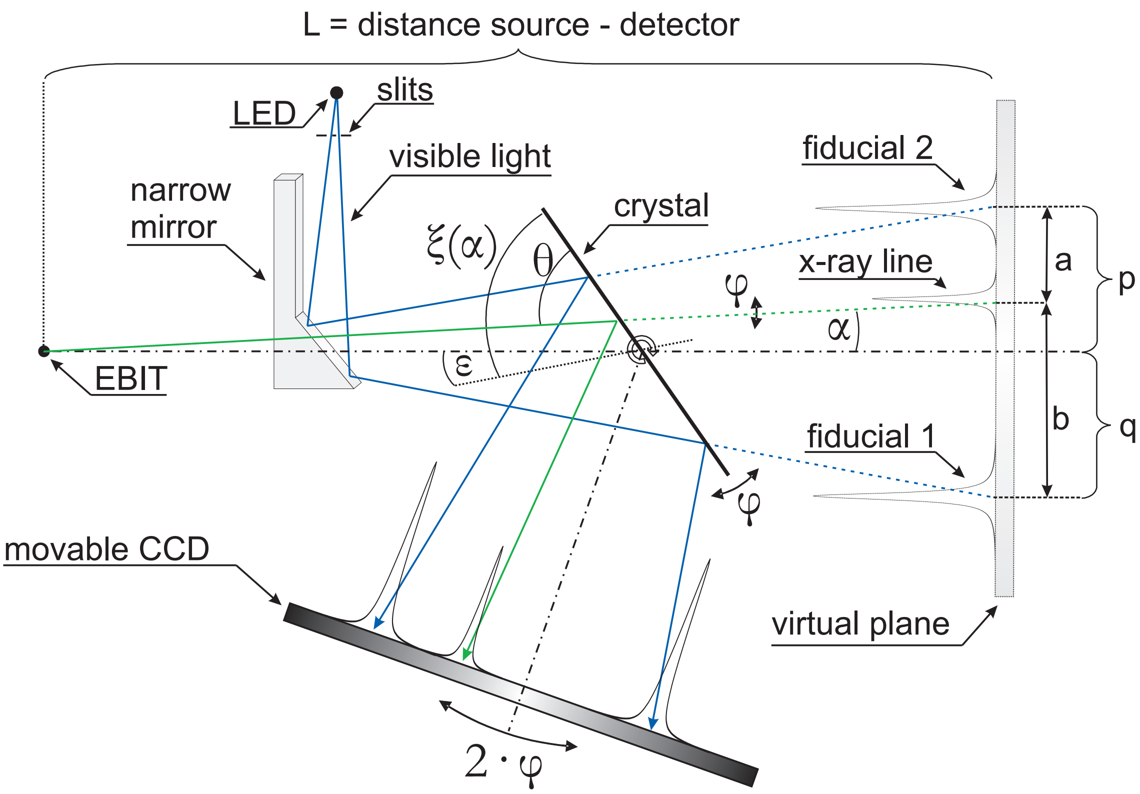

Figure 3.4: Principle of the new method of position calibration. The horizontal dash-dotted line represents the main axis of the instrument defined by the x-ray source (here: the EBIT) and the crystal rotation axis. The EBIT generates x-rays with a defined energy; a light emitting diode (LED) and two slits are needed to generate two beams of visible light that are coupled into the x-ray beam path by a small mirror. All items on the right hand side of the crystal are the projected positions of the intersections of the reflected x-rays and the visible light beams with the camera surface, with the crystal surface taken as a symmetry plane. They are included in the figure as they allow an easier understanding of the geometrical dependencies. More explanations to the figure are found in the text.

The decisive innovative idea to resolve this problem as well as its practical realisation presented in this work was developed in close collaboration with J. Braun [Bra06]. The central point of the method is to determine and describe the reflection position of an x-ray line on the crystal in dependence of the crystal's orientation rather than to define the reflection position through collimation. Thus, a certain energy range can be observed simultaneously on a position sensitive detector without any collimation plus the crystal can be rotated in order to cover a large energy range, thereby combining the advantages of the previously seperated methods. This was achieved by making use of two beams of visible light which serve as position references, or fiducials, as illustrated in Fig. 3.4 and explained in the following.

The main axis of the spectrometer is defined by the position of the x-ray source and the crystal rotation axis, and the total distance between the source and the detector (including the reflected beam's path length) along this axis is called L. X-rays of a defined energy emitted by the EBIT are reflected by the crystal under the corresponding Bragg angle θ. The angle α between the incoming x-rays and the main axis, *i.e.* the (projected) reflection position on the crystal, depends on the crystal's orientation. A change in the crystal's orientation by an angle φ also shifts the direction of the incoming x-ray line by φ with respect to main axis. Even if the camera angle is simultaneously changed by $2 \cdot \varphi$ to keep the camera position fixed in the virtual plane, the position at which the x-ray line is detected on the camera changes. On the other hand, the polished crystal surface acts as a mirror for the visible light beams and reflects them under any angle. Thus, a change in the crystal's orientation by φ with simultaneous change of the camera angle by $2 \cdot \varphi$ has no effect on the positions on the CCD at which the visible light beams are detected (the CCD camera is sensitive to both x-rays and visible light). Consequently, the relative position of the x-ray line with respect to the two visible light lines on the CCD yields full information about the crystal orientation. In particular, finding identical distance proportions a/b of the separation of the x-ray line from the two visible light lines in any two measurements implies identical reflection positions on the crystal.

The crystal angle $\xi(\alpha)$ is measured with respect to an arbitrary axis that differs from the main axis by the unknown but fixed offset angle ϵ. To find the function describing the change of the distances a and b of the x-ray position relative to that of the two fiducials in dependence of $\xi(\alpha)$ it is necessary to introduce the the distances of the two fiducials to the main axis p and q. The movement of the x-ray line with respect to the two fiducials can be described as

$$\left|\frac{a}{b}(\alpha)\right| = \left|\frac{p - L\tan(\alpha)}{q + L\tan(\alpha)}\right| = \left|\frac{p - L\tan\left[\theta_i^* - \xi_i(\alpha)\right]}{q + L\tan\left[\theta_i^* - \xi_i(\alpha)\right]}\right| \tag{3.1}$$

where the index $i = \{1, 2, \dots\}$ denotes different wavelengths and θ_i^* is the measured angle at $\alpha = 0$, i.e. the special case where the x-rays are travelling along the main axis of the instrument and $a/b = p/q$. If the device measuring the crystal angle could be set up in such a way that the crystal angle is measured exactly with respect to the main axis ($\epsilon = 0$), θ_i^* would be the real Bragg angle θ_i, hence the denotation. However, adjusting the zero setting of the angular measurement scale to the main axis to ppm precision is hardly achievable, and the offset angle ϵ has to be considered: $\theta_i^* = \xi_i(\alpha = 0) = \theta_i + \epsilon$. Therefore, only the difference γ between two Bragg angles can be measured accurately: $\gamma = \theta_j^* - \theta_i^* = (\theta_j + \epsilon) - (\theta_i + \epsilon) = \theta_j - \theta_i$. Figure 3.5

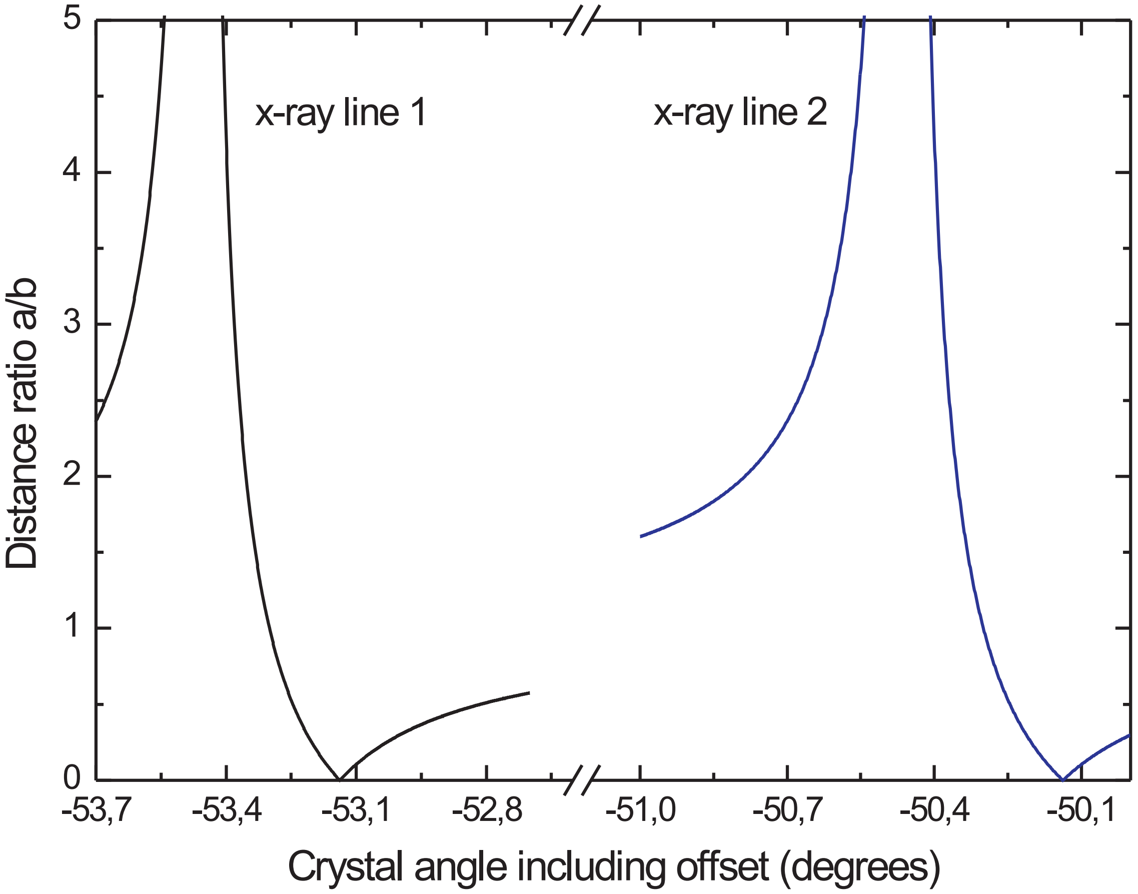

Figure 3.5: Equation 3.1 plotted for two different x-ray lines; all parameters are chosen to be similar to the data analysed in chapter 4. Either line can be used as a reference for the other.

shows Eq. (3.1) for two different Bragg angles with the same geometrical parameters p, q and L in dependence of the measured crystal angle ξ.

In a measurement a set of x-ray exposures is taken for each x-ray line under study. Each exposure within a set is taken at a slightly different crystal angle than all others, and depending on the crystal angle, the x-ray line appears at different distance ratios a/b on the detector, following the curves shown in Fig. 3.5. The unknown parameters of Eq. (3.1) can then be fitted to those datapoints (see chapter 3.2.1 for some important details about the fitting procedure). A divergence in the ratio a/b implies that the x-ray line is detected at the same position on the camera as fiducial 1, analogously a zero value implies overlap of the x-ray line with fiducial 2. In the following, the method of position calibration described above will be referred to as the a/b-method.

3.2.1 Properties of the distance ratio curves

Since only the difference in Bragg angles of two lines can be measured accurately with the a/b-method, it is necessary to discuss Eq. (3.1) in more detail, as two sets of data have to be analysed simultaneously. The parameters p, q and L do not depend on the x-ray energy under study but only on the geometrical properties of the instrument and have thus to be shared parameters in the analysis of any two different x-ray lines. With these parameters shared, the two curves have exactly the same shape and a difference in the only remaining degree of freedom θ_i^* results in a horizontal shift, as can be seen in Fig. 3.5. Consequently, the horizontal distance of the two curves is the same for all distance ratios a/b. This implies that the difference γ in Bragg angles of two x-ray lines

$$\gamma = \theta_j - \theta_i = \theta_j^* - \theta_i^* = \xi_j \left(\frac{a}{b} = \frac{p}{q} \right) - \xi_i \left(\frac{a}{b} = \frac{p}{q} \right) \tag{3.2}$$

can be obtained at any value of $a/b = p/q$. Thus, the values of p and q can be chosen arbitrarily, with the constraint that the sum $p + q$ is equal to the distance of the two visible light fiducials. Hence, in the analysis of the experimental data the values of p and q have been set to $p = q = (p + q)/2$, meaning that the difference in Bragg angles of two lines has been obtained in the centre between the two light fiducials, at $a/b = 1$.

3.2.2 Remarkable features of the a/b - method

Comparing the a/b-method with the use of entrance slits that define the reflection position[1] of an x-ray line on the crystal, one should recall that the more entrance slits are closed, the better the reflection position on the crystal is defined, and the higher the accuracy of the measurement becomes. Due to the collimation x-ray photons are lost, and only a very small region of the total spectrum can be observed. On the other hand, a fit of the analytical function (3.1) to data taken with the a/b-method is comparable to the use of a tightly closed entrance slit, as the distance ratio a/b is an indicator for the reflection position of an x-ray line on the crystal. However, when employing the a/b-method, a wide spectrum is observed simultaneously, and every single photon detected at any distance ratio a/b adds to the overall statistical significance of a measurement.

---

[1] The term “reflection position on the crystal” actually refers to the *projected* reflection position on the crystal, *i.e.* the angle between the incoming line and the main axis (see Fig. 3.4).

One should also note that the important measured quantity a/b is a ratio of distances. Therefore, the absolute values of a and b in units of metres are not important, and uncertainties arising from the limited knowledge of the exact pixel size of the CCD camera do not play a role for the measurement of the distance ratio. Furthermore, since the x-ray line is forced to be reflected/detected at different positions of the crystal/camera (*i.e.* different crystal/camera angles), inhomogeneities in the crystal and the camera surfaces are averaged out. Also, while the crystal angle needs to be measured with high accuracy, it does not need to be set to certain distinct positions but only to slightly modified positions every time, thus simplifying the positioning process. Eventually the camera angle, or its position, is not needed for the data analysis at all, since the visible light fiducials are acting as position references.

3.2.3 Systematic error sources

In Fig. 3.4 perfect alignment of all elements is assumed. In particular, possible eccentricities of the crystal or the camera to the central axis were not considered hitherto. If there were no eccentricities, the position of the visible light beam origin could be arbitrary, as for any crystal rotation the projected image of the light fiducials in the virtual plane stays at exactly the same position. With eccentricities, however, the total length L used in Eq. (3.1) changes depending on the crystal or camera angle, as illustrated in Fig. 3.6. Consequently, even if the x-ray line is reflected at the same position on the crystal as another x-ray line, the measured distance ratios a/b of the two lines are different by a small amount, as the change in L depends on the crystal orientation and camera position. The effect of eccentricities can be countered by placing the source emitting the visible light beams at the same position as the x-ray source. In this (and only this) case the ratio a/b is preserved for all changes ΔL.

A thorough analysis of the effect of eccentricities and visible light source positioning has been performed in [Bra06] by a ray tracing simulation of the beampaths in the spectrometer. According to this simulation, with the geometry and measured eccentricities of the crystal and camera motion, the most critical issue is the misalignment of the visible light source in direction perpendicular to the main axis (indicated by Δy in Fig. 3.7). A displacement of only a few millimetres in this direction already has a sizeable effect on the measured distance ratio a/b (and thus the difference in Bragg angles obtained from the measurement), while the effect of a displacement Δx in direction of the main axis is more than an order of magnitude lower. However, in this work the observed difference in Bragg angles obtained by employing the a/b-method corresponds only to the small difference $\Delta\lambda$ between the line under study

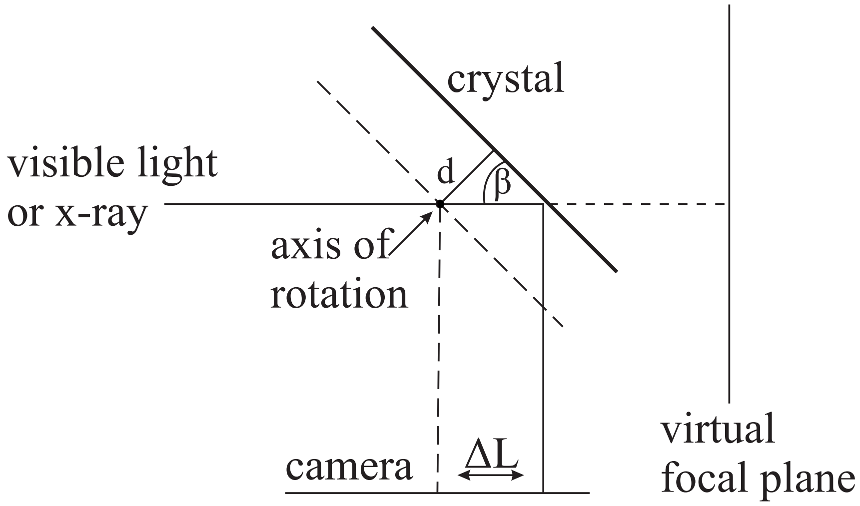

Figure 3.6: Schematics to show the effect of eccentricities on the a/b-method. An eccentricity of the magnitude d in the crystal position leads to a longer pathlength travelled by an x-ray line of $\Delta L = \mathrm{d}/\sin(\beta)$. In the virtual plane, the x-ray appears at the centre of the camera, which is clearly not the case on the detector. The effect of camera eccentricity is analogue.

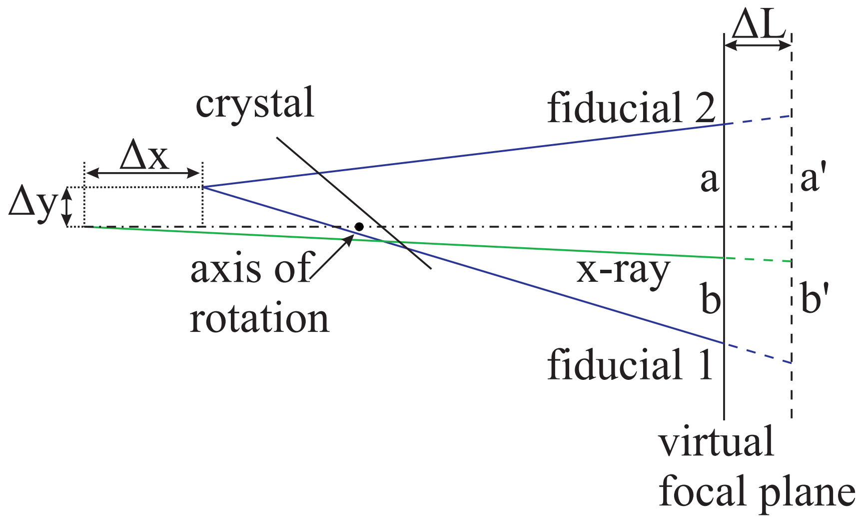

Figure 3.7: The effect of the change in beam path lengths arising from crystal or camera eccentricities. If the visible light source is displaced by $(\Delta x, \Delta y)$, the distance ratio $a/b \neq a'/b'$ is different for same reflection points at different crystal and camera angles.

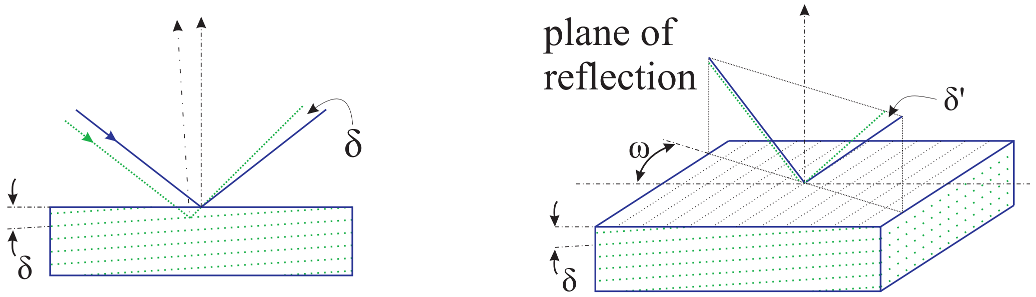

Figure 3.8: Left: schematic showing the effect of an angular offset δ between the crystal lattice (green dotted lines) and the crystal surface (blue box). Incoming parallel beams of visible light (blue, full lines) and x-rays (dashed lines) are reflected by different planes and the exiting beams are nonparallel. Right: the same for the general case in isometric view. Turning the crystal by the angle ω around the surface normal leads the tilt angle δ appearing only in a projection, thus the angle between the outgoing x-ray and visible light beams changes to δ'.

and a reference line. The magnitude of the wavelength under study is determined by the reference line, and the impact of the uncertainty in the Bragg-angle difference γ on the total uncertainty of the measurement scales with $\Delta\lambda/\lambda$. Thus, while the uncertainties in γ due to the alignment of the visible light source determined in this work are of the order of 50 ppm, the overall result is affected to only ≈ 3 ppm. Still, for the absolute wavelength measurements aimed at in [Bra06] the spacial overlap between the EBIT and the visible light source must be ensured and is subject of current work.

Another question arising from the use of visible light in the a/b-method is the effect of a "tilt" angle δ between the crystal lattice (reflecting x-rays) and the crystal surface (reflecting visible light), as illustrated in Fig. 3.8. If the two reflecting planes are nonparallel, an additional angular tilt δ is imposed on the beampaths between the x-ray lines and the visible light beams. Even in crystals of good quality the tilt angle can amount to as much as $\delta \leq 0.1°$. Quite similar to the visible light source positioning problem described before, also in this case the distance ratio a/b is changed and the geometry depicted in Fig. 3.4 is not fully valid anymore. However, the ray tracing spectrometer simulations have shown that for this work's measurements the tilt angle effect is negligible in comparison with the uncertainties arising from the visible light source positioning.

The absolute wavelength measurements to be reported on in [Bra06] have stronger alignment requirements, and the effect of the tilt angle on the measurement can no longer be neglected. The size of the tilt angle cannot be measured with high accuracy, thus completely correcting the measured angular difference for the tilt angle contribution is not possible. The solution to this problem is to arrange the crystal in its holder in such a way that the tilt orientation is perpendicular to the plane

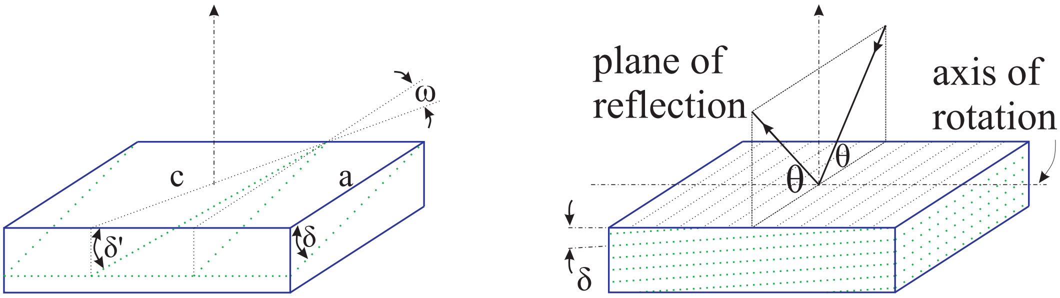

Figure 3.9: Left: schematic to clarify the dependence of the projected tilt angle δ' of the total tilt angle δ and the angle ω between the incoming beams (not shown in the figure) and the tilt orientation (side view of Fig. 3.8). One obtains $\tan\delta' = \tan\delta\cos\omega$. Right: setting crystal rotational axis to make the plane of reflection (both x-rays and visible light beams) perpendicular to the tilt orientation, *i.e.* $\omega = 90$ degrees, the influence of the tilt angle on the measurement is nullified.

spanned by incoming and reflected beams of visible light and x-rays, as illustrated in Fig. 3.9. For this purpose, the tilt angle orientations of several crystals are currently measured by the x-ray optics group of Prof. Förster in Jena.

A more detailed analysis of these effects along with a description of the geometrical simulation of the instrument and a modified data fit function including the tilt angle as a fit parameter will be given in [Bra06].

3.3 The modified spectrometer setup

In order to implement the a/b-method into the spectrometer built in [Bra03], two beams of visible light had to be generated and coupled into the x-ray beam path, projecting them onto the crystal and the camera. In the first tests the spectrometer was directly attached to the EBIT main vacuum chamber and, thus, the free top port of the spectrometer chamber (Fig. 3.1) had to be used for the visible light beams. To do so, a quartz window flange was mounted on this vacuum port. On the vacuum side, this window supports a 10 cm long aluminium holder shaped as shown in Fig 3.4 which allows to place the mirror centered in front of the crystal. This mirror blocks part of the incoming x-ray radiation (Fig. 3.10).

In order to generate the visible light beams a double-slit aperture was illuminated with an LED. To prevent superposition of unwanted diffraction patterns generated by the slits around the two peaks appearing on the CCD a quartz lens with appropriate focal length was used to image the slit apertures, after being reflected on both the mirror and the crystal onto the CCD camera. The assembly is mounted in a cylindrical aluminium encasing on the top port of the spectrometer. During first

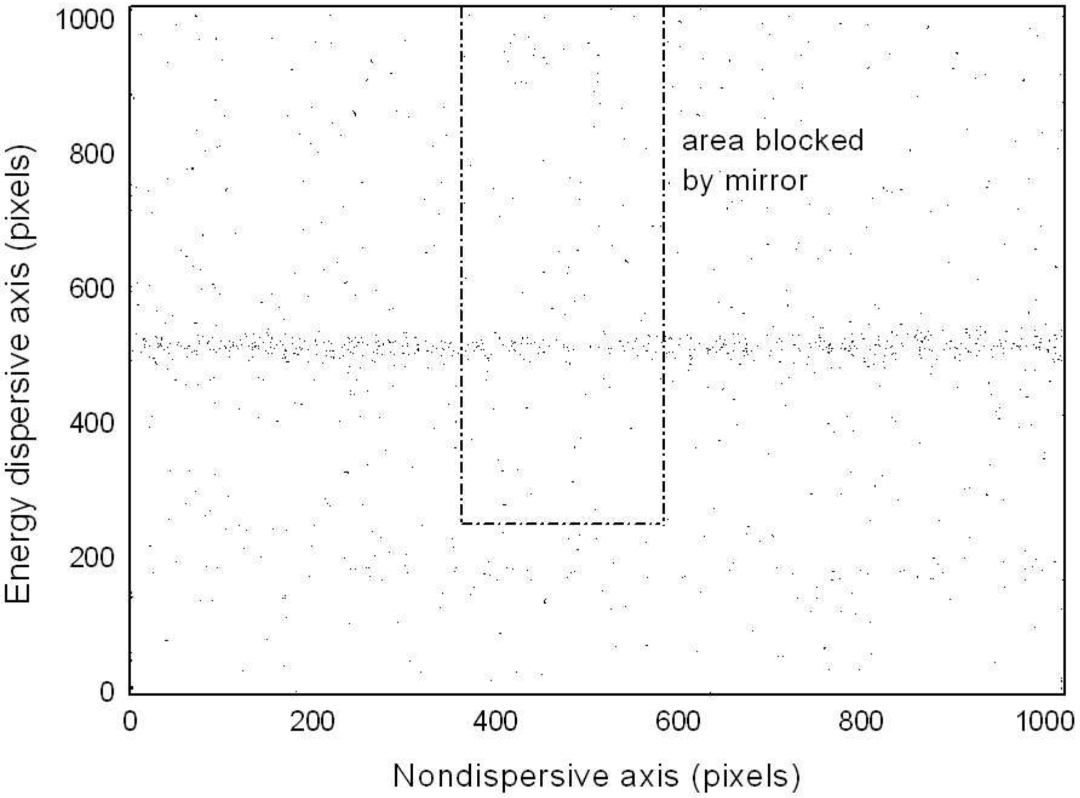

Figure 3.10: Image of an x-ray line (events around pixel row 520 on the energy dispersive axis) on the CCD detector. The mirror used to couple the visible light beams into the spectrometer has negligible transmittivity for x-rays of $1000 - 10000\,\mathrm{eV}$ energy and thus blocks part of the incoming radiation. This can be seen as a shadow in the center of the image. Events registered within this area are due to x-rays passing the mirror on a oblique trajectories.

experiments the need for a close spatial overlap between the projection of the visible light source and the EBIT ion cloud was not realised, thus the distance between the visible light source and the CCD camera was not optimal and has to be taken into account as a source of systematic error in the analysis of these measurements. The positioning procedure for each element is described in the following.

When the spectrometer was set up at the EBIT, before the initial pump-down both the crystal and the CCD positions were separately vertically aligned by means of a water level. With this rough setting of the angular scale to zero, a strong x-ray line within the covered spectral region (in this case this was the line of interest, the $1s2p\ ^1P_1 \rightarrow 1s^2\ ^1S_0$ resonance transition in He-like argon) could be found easily by rotating crystal and CCD camera to the calculated angles. Then, by changing the crystal orientation by small angles φ, the x-ray line reflection position on the crystal was scanned, allowing one to find the crystal angles at which the x-ray line hits the

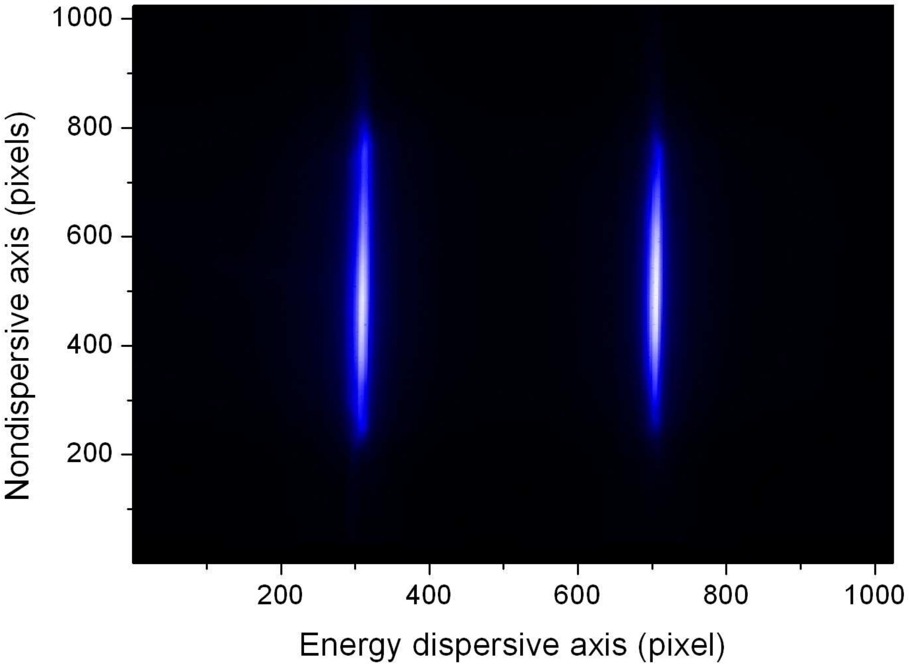

Figure 3.11: Image of the two visible light fiducials used for position calibration in the *a*/*b*-method. Note that, in contrast to Fig. 3.10, here the x-axis is the energy dispersive axis.

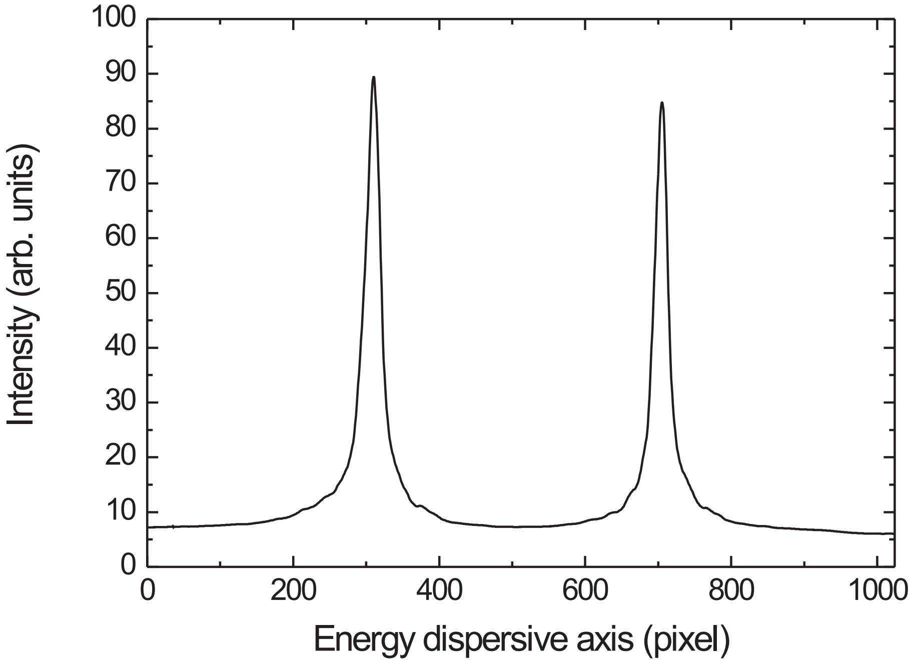

Figure 3.12: Projection of 3.11 on the energy dispersive axis of the CCD.

crystal edges, *i.e.* where the signal became weaker and eventually disappeared at either side. With this information, the crystal and the camera could be oriented such that the x-ray line was reflected well in the crystal's centre and detected in the central region of the camera, and the calibration of the angular readings was improved (for historical reasons the vertical axis was chosen as the zero axis of the crystal's angular measurement). Finally, the positions of the LED, the slit aperture and the quartz lens were adjusted to obtain two distinct peaks centred around the x-ray line on the camera, as shown in Fig. 3.11.

Using this procedure the misalignment of the visible light source in vertical direction (Δy in Fig. 3.7) is estimated to be smaller than 1 mm. The displacement in direction Δx depends on the length of the beamline connecting the spectrometer with the EBIT and was taken into account in the estimation of the error contribution in the simulations. For the reasons mentioned above, the implementation of the a/b-method used in this work is still not perfect. Nevertheless, even with the present deficiencies of the setup, the measurements performed in this work constitute the most accurate measurements on transitions in helium-like ions to date.

3.4 Data acquisition

In order to obtain data points for the a/b distance ratio curves, a measurement sequence needs to be set up. This sequence consists of a number of iterations. In each iteration the crystal is rotated such that each one of the x-ray lines under study is reflected from a similar reflection position on the crystal. In a typical sequence, two x-ray lines, the calibration and the unknown line, are measured alternately, in order to reduce possible effects of long term drifts. With every movement of the crystal, the camera is moved accordingly. At their designated positions, an exposure of typically $15-60$ minutes (depending on the x-ray line strength) is made. Before and after every x-ray exposure, a 5 second image of the visible light fiducials at the very same crystal and camera positions is recorded. All three images taken at one position (2× fiducials and one x-ray exposure) are saved to disk in ASCII format. During all exposures the crystal and camera angles are measured every second and stored in separate datafiles at the image file location.

In the first iteration, the crystal positions are chosen such that the x-ray lines appear close to fiducial 1. In each following iteration the crystal position is modified by $\approx 0.01°$ as compared to the previous crystal angle to make the x-ray lines approach fiducial 2. The complete procedure including filling liquid nitrogen to the camera's dewar at regular intervals, angular measurement, camera exposure and readout as well as the stepper motor control is automatised and controlled by means of a LabView programme. In this way, hundreds of exposures over periods of several days are acquired without operator intervention. The EBIT laboratory access is restricted during the measurement, so that temperature changes and accidental displacements are avoided as good as possible. The crystal and camera positioning process is programmed to approach the target positions always from the same direction with the same speed. Thus, the relation between the crystal orientation and the angular reading of the crystal is affected by slip effects in the stepper motor, transmission and rotating platform in always the same way, allowing one to minimise them as a systematic error source. Overall, the full automatisation ensures stable laboratory conditions over the whole measurement time without the need of any user interaction. The interface of the spectrometer control program is found in appendix A.1.

Chapter 4

Data analysis and results

In this work, the first high-precision measurement employing the a/b-method was performed. This chapter first gives a detailed description on how the x-ray spectra are analysed, with emphasis on issues like background linearity and line fitting that are prone to systematic errors. After a detailed description on how the visible light images that yield the position references (fiducials) are analysed the process of obtaining the data points on the a/b distance ratio plot is explained. Then, the measurement and analysis of the $1s2p\ ^1P_1 \rightarrow 1s^2\ ^1S_0$ and the $1s2s\ ^3S_0 \rightarrow 1s^2\ ^1S_0$ transitions in He-like argon as well as the Lyman-α_1 transition in hydrogen-like chlorine with respect to the Lyman-α_1 transition wavelength in hydrogen-like argon are presented and discussed.

4.1 X-ray spectrum analysis

A key point of the x-ray spectrum analysis is to understand the properties of the CCD detector used. Table 4.1 lists a number of its important specifications. Each pixel on the CCD chip is in itself an energy resolving semiconductor detector. This energy information can be used to discern whether an event was caused by thermal noise, a photon of the expected energy or a cosmic ray passing through the detector. To produce an electron-hole pair in silicon, 3.62 eV energy are needed at 300 K temperature [Leo93]. Hence, an incident x-ray photon of E_{ph} energy can promote a maximum number of electrons equal to $E_{ph}/3.62\,\mathrm{eV}$ from the valence band to the conduction band, that are then stored in a capacitor for digitisation. One “count” generated by the analogue-to-digital converter (ADC) during readout corresponds to 5.3 electrons. Thus, about 170 counts are generated in a pixel by an incident photon of 3300 eV energy. The biggest contribution to the background of the CCD

Table 4.1: Specifications of the Photometrics Series 300 camera.

Camera	Roper Scientific (Photometrics) CH 360
CCD-chip	SITe 003B back illuminated without AR coating
Sensitive area	$24.6 \times 24.6\,\mathrm{mm}^2$; 1024×1024 pixels
Pixel size	$24 \times 24\,\mu\mathrm{m}^2$
Dark current	< 1.45 electrons per pixel and hour (at −110°C)
Gain factor	5.3 electrons per shade of grey ("count")
Preamplifier noise	12.1 electrons
Dewar volume	1.1 liter

images is due to the digitisation of the preamplifier bias voltage that results in a fixed offset of 462 ± 3 counts per pixel. The specified thermal noise at the operating temperature of −110°C is lower than one count per pixel and hour.

Figure 4.1 shows a spectrum of the Lyman-α_1 and Lyman-α_2 transitions in H-like argon, with transition energies of about 3323 eV and 3318 eV, respectively. The histogram of the signal height distribution in Fig. 4.2 is generated only from the region of the CCD where the two lines appear. While the photon peak appears close to the expected $462 + 170 = 632$ counts, it can be seen from the histogram that only comparatively few photons deposit all their energy in a single pixel. Consequently, the lower level of the signal discriminator window has to be set closely above the background level (see below) for the best signal-to-noise ratio. The upper level of the discriminator window is set to just above the photon peak energy. For the data analysis all pixels that show only noise level (below lower discriminator level) or indicate impact of high energetic cosmic particles (above higher discriminator level) are disregarded. All other pixels are treated equally, *i.e.* as a single event. Double hits on a single pixel are not very frequent, and so their contribution to the true signal can be ignored with negligible losses.

Since pixel defects or a non-homogeneous background can lead to asymmetric lineshapes and, thus, to an error in the line centroid determination, a more thorough characterisation of the CCD camera background noise without the discrimination procedure mentioned above is necessary. For the background analysis, about 200 exposures with different exposure times have been made at slightly different camera temperatures. Averaged background data files were generated by first tabulating the number of counts found in each pixel in all data files of same exposure time and camera temperature. To avoid events generated by cosmic particle impact from spoiling the average number of counts in these tables, a preliminary average excluding the

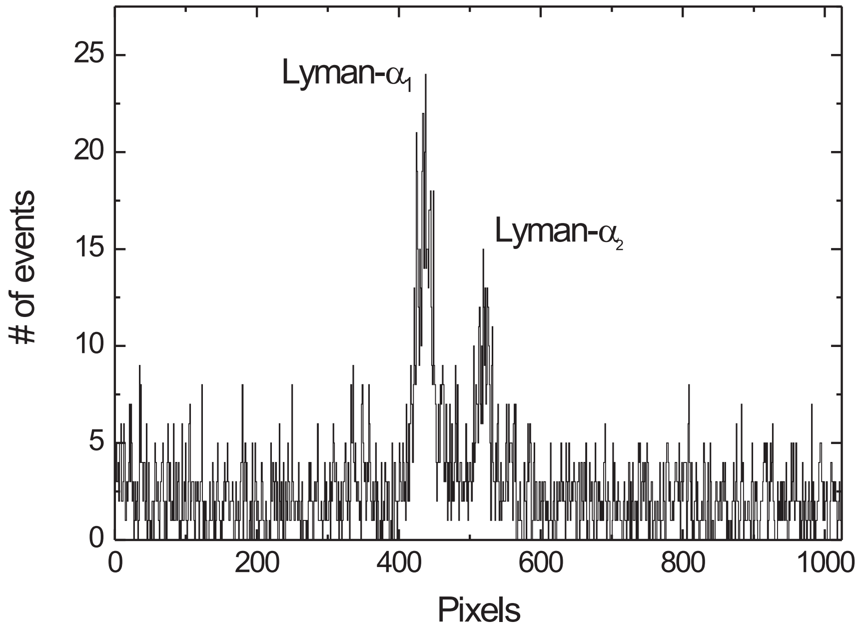

Figure 4.1: Lyman-α spectrum of H-like argon obtained at the HD-EBIT (60 min exposure time). Each event represents one pixel that contained a number of counts within the discrimination window.

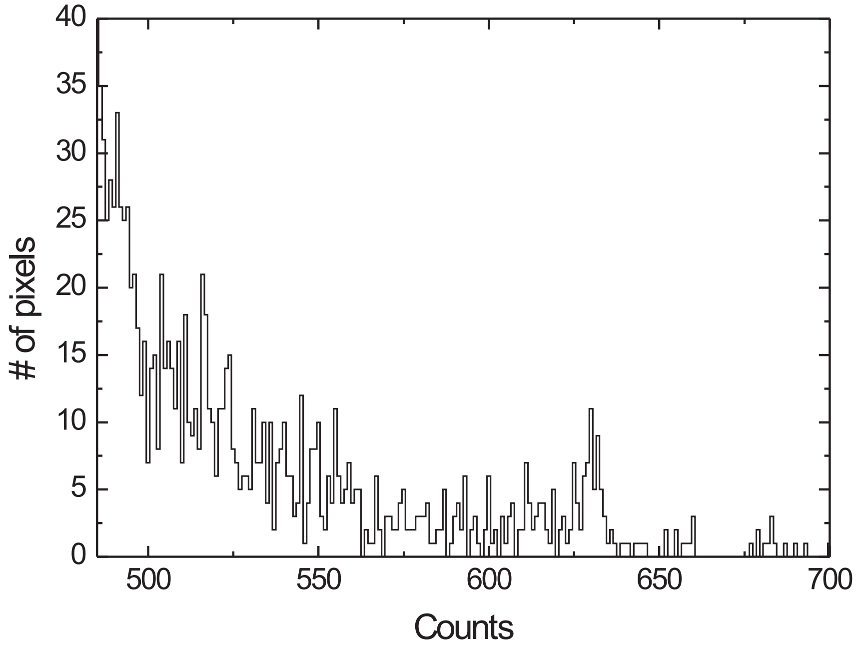

Figure 4.2: Histogram of the events in the spectrum of Fig. 4.1. Only the area where the two Lyman-α lines appear was included in the histogram, *i.e.* pixel rows $400 - 600$.

two highest values in the table was created. Then, the final average of the counts per pixel was obtained excluding events that were outside ±2 standard deviations of the preliminary average (*i.e.* if a pixel was not hit by a cosmic particle in any of the exposures, the average is built from the counts found in all available files).

In the background analysis, four defect pixels were found on the CCD showing a roughly linear increase of the count number with exposure time. In the coordinate space (energy dispersive axis, nondispersive axis), these are the pixels $(612, 160)$, $(665, 866)$, $(240, 349)$, and $(241, 349)$. As seen in Fig. 3.11, the visible light fiducials are located roughly at the pixel rows 300 and 700 in the projected images, thus only the first two pixels lie in the region where the x-ray lines are likely to appear in the measurement. Since the x-ray line is forced to move between the two visible light fiducials in a measurement, *i.e.* in the region between rows 300 and 700, these defect pixels do not lead to a systematic shift of any specific line and can, hence, be ignored.

Apart from the above mentioned four damaged pixels in the central CCD region, there are a number of pixels distributed at the two edges of the nondispersive axis that also show an increased noise level, and also neighbouring pixels are affected by their dark current at longer exposure times. When integrating, *i.e.* projecting, along the nondispersive axis of the image these "hot" areas lead to the appearance of artifact peaks in the spectrum. Additionally to these small areas, there is a very strong general increase of the background level on two edges of the chip which was aligned in such a way to make them the two extremes of the nondispersive axis (Fig. 4.3). The origin of this increase is believed to be a timing problem of the readout electronics. As will be shown later, this increased background does not affect the energy dispersive axis and thus the symmetry of the detected lines, since the energy dispersive axis is affected rather homogeneously. The drawback of the increasing background level is, of course, that the larger the area of the CCD one wants to use is, the higher one has to set the lower discriminator level in order to suppress it. This reduces the available number of events, as most photons deposit only small amounts of energy in one pixel (Fig. 4.2). Thus, the signal to noise ratio can be improved by disregarding ≈ 200 pixel rows on the right hand side of Fig. 4.3 and lowering the discriminator level accordingly. In the data analysis of this work, however, the choice was to use the whole available CCD surface rather than to increase the already good signal to noise ratio. Still, the pixel defects in the outermost regions of the CCD had to be cut away, and thus the first 4 and last 30 pixel rows of the nondispersive axis (as shown in Fig. 4.3) were excluded when projecting the x-ray spectra.

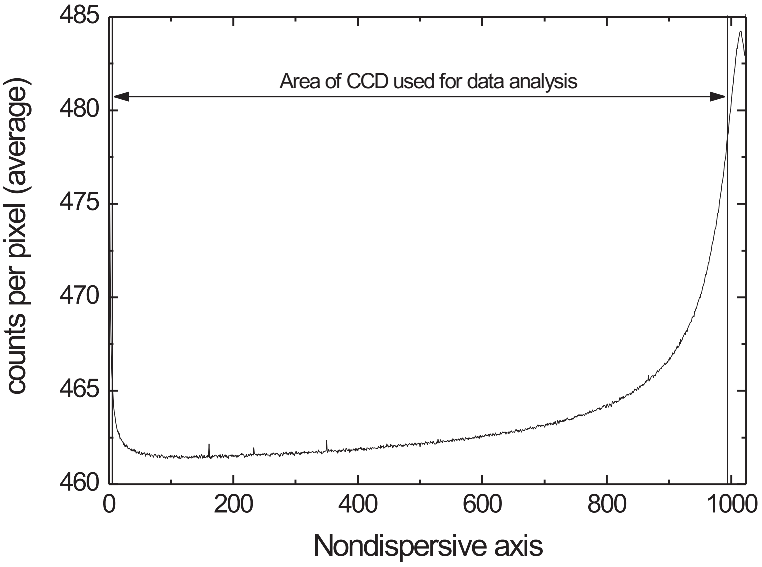

Figure 4.3: Average background projected on the nondispersive axis of the CCD. For the data analysis in this work, only the outermost regions of the CCD were excluded. Apart from the high background level, these regions contained small areas with "hot" pixels, leading to artifact peaks when projecting on the energy dispersive axis.

Except for the need for a higher discrimination level, the x-ray spectra are hardly affected by the fact that the background is not constant along the nondispersive axis. Figure 4.4 shows the projection of the background files of the four different exposure times at a camera temperature of −110°C onto the energy dispersive axis. As a consequence of inhomogeneities in the background levels along the nondispersive axis as well as in the projection onto the energy dispersive axis, an increase of the background can be seen at the low-energy end of the spectrum. Linear fits to the region where the x-ray lines appear in the measurement (between pixel 300 and 700) in all four spectra of different exposure times are shown in Fig. 4.5. The slopes of these fits are found in Tab. 4.2. The resulting reduction of $(1.74 \pm 0.33) \cdot 10^{-4}$ counts per pixel leads to a decrease of about $4 \cdot 10^{-3}$ counts over the width of an x-ray line (typically about 25 pixels), which is negligible compared with the $10 - 170$ counts generated by a real event. Thus, the background is sufficiently constant in the region where the x-ray lines appear and does not notably affect the line symmetry.

Table 4.2: Background slopes obtained by the linear fits in Fig. 4.5.

Time	15 min	30 min	45 min	60 min
slope $[\frac{counts}{pixel} \cdot 10^4]$	$-1.66(30)$	$-1.74(33)$	$-1.45(34)$	$-1.41(38)$

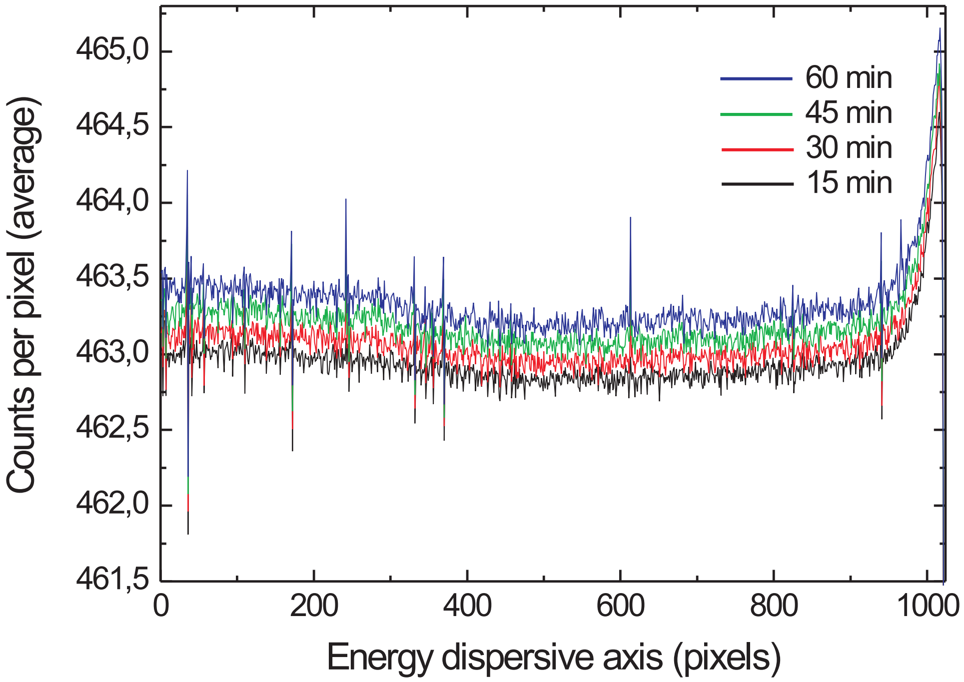

Figure 4.4: Average background per pixel projected on the energy dispersive axis at a camera temperature of −110°C, for different exposure times.

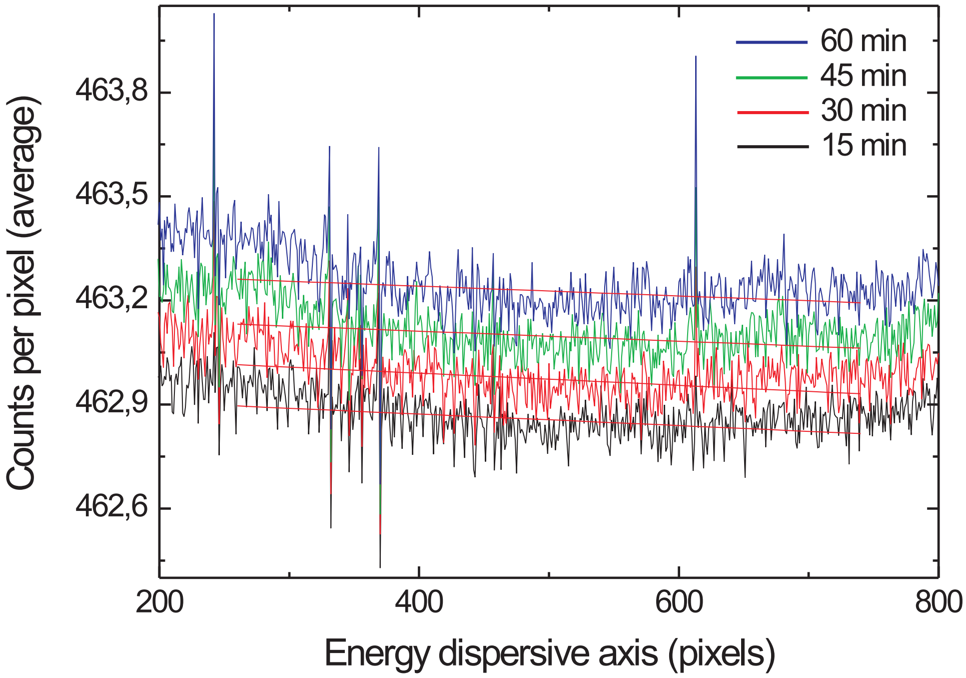

Figure 4.5: The same as Fig. 4.4 showing the important region between pixel rows 300 − 700 more closely, with linear fits. The slopes of the fits are listed in Tab. 4.2.

Apart from slightly higher noise levels at higher temperature, no significant temperature dependence of the background characteristics was found in the analysis of the background data files taken at −111°C and −106°C. Hence, the camera was operated at the specified temperature of −110°C. In exposures to x-radiation from the EBIT, apart from the line spectrum emitted by the ions also a continuous spectrum emitted in bremsstrahlung-processes is detected by the x-ray spectrometer. Over the small spectral bandwidth of about 50 eV covered by the spectrometer (at one crystal orientation), this background can be considered constant. Thus, it does not lead to asymmetries in the x-ray lines but adds a small amount of additional noise to the x-ray spectra.

Finally, exposures where the x-ray line appears around pixel 400 show a pixel row defect at row 397, as displayed in Fig. 4.6. To prevent this defect from influencing the data analysis, the integrated value of row 397 is replaced by the mean value of rows 396 and 398 before the fitting of the x-ray lines. For comparison, a Gaussian fit was made to both the original spectrum shown in Fig. 4.6 and a spectrum where the value of pixel 397 was replaced as described. In the uncorrected spectrum, the fit result for the Lyman-α_1 peak centroid was position 408.4(4), in the corrected spectrum the peak centroid was found to be at position 406.0(4), corresponding to a discrepancy of about 140 meV, or 40 ppm of the transition energy.

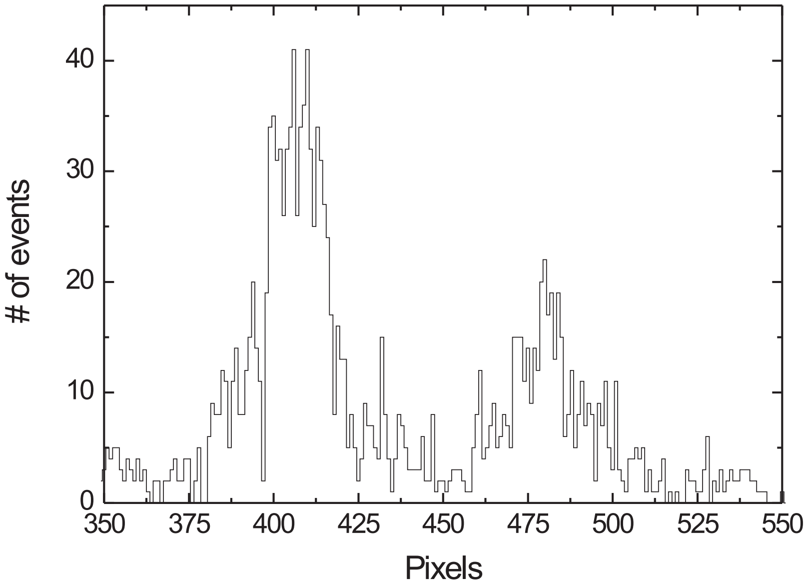

Figure 4.6: A Lyman-α spectrum showing the pixel row defect in row 397. This defect is visible in all spectra where an x-ray line is located above row 397. In the data analysis, the interpolated value of row 396 and 397 has been used instead of the original value.

4.2 X-ray line peak position determination

The line profile of the x-ray lines obtained with the spectrometer is determined by a Voigt function which is a convolution of the natural Lorentz profile with a Gauss profile. The convolution with the Gaussian represents line broadening effects arising from the ion temperature (Doppler broadening), the non-zero ion cloud size (source broadening) and imperfections of the spectrometer (crystal mosaicity etc.) which are generally subsumed as the “apparatus function”. The Voigt function is defined as

$$V(x) = (G * L)(x) = \int_{+\infty}^{-\infty} G(x')L(x-x')dx' \ , \tag{4.1}$$

with $L(x)$ and $G(x)$ the Lorentz- and Gauss-profile, respectively. There is no analytical solution for the convolution integral in Eq. (4.1) and, thus, the Voigt profile is commonly approximated by a simple weighted sum of the Lorentz and Gauss profiles called a pseudo-Voigt profile $V_{psd}(x)$:

$$V_{psd}(x) = (1-\eta)G(x) + \eta L(x) \ ; \ 0 \leq \eta \leq 1 \ . \tag{4.2}$$

The full width at half maximum (FWHM) Γ and the weighting parameter η of this curve can be computed from the FWHMs of the Gaussian (Γ_G) and the Lorentzian (Γ_L) components [TCH87]:

$$\begin{aligned} \Gamma &= (\Gamma_G^5 + 2.69296\,\Gamma_G^4\Gamma_L + 2.42843\,\Gamma_G^3\Gamma_L^2 \\ &\quad +4.47163\,\Gamma_G^2\Gamma_L^3 + 0.07842\,\Gamma_G\Gamma_L^4 + \Gamma_L^5)^{1/5} && (4.3) \\ \eta &= 1.36603(\Gamma_L/\Gamma) - 0.47719(\Gamma_L/\Gamma)^2 + 0.11116(\Gamma_L/\Gamma)^3 \ . && (4.4) \end{aligned}$$

Figure 4.7 shows a typical spectrum of the $1s2p\,^1P_1 \rightarrow 1s^2\,^1S_0$ transition in helium-like argon together with a Gauss and a Voigt fit to the line. This electric dipole transition is the one with the highest transition probability of all lines that were studied in this work (see chapter 4.5). Hence, the Lorentzian contribution to the overall line profile is expected to appear strongest in the shape of this line. With the transition probability of $A_{ki} = 1.07 \cdot 10^{14}\,\mathrm{s}^{-1}$ [BKS97], the relation $\Delta E \geq hA_{ki} \approx 0.44\,\mathrm{eV}$ and the dispersion of the instrument (known *e.g.* from the splitting of the Lyman-α lines in spectra like Fig. 4.6, in this work always $1\,\mathrm{eV} \approx 17\,\mathrm{pixels}$) one obtains an expected Lorentzian contribution to the total line width of about 7.5 pixels.

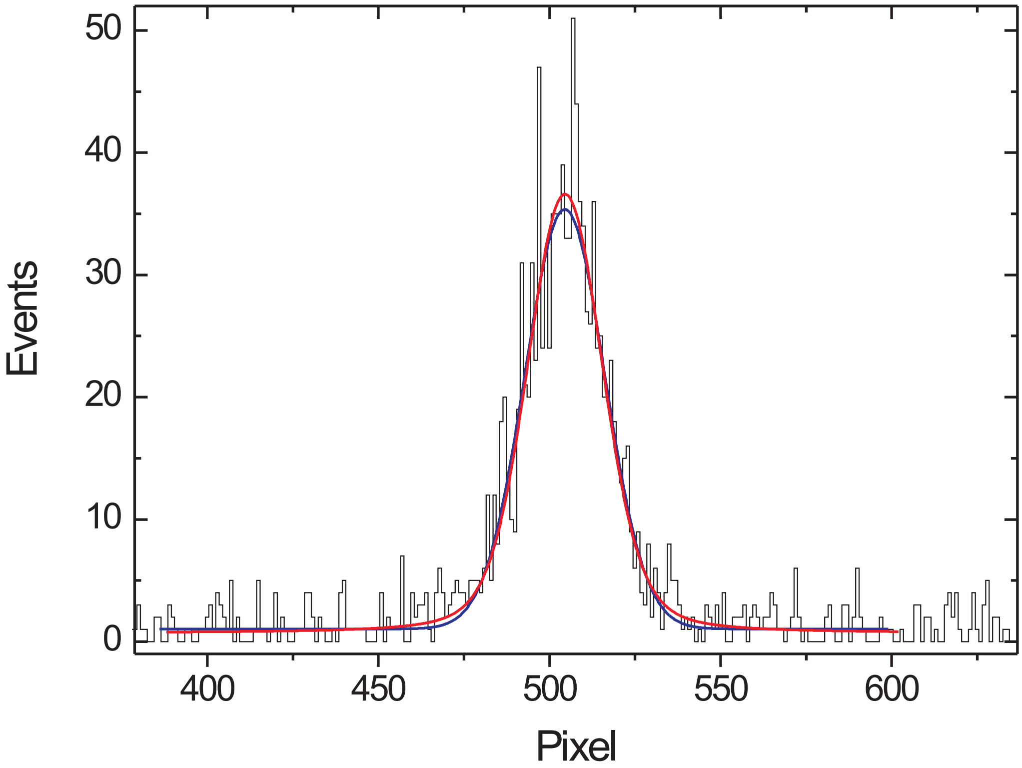

Figure 4.7: A spectrum of the $1s2p\,{}^1P_1 \rightarrow 1s^2\,{}^1S_0$ transition in Ar^{16+}. The blue curve shows a Gauss fit, the red curve a Voigt fit. For the fit of the Voigt profile its exact integral representation rather than the approximate pseudo-Voigt function was used.

Table 4.3: Fit results of the Gauss and Voigt fits in Fig. 4.7. All parameters are given in units of pixels. Statistical weighting was used in both fits.

Profile	Offset	Intensity	Peak center	Gauss width	Lorentz width	χ^2
Gauss	1.04(10)	1004(32)	504.47(39)	23.34(66)	–	0.95
Voigt	0.71(15)	1099(47)	504.52(40)	22.5(2.1)	6.3(2.2)	0.92

The results obtained from the two fits are displayed in Table 4.3. The Lorentz width obtained from the Voigt fit is in good agreement with the calculated one. Still, the line shape is clearly dominated by the Gaussian contribution to the Voigt profile. The two profiles fit equally well to the experimental data, the peak positions determined by the two fits agree well one with another, and the errors in the determination of the line centroid are almost equal (also if the Lorentz width is fixed to 7.5 pixels in the fit). This is not surprising, since the Voigt profile is symmetric like its Gaussian and Lorentzian components. Consequently, the peak position of a Voigt curve is well reproduced by a Gaussian fit, especially if the Gaussian contribution to the line profile is dominant. Hence, Gaussian fits are sufficiently accurate to obtain the x-ray line peak positions.

Since the x-ray detection represents a counting experiment, a statistical errorbar of the size $\sqrt{N_i}$ is assigned to each channel, where N_i is the number of events in the channel i. As seen from Figs. 4.6 and 4.7, it is possible that a channel contains zero events. This is problematic as the result is a zero-size error bar and, thus, the offset of the Gaussian fit is automatically set to zero (which is obviously non-physical) by the standard weighting procedure used in many cases. The appropriate way to assign an error bar to a zero count event can be deduced correctly only from Bayesian statistics [Har03,Har]. However, since the line profile is symmetric and the background constant, the absolute value of the background level found by a fitting procedure does not affect the x-ray line position. It is, hence, allowed to assign an error bar of 1 event to all zero event data points before the Gaussian fit [Har].

In the automatised fitting procedure used in these measurements and described in chapter 4.4 a complete x-ray spectrum is analysed at once. Since the background is constant, the fitted positions are not affected by analysing the whole spectrum rather than only the region around the x-ray lines. Still, in the determination of the reduced χ^2,

$$\chi^2 = \frac{1}{n-1} \sum_{i}^{n} \left(\frac{f(N_i) - N_i}{\Delta N_i} \right)^2 , \tag{4.5}$$

where $f(N_i)$ is the value of the fit function at position i, the background is overrepresented if the complete spectrum is fitted. This means that the χ^2 obtained from the automatised fit differs from a fit where only a small region of a few standard deviations around the line centroid is taken into account. This point was studied in some more detail by doing manual Gaussian fits to 15 randomly selected x-ray spectra obtained in the measurement that will be described in chapter 4.5. The reduced χ^2 from these fits is always close to 1 (Tab. 4.4), whereas the χ^2 obtained in the automatised fits of the same spectra scatters by about ± 0.1 around 1. Commonly the errors of a fit are scaled with the reduced χ^2. However, as the χ^2 of the manual fits is close to 1 but the automatic fit is done over the complete spectrum, it was chosen not to scale the errors obtained from the automatised fits with their respective χ^2 but to rather use the standard value of 1 for all of them.

Table 4.4: Reduced χ^2 from manual Gaussian fits to randomly selected x-ray spectra where only a small region of $\approx 5\sigma$ around the line centroid was fitted.

Transition	1	2	3	4	5
Ar^{17+} Lyman-α	0.92	1.01	1.02	0.98	1.00
Ar^{16+} $1s2p\ {}^1P_1$	0.83	0.80	1.02	0.98	0.95
Ar^{17+} $1s2p\ {}^3S_1$	0.88	1.14	0.93	0.94	0.92

4.3 Visible light fiducial analysis

In contrast to the x-ray line shape, the profile of the visible light fiducials cannot be derived from elementary processes because it is the result of an optical imaging procedure and, thus, the line shape cannot be directly described by a predetermined analytical peak function. However, it is not important whether the shape of the lines is exactly reproduced by a fit of any analytical function, as long as this procedure is reproducible and a stable position reference is obtained. Hence, the function used to find a position reference from the visible light lines is somewhat arbitrary, as long as the deviation between the real line shape and the fit function's profile is always the same.

Projecting the visible light images to the axis of the CCD which is energy dispersive for the x-ray lines results in a spectrum of two peaks which have, by chance, a remarkable resemblance to Lorentz-curves. A fit of Lorentzian profiles to exemplary visible light peaks and the residuum of this fit, *i.e.* the deviation of the fiducial profile from the Lorentz curves, is shown in Fig. 4.8.

Clearly, the line shape is only approximated by a Lorentzian profile. To check the reliability of the a/b method, it is necessary to show that the peak positions can be reproducibly obtained from such fits at different orientations of crystal and camera. To test this, a number of fiducial images have been acquired, keeping the camera position fixed and changing the crystal angle in between the exposures by about 0.013°. In this way, the fiducials were forced to move over the camera. Analogously, when the crystal angle was kept fixed and the camera was moved the fiducials stayed fixed in space and, depending on the respective camera position, appeared at different positions in the images. The result of these measurements is displayed in Fig. 4.9. A second-order polynomial was fitted to the data to approximate the sinusoidal dependency of the peak positions on the angle.

Some larger fluctuations affecting both fiducials alike can be seen in the polynomial fit residuals. These changes can be explained by temperature changes and the fact

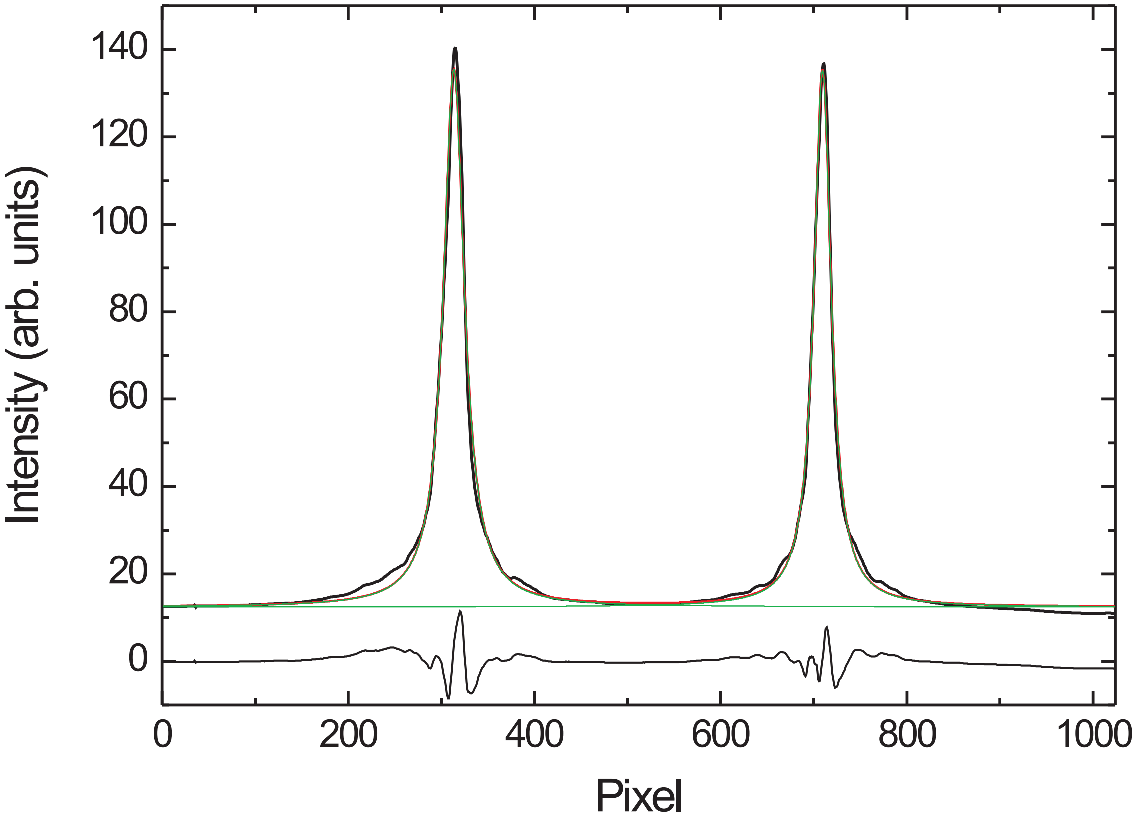

Figure 4.8: Projections of the light fiducials on the energy dispersive axis and Lorentzian fits. The graph at the bottom shows the fit residuals.

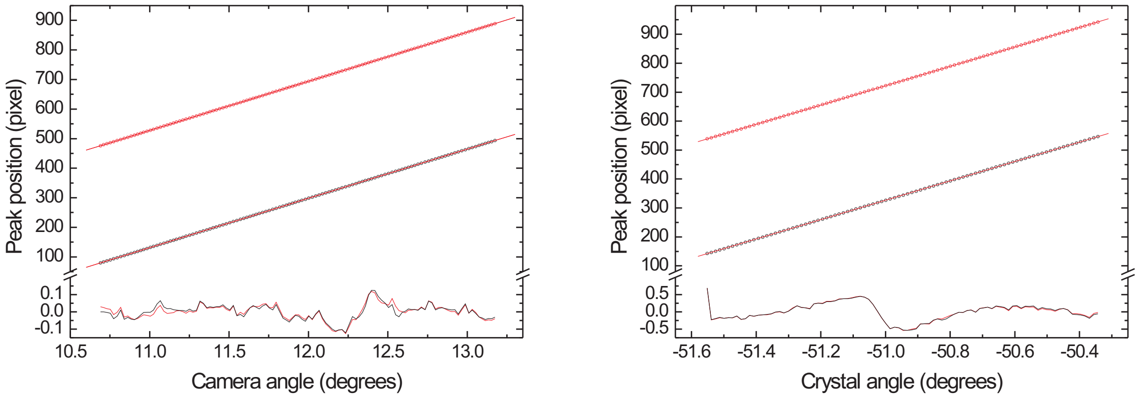

Figure 4.9: Light fiducial positions in dependence of the camera position (right) and the crystal orientation (left). The lines drawn through the datapoints represent parabolic fits, the graph at the bottom are the fit residuals. The residuals correspond to an angle of $< 6 \cdot 10^{-4\,\circ}$ (left) and $< 1.4 \cdot 10^{-3\,\circ}$ (right), respectively.

that people working in the laboratory during the measurement caused vibrations that can easily lead to shifts of some micrometers. In particular, the large deviation in the very first datapoint in the right graph of Fig. 4.9 is most likely due to the author of this work walking away from the instrument after starting that measurement sequence.

The reproducibility of the fiducial position determination can be obtained from the small-scale variations in the residuals which amount to less than 0.1 pixel. These fluctuations also include the uncertainties generated from the positioning of crystal or camera, respectively. In comparison, the uncertainty in the x-ray peak position determination from a fit is of the order of 0.5 pixels (see table 4.3). Hence, the uncertainty in the the determination of the fiducial positions is a negligible contribution to the error of the a/b distance ratio.

A qualitative argument can be obtained by comparing the residuals of Lorentzian fits to several different fiducial images one with another. This is more fruitful than directly comparing the fiducial shape, since additionally to the differences in the fiducials also the reproducibility of the fitting procedure is seen there. Furthermore, their substructure appears more prominently and so do the small deviations between their shapes.

To be able to compare the residuals one has to realise that at different crystal and camera angles the fiducials appear at slightly different positions on the camera. This is due to the fact that the camera cannot be positioned with the required precision according to the chosen crystal angle. Also, as the timing of switching the LED light source on and off is controlled with only a few hundred milliseconds precision, it is not surprising that the peak height changes between the single exposures. Thus, the fit residuals have to be shifted and scaled to overlap. This procedure was carried out with the residuals of Lorentzian fits to 73 different fiducial spectra obtained at different crystal and camera angles. The angles were chosen like in a typical x-ray measurement: two central crystal angles defined by the transition energies of the x-ray lines under study. The crystal (and the camera accordingly) was alternately moved to angles close to these values, with small shifts which in an x-ray measurement would cause the x-ray reflection position on the crystal to move. All 73 normalised and shifted residuals are shown in Fig. 4.10. It is seen from the figure that the substructure of the fiducials, *i.e.* the deviation of their shape from the Lorentz profile, is very reproducible. This means approximating the fiducial shape with a Lorentzian fit results in always the same systematic shift in the peak position determination, as was also indicated by the crystal and camera movement measurements described before. In other words, the a/b distance ratios are influenced by this choice of the fit function only negligibly. Judging from the

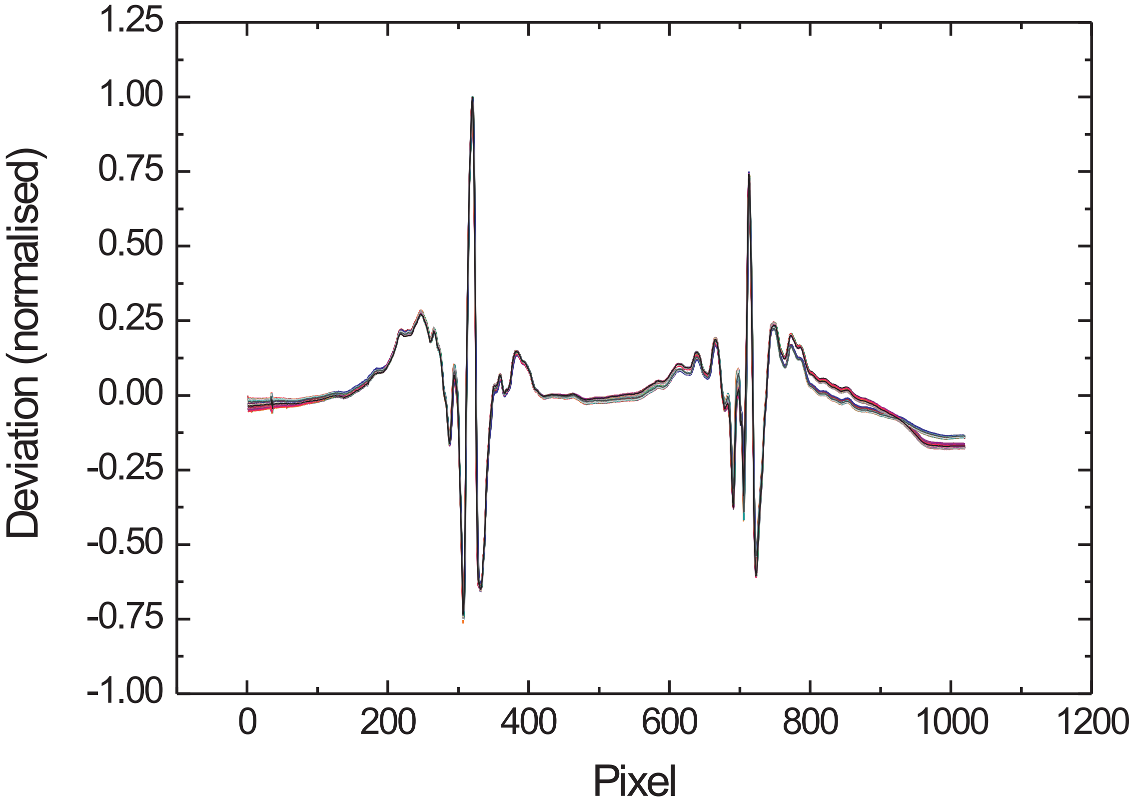

Figure 4.10: Residuals of Lorentzian fits to 73 different visible light fiducial projections, normalised and shifted to the point of largest deviation (the curves are not stretched horizontally).

results obtained with both the quantitative and the qualitative test methods described above, it was concluded that the centroid positions of Lorentzian fits to the fiducials could be used very reliably as the references needed for the a/b-method in high-precision measurements.

4.4 Obtaining a/b distance ratios from the data files

In total, four values are needed for the generation of a single datapoint in the a/b distance ratio plot: the positions of the two fiducials and that of the x-ray line as well as the crystal angle measured during the exposure.

As discussed before the fiducials for the x-ray lines are obtained by Lorentzian fits to projections of the 5 second exposures of the visible light beams taken before and after the x-ray exposure. However, from the continuous crystal angle readings taken

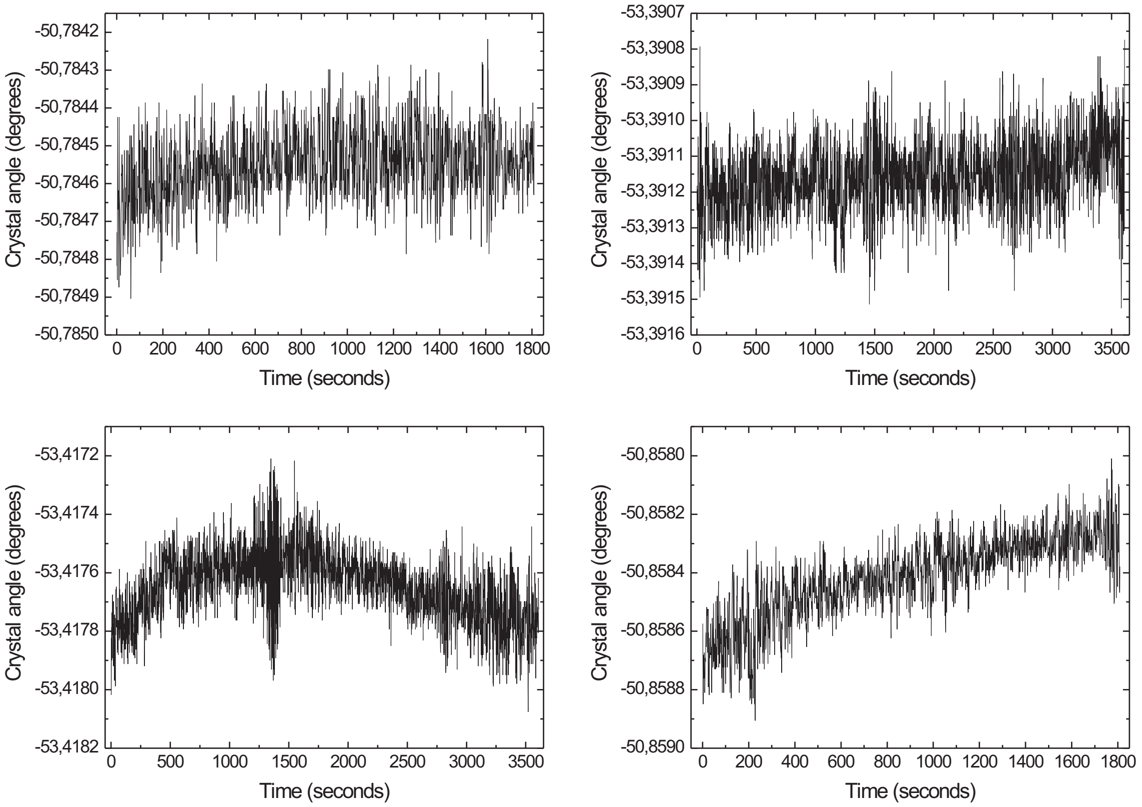

Figure 4.11: Crystal angle movement over time. Top: typical progressions. Bottom: unusual progressions. In the case of the bottom left progression the fiducial interpolation routine actually has to extrapolate from the start and end angles to the mean crystal angle (see text). The rapid oscillations are due to vibrations of the instrument.

during the x-ray exposures it was found that the crystal angle is not constant on the time scale of $15 - 60$ minutes but changes by amounts of the order of $(10^{-4})^\circ$ (Fig. 4.11). These small changes are believed to originate mainly from torsion relaxation in the crystal holder after the positioning process. As seen from Fig. 4.9, a change in the crystal angle by $(10^{-4})^\circ$ results in a (in very good approximation linear) movement of the visible light fiducial positions by approximately 0.05 pixels[1]. Such changes are indeed found in the comparison of the fiducials before and after the x-ray exposures. Hence, interpolated fiducial positions according to the mean crystal angle measured during the x-ray exposure are used as the references needed.

For every data point, three images are acquired (2 × light fiducials, 1 × x-ray). Hence, a measurement requires the analysis of usually much more than 100 images. All the peak fitting procedures were automatised using a Levenberg-Marquardt algo-

---

[1] The value of 0.5 pixels for this shift found in [BBT$^+$05] is wrong.

rithm implemented in a LabView programme. Only the final fit of the a/b ratio data obtained from that programme was performed using the commercial data analysis software Origin 7. The validity of the fit results obtained by the LabView programme were checked by comparing the a/b distance ratio of a random x-ray exposure so obtained with results yielded by using Origin 7. The LabView programme gave a value for the distance ratio of 0.5733(96), the result of the analysis with Origin 7 was 0.5734 (no error was calculated here, since the correctness of the error calculation in the LabView programme had been checked before). However, the best proof that the fitting procedure written in this work delivers correct results was given by using a slightly modified version of the programme to analyse spectral data in the visible range by the author of [Sor05]. The automated analysis developed in this work gave within a fraction of the error bar identical results as a previous elaborate data analysis procedure using Origin 7.

To summarise, the procedure to obtain the a/b distance ratio plot from the raw data is sketched in the following. First, some exemplary x-ray data files are studied to determine the optimal background and cosmic particle discrimination levels. Then, spectra from all x-ray and visible light images are projected (no regions or thresholds are used when creating projections of fiducial images). The fully automatised procedure iteratively reads all data files recorded at a certain crystal angle, *i.e.* one x-ray spectrum, the two images of the fiducials (before and after the x-ray exposure) and the data files of the crystal angle measurement. Then, Lorentz-profiles are fitted to the light fiducials to obtain their positions. X-ray line positions are obtained by fitting as many Gauss-curves as there are clearly discernible lines in the x-ray spectrum (automatic search of the highest peak, the guess values for the fit of other peaks are entered manually before starting the analysis programme). From the fiducial positions $P(F)_{i,t}$, where the indices stand for one fiducial ("left or right", $i = \{1, 2\}$) in one single exposure (before or after the x-ray exposure, $t = \{1, 2\}$) and the corresponding mean crystal angles $\bar{\xi}(F)_t$ and $\bar{\xi}(X)$ measured during the fiducial and x-ray exposures, respectively, the interpolated reference positions $P(R)_i$ are calculated as

$$P(R)_i = P(F)_{i,1} + \left(\bar{\xi}(X) - \bar{\xi}(F)_1\right) \frac{P(F)_{i,2} - P(F)_{i,1}}{\bar{\xi}(F)_2 - \bar{\xi}(F)_1} \ . \tag{4.6}$$

Finally, the distance ratio of an x-ray line at position $P(X)$ is determined as

$$\left|\frac{a}{b}\right| = \left|\frac{P(X) - P(R)_1}{P(X) - P(R)_2}\right| \ . \tag{4.7}$$

Since the errors in the determination of the peak positions and the angle measurement are independent one from another, the error $\Delta|a/b|$ in dependence of the single parameters (in the following called x_n with $n = \{1, 2, \dots\}$) can be estimated using the error propagation law

$$\Delta|a/b|(x_1, x_2, ...x_n) = \left[\sum_n \left(\frac{\partial|a/b|}{\partial x_n}\Delta x_n\right)^2\right]^{\frac{1}{2}} . \tag{4.8}$$

As expected, the total error of a typical a/b distance ratio is dominated by the uncertainty in the determination of the x-ray peak position. If the mean crystal angle during the x-ray exposure is higher or lower than both the angle at the beginning as well as the angle at the end of the x-ray exposure (see Fig. 4.11, bottom left image) the fiducial interpolation routine in Eq. (4.6) actually has to do an extrapolation. In these very rare cases the total error $\Delta a/b$ would be dominated by the uncertainty arising from this extrapolation, and the corresponding data points are therefore ignored in the further data analysis.

4.5 Experimental results

The first experiment employing the a/b-method is the measurement of the energies of the transitions $(1s2p)\,^1P_1 \rightarrow (1s^2)\,^1S_0$ and $(1s2s)\,^3S_1 \rightarrow (1s^2)\,^1S_0$ in helium-like argon (Ar^{16+}), which are traditionally designated as the "w" and "z" lines following the Gabriel notation [Gab72], as well as the Lyman-α_1 transition in hydrogen-like chlorine (Cl^{16+}). All three lines were measured with respect to the Lyman-α_1 transition energy in hydrogen-like argon (Ar^{17+}). Figure 4.12 shows the Grotrian diagram of $n = 2 \rightarrow n = 1$ transitions in helium-like as well as close-lying transitions in lithium-like ions, along with their Gabriel notation names. The respective transition energies are listed in Table 4.5 and Table 4.6. Using a Si-111 crystal, the Bragg angles of the two Lyman-α, the w and the z transitions lie between 36.5° and 42.0°, and are well within the positioning range of crystal and camera.

From the experimental point of view this measurement is the hardest conceivable test of the new method, since the Ar^{17+} Lyman-α_1 and the Ar^{16+} w lines are the most accurately measured ones for hydrogen-like and helium-like ions, respectively [BDFL85, DBF84]. The theoretical prediction and the measured value for the Ar^{17+} Lyman-α_1 transition energy are in excellent agreement (within 5 ppm), making this transition a perfect reference standard for high-precision spectroscopy in the 3 keV range with an EBIT. The accuracy of the best experimental value for the Cl^{16+} Lyman-α_1 transition energy is somewhat lower, namely 33 ppm [KKRS84]. For this reason, the calculated value of the Lyman-α_1 transition energy in hydrogen-like chlorine can be considered to be more accurate than the experimental value. It is, hence, worthwhile to measure this transition in order to test the new experimental method.

Concerning the physical importance of this measurement, it is interesting to note that most calculations, including some recent ones, for the w-transition disagree with the value measured by Deslattes *et al.* [DBF84]. Moreover, the simultaneous measurement of both the w and z transition energies is interesting, since different effects are important for the calculation of the excited states involved. For the $1s2p\,(^1P_1)$ initial state of the w-transition, configuration mixing is very important, and the two-electron QED contribution is estimated to amount to almost 30 ppm of the total transition energy [CPH$^+$00]. On the other hand, the metastable $1s2s\,(^3S_1)$ initial state of the z-transition is less affected by mixing but more sensitive to relativistic effects.

Table 4.5: Calculated energies of the $n = 2 \rightarrow n = 1$ transitions in helium-like argon [ASY$^+$05].

Transition	Designation	Wavelength (mÅ)	Energy (eV)
$1s2p\ ^1P_1 \rightarrow 1s^2\ ^1S_0$	w	3949.067 mÅ	3139.582 eV
$1s2p\ ^3P_2 \rightarrow 1s^2\ ^1S_0$	x	3965.857 mÅ	3126.290 eV
$1s2p\ ^3P_1 \rightarrow 1s^2\ ^1S_0$	y	3969.356 mÅ	3123.534 eV
$1s2s\ ^3S_1 \rightarrow 1s^2\ ^1S_0$	z	3994.146 mÅ	3104.148 eV

Table 4.6: Experimental wavelengths and energies for transitions in lithium-like argon within the spectral range of the transitions listed in Tab. 4.5, from [TBPS01].

Transition	Designation	Wavelength (mÅ)	Energy (eV)
$1s2p(^1P)2s\ ^2P_{3/2} \rightarrow 1s^2\ ^1S_0$	s	–	–
$1s2p(^1P)2s\ ^2P_{1/2} \rightarrow 1s^2\ ^1S_0$	t	–	–
↪ Blend	s, t	3968.91(20) mÅ	3123.89(16) eV
$1s2p(^3P)2s\ ^2P_{3/2} \rightarrow 1s^2\ ^1S_0$	q	3981.34(10) mÅ	3114.13(08) eV
$1s2p(^3P)2s\ ^2P_{1/2} \rightarrow 1s^2\ ^1S_0$	r	3983.55(10) mÅ	3112.40(08) eV
$1s2p(^3P)2s\ ^4P_{3/2} \rightarrow 1s^2\ ^1S_0$	u	–	–
$1s2p(^3P)2s\ ^4P_{1/2} \rightarrow 1s^2\ ^1S_0$	v	–	–
↪ Blend	u, v	4010.12(20) mÅ	3091.78(15) eV

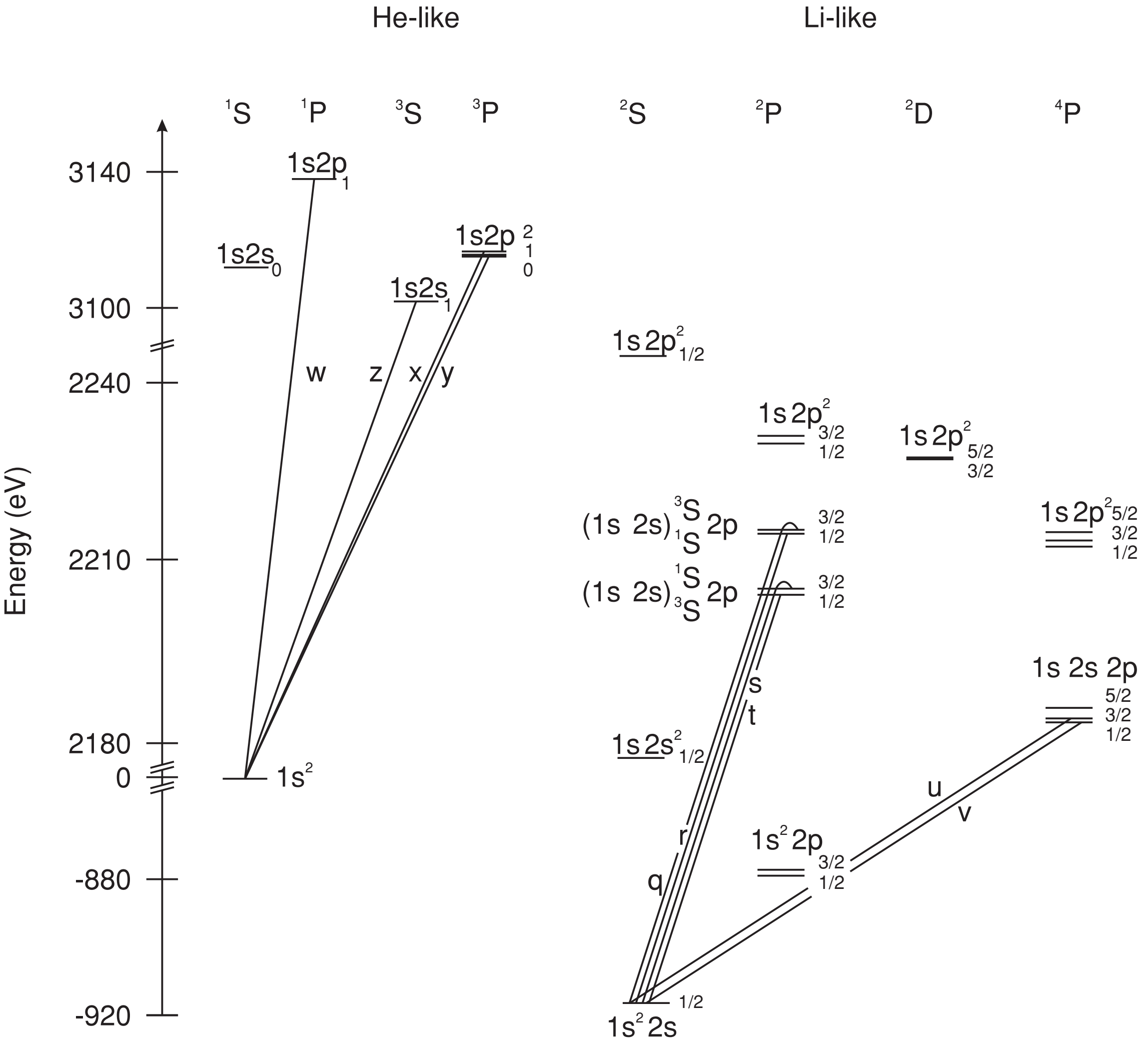

Figure 4.12: Left: Radiative decay scheme of helium-like argon. All named (Gabriel notation [Gab72]) transitions are $E1$-transitions except for z ($M1$). Right: Radiative decay scheme of those transitions in lithium-like ions that lie close to lines from helium-like ions. All indicated transitions stem from excited states that can be created through direct electron impact excitation (no dielectronic satellites).

4.5.1 Experimental setup and data acquisition

From the data gained at the first attempt to perform this measurement, it became apparent that the Lyman-α_1 and Lyman-α_2 transitions were not completely resolved if the x-ray spectrometer is attached directly at the EBIT viewport. In this configuration, the distance between the crystal and the trap volume is about 65 cm. Since the statistical significance reached in this first measurement was much higher than needed, it was concluded that a higher resolution at the expense of x-ray flux losses by setting up the spectrometer at a larger distance from the trap was preferrable. Hence, in all following beamtimes a larger distance between crystal and trap was chosen, yielding a reasonable separation of the two Lyman-α peaks in the spectra. That first measurement failed due to shape imperfections in the angular scale ring used for the crystal angle measurement. In the process of data analysis no satisfactory corrections were found to account for these imperfections. This problem was solved by replacing the measurement device for the determination of the crystal angle with an absolute angle encoder (see chapter 3.1).

The final results presented in this work originate from a second beamtime with the new angular measurement device. The spectrometer was set up at the end of an evacuated beamline, with the total distance between the crystal and the EBIT ions of 1586(2) mm (1815(2) mm distance between ions and CCD detector). With an electron beam energy set to approximately 13.5 keV, a beam current of 330 mA and axial trapping voltages of 90 V ($\times q$), reasonable count rates were obtained for all investigated lines (for details about ionisation cross-sections, ionisation and transition rates as well as EBIT beam parameter optimisation see [Gon05]). Alternately Lyman-α, w and z spectra of argon were obtained in the measurement sequence. The Lyman-α_1 transition energy of chlorine was measured later and will be discussed in chapter 4.5.5. The exposure times for each Lyman-α spectrum (both argon and chlorine) was 1 hour, for the w spectra 30 min and for z-spectra 45 min. Before and after each x-ray exposure, light fiducial images were acquired in 5 second exposures, respectively. During exposures and readout of the CCD camera, a crystal angle reading was taken every second (see Fig. 4.11). The room temperature was measured at the beginning of each x-ray and fiducial exposure. In total, 24 spectra of the Lyman-α transition (Fig. 4.13) and 23 spectra of the w (Fig. 4.14) and z (Fig. 4.15) transitions were obtained.

4.5.2 Details of the x-ray spectra

In the argon Lyman-α spectra (Fig. 4.13) the data analysis programme was set to fit a Gaussian profile to each of the peaks. In the w-spectra (Fig. 4.14) only one Gaussian was fitted to the w-peak. Due to the large separation from the w line, no effect on the w peak position found by the fit was expected by neglecting x and y. In the z-spectra, three Gaussians were fitted in total: one to the x, y blend, one to the q, r blend, and one to the z-line, respectively. None of the fitting parameters (*i.e.* offset, peak positions, amplitudes or widths) were constrained.

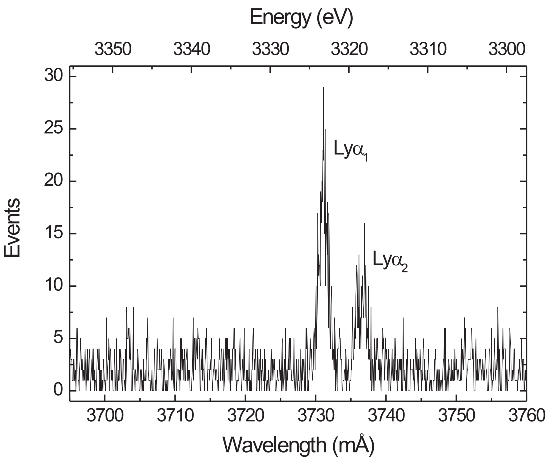

Figure 4.13: An exemplary Ar^{17+} Lyman-α spectrum (exposure time: 60 minutes).

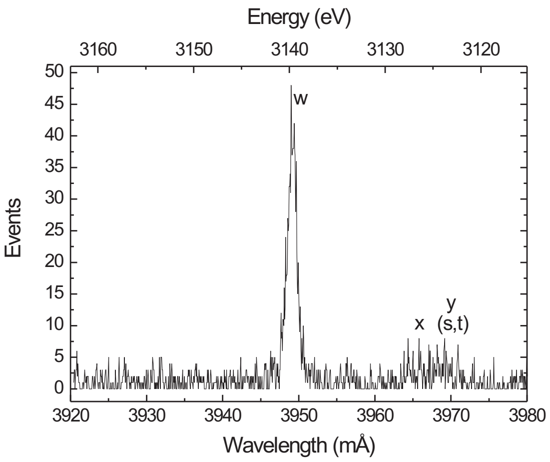

Figure 4.14: An exemplary Ar^{16+} w spectrum (exposure time: 30 minutes).

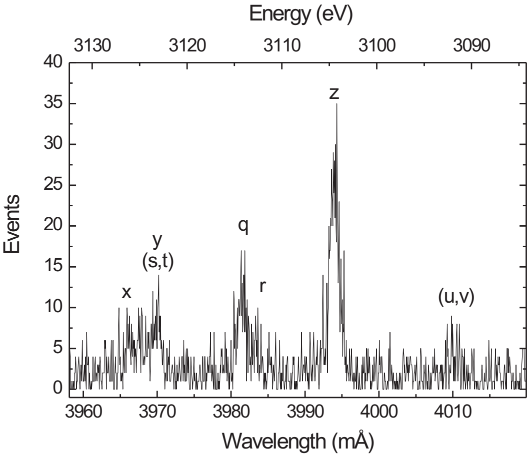

Figure 4.15: An exemplary Ar^{16+} z spectrum (exposure time: 45 minutes).

From the fit results the distance ratios a/b and their errors were determined as described in Eq. (4.7) and Eq. (4.8). However, before analysing the distance ratios, one has to sum the single x-ray spectra to check whether the assumption of the line symmetry was correct. Since an x-ray line appears at different positions in the different spectra due to the intentioned angle changes, all corresponding spectra have to be shifted to overlap before the summation. Again, this is done automatically by a LabView programme that reads all spectra of one x-ray line as well as the peak position fitted to it before. Since the x-ray peak position is usually not located at an integer pixel number, the shifting requires some interpolation. Figure 4.16 illustrates the algorithm which will be described in the following.

Each spectrum is shifted in two steps. In the first step, an empty second spectrum of 2048 elements width is generated. Each data point at position i in the original spectrum is inserted to the position $j = 1024 - x + i$ into the second spectrum, where x is the truncated value of the fitted pixel position. This first step brings the peak position close to the position 1024 in the second spectrum. The fractional shift by the remaining $0.y$ pixels is obtained by creating an interpolated copy of this second spectrum. In this third and final spectrum, the fth element is generated by filling

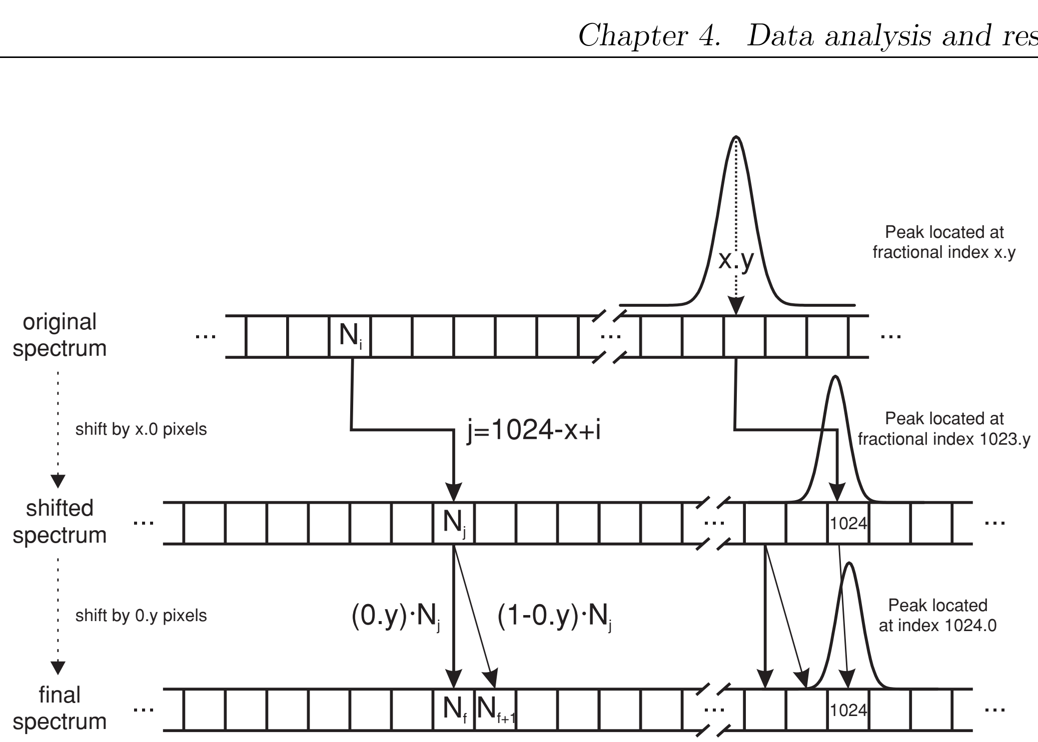

Figure 4.16: Schematic to illustrate the spectrum shift needed for summation of the single x-ray spectra. First the original spectrum is shifted by an integer number of pixels x so that the peak position of the x-ray line appears close to pixel 1024 in the shifted spectrum. Then, the remaining fractional shift is performed by interpolating this shifted spectrum. All spectra shifted this way are then added up to create the sum spectrum.

it with $N_f = yN_j + (1-y)N_{j-1}$ events from the second spectrum. In the final sum spectrum, the x-ray peak is located almost exactly at position 1024, as fits to the sum specta showed (see Table 4.7).

After performing this procedure with all spectra of one type, their sum is obtained. The sum spectra of the argon Lyman-α, w and z transitions are shown in Figs. 4.17, 4.18 and 4.19, respectively. Note that due to the shifting of the single, original spectra, the sum spectrum gently drops to zero at both ends. This is seen in Fig. 4.19. In particular, the peak generated by the x-transition layed outside of the spectral range in some of the z-transition spectra and is, hence, underrepresented in the sum spectrum.

The shifting of the spectra is not perfect and, thus, the lines in the sum spectrum are broader than lines in the single spectra. Most of this broadening is due to the uncertainty in the peak determination from the Gauss fits to each single x-ray spectrum. To quantify this broadening effect, 25 artificial spectra were created and summed with the algorithm. Each of these spectra contained one line at different positions, respectively. The lines were created from perfect Voigt profiles with a Gaussian width of $w_G = 20$ pixels and a Lorentzian width of $w_L = 10$ pixels, and

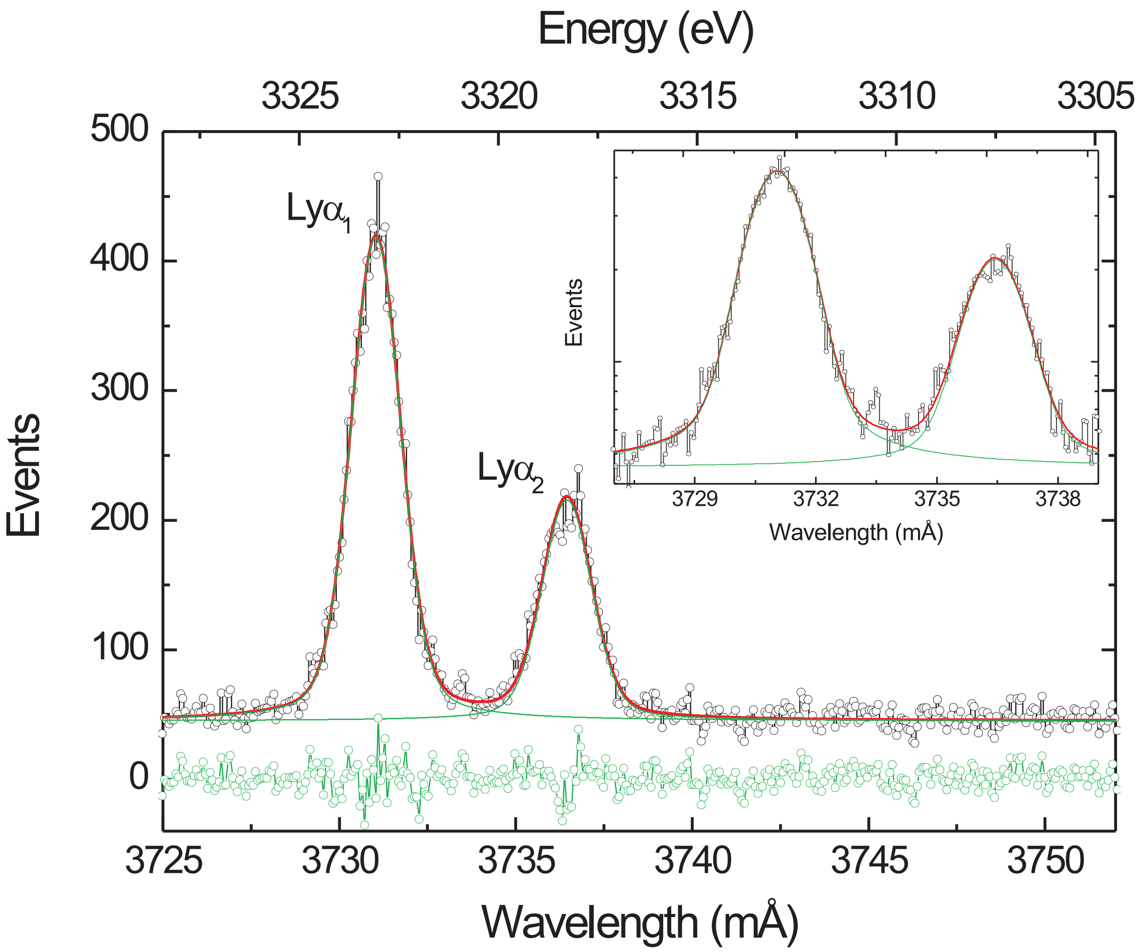

Figure 4.17: Sum spectrum of the Ar^{17+} Lyman-α transition spectra, Voigt fit and residuals. The insert shows the same spectrum with a logarithmic scale.

superimposed with noise proportional to the squareroot of the peak amplitude (chosen to be about 100 events) to simulate a measurement. A Voigt fit to the sum of these simulated spectra gave a Gaussian width of $w_{G,Sum} = 24.2(5)$ pixels and a Lorentzian width of $w_{L,Sum} = 10.2(5)$ pixels, showing that the Lorentzian width of the line is preserved when using the spectrum summation algorithm, while the Gaussian width is slightly increased.

The Lyman-α, w and z sum spectra were fitted using Voigt profiles, since it was assumed that the Lorentzian contribution to the line shape should appear more clearly in the sum spectra than in the single spectra due to the higher statistical significance. As expected, in the case of the Lyman-α_1 and the w transitions a Voigt profile fits the sum spectra perfectly (Fig. 4.17 and 4.18), whereas the peak height as well as line wings are underrepresented when using a Gaussian fit. On the

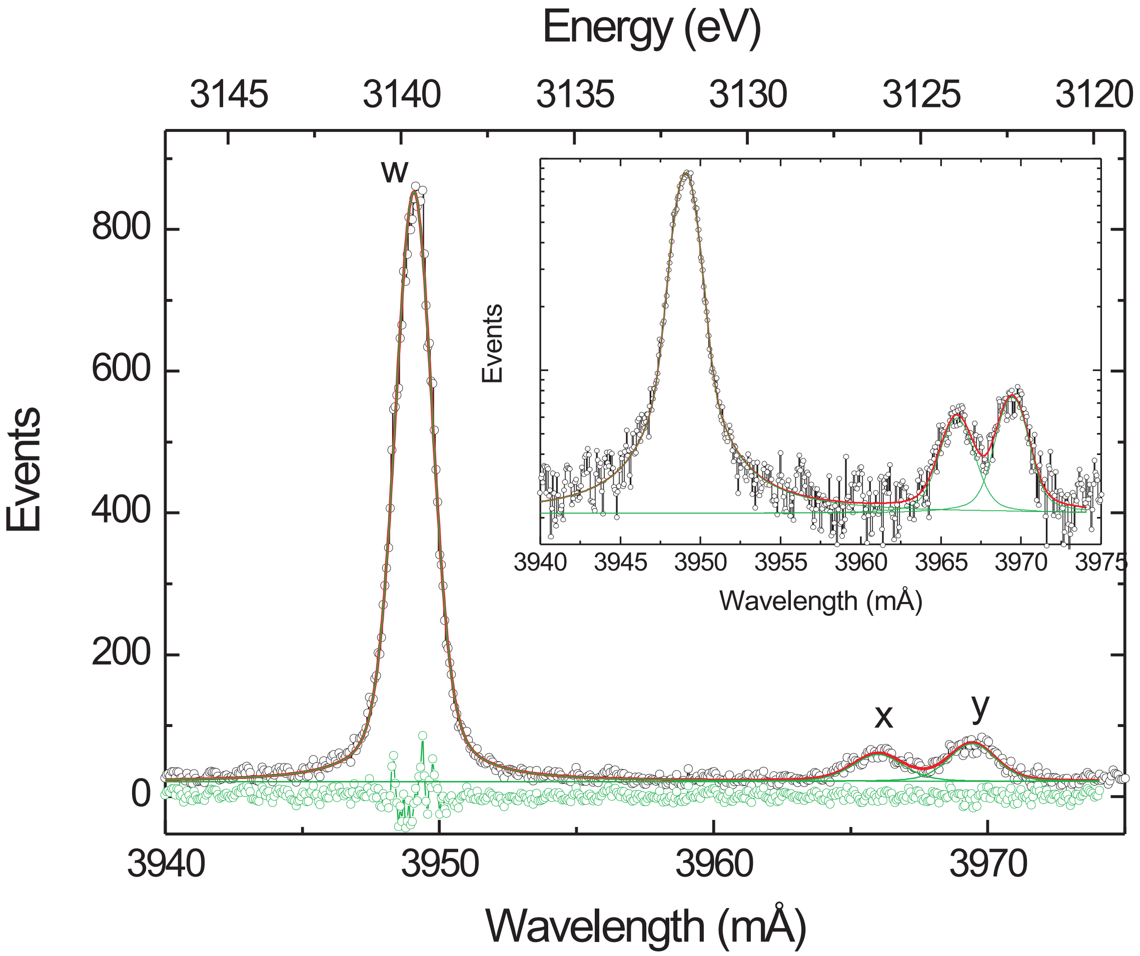

Figure 4.18: Sum spectrum of the Ar^{16+} w transition spectra, Voigt fit and residuals. The insert shows the same spectrum with a logarithmic scale.

other hand, the z transition originates from the decay of a metastable excited state with a transition probability of only $A_{ki} = 4.8 \cdot 10^6$ Hz [BKS97] which corresponds to a natural line width of $2 \cdot 10^{-8}$ eV. It was, hence, expected that the line of the z transition is of purely Gaussian shape. It comes as a surprise that also in this spectrum a Gaussian fit underrepresents the peak height and the line wings. As a test, a Voigt profile was fitted to the line and found to perfectly match the line shape. In fact, within the error bars the Lorentzian width obtained from this fit is the same as in the w sum spectrum. The results of the Gauss and Voigt fits performed on the Lyman-α_1 line, the w line and the z line in the sum spectra are shown in Table 4.7. It is yet unclear as to why the z transition is well represented by a Voigt shape in the sum spectrum, or why the apparatus function of the x-ray spectrometer would contain a Lorentzian contribution.

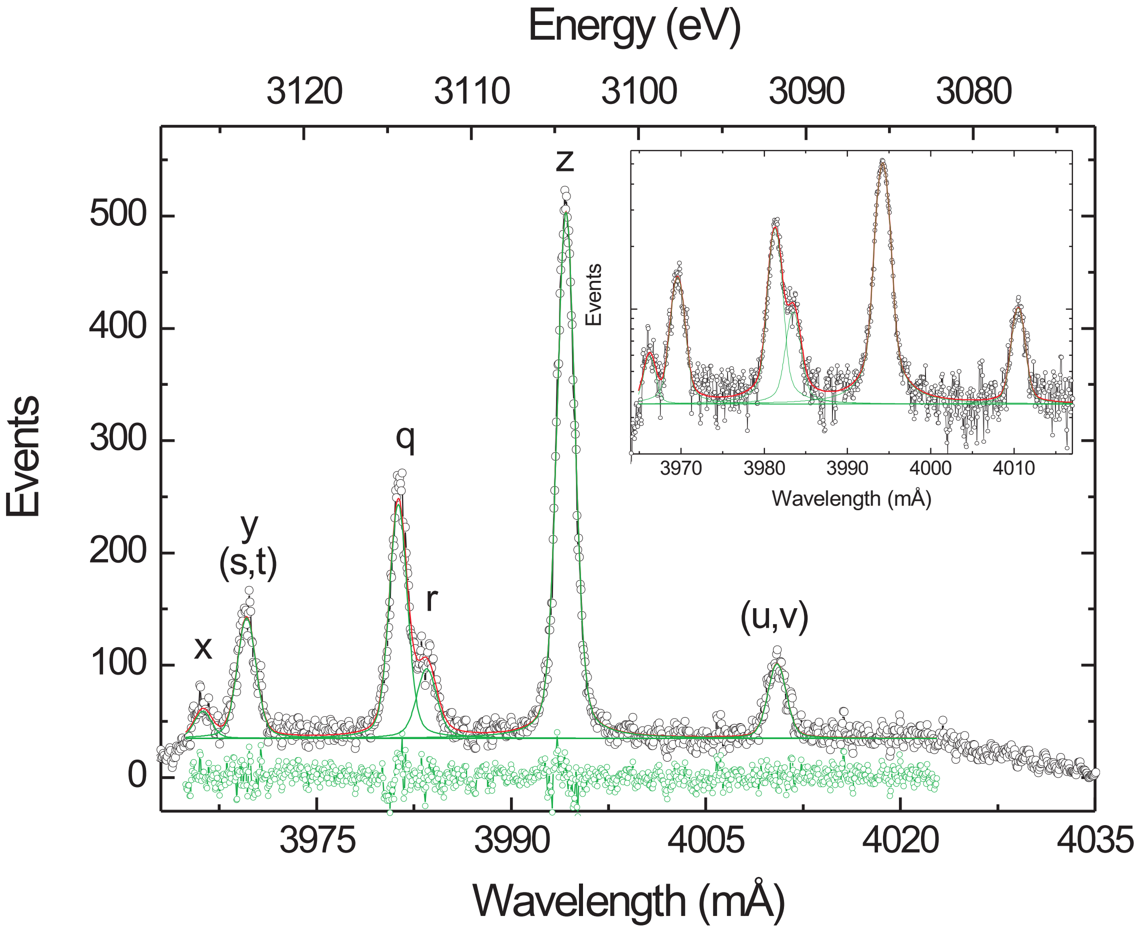

Figure 4.19: Sum spectrum of the Ar^{16+} z transition spectra, Voigt fit and residuals. The insert shows the same spectrum with a logarithmic scale. In contrast to the single spectra (Fig. 4.15), in the sum the lines q and r can be clearly resolved. The x line was not within the range of all single spectra and is, thus, underrepresented in their sum. The gentle falloff of the baseline on both ends is a consequence of the way the spectra are added up (see text for details).

While the sum spectra obviously cannot be used to perform a precise determination of the line shape, the line symmetry is at least sufficiently proven. As can be seen from the sum spectra, there is not the slightest indication at all for close-lying satellites originating from transitions with a spectator electron in multiply excited ions to either one of the lines of interest that could lead to a systematic error in the determination of the line centroids. For comparison, Fig. 4.20 shows a spectrum taken from [BRF02], where such satellites were excited by dielectronic recombination processes.

Table 4.7: Comparison of Gauss and Voigt fit to the sum spectra. The precise integral form of the Voigt profile was used in the fit.

	Lyman-α_1		w		z	
Parameter	Gauss	Voigt	Gauss	Voigt	Gauss	Voigt
Offset	49.92(61)	47.38(69)	28.71(54)	22.54(47)	39.21(56)	33.94(59)
Peak position	1023.98(15)	1024.02(15)	1023.94(14)	1023.98(10)	1023.97(16)	1023.92(13)
Amplitude	10380(133)	11473(210)	23873(269)	27009(233)	13364(168)	15398(202)
Gauss width	22.78(28)	21.20(95)	24.54(24)	20.22(51)	23.63(28)	19.30(76)
Lorentz width	–	7.25(1.05)	–	9.93(46)	–	10.38(73)
χ^2	1.19	1.00	2.73	1.17	1.69	1.00

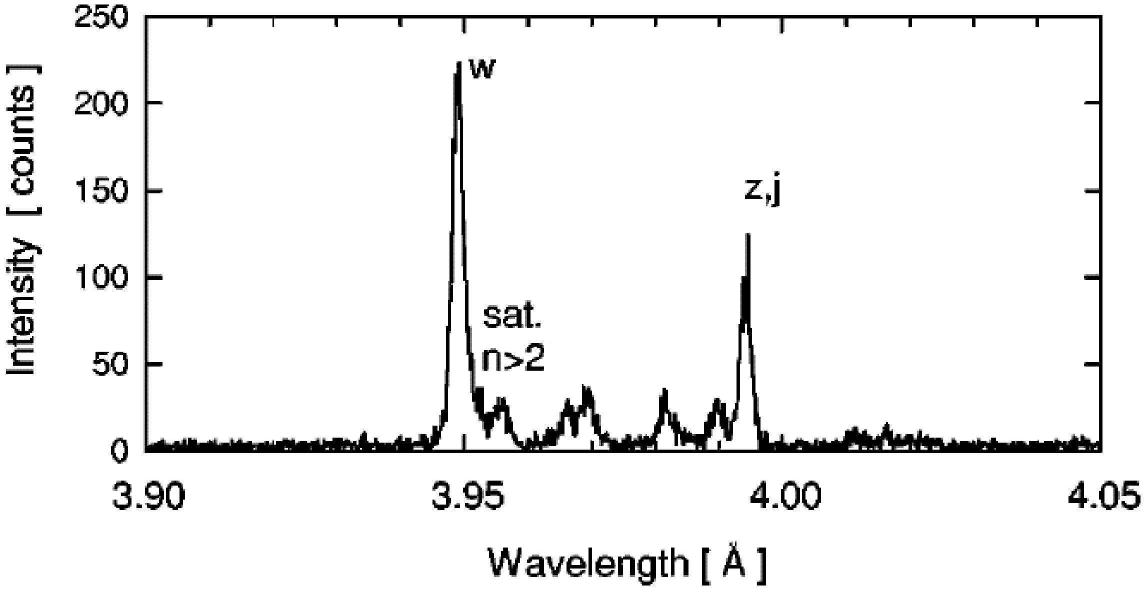

Figure 4.20: A spectrum containing spectral lines originating from transitions in multiply excited ions after dielectronic recombination (from [BRF02]). The satellite line on the lower energetic flank of the w line is due to spectator electrons on higher shells ($n > 2$) during the w transition. The line indicated as j is almost degenerate with the z line and corresponds to the transition $1s2p^2\ {}^2D_{5/2} \rightarrow 1s^22p\ {}^2P_{3/2}$.

4.5.3 Analysis of the a/b distance ratios

With the line symmetry confirmed, one can proceed in the data analysis. The a/b distance ratios of the Ar^{17+} Lyman-α_1 transition obtained in the measurement are depicted graphically in Fig. 4.21 as a function of the crystal angle. Figure 4.22 shows the evolution of the spectrometer temperature during the measurement sequence. As

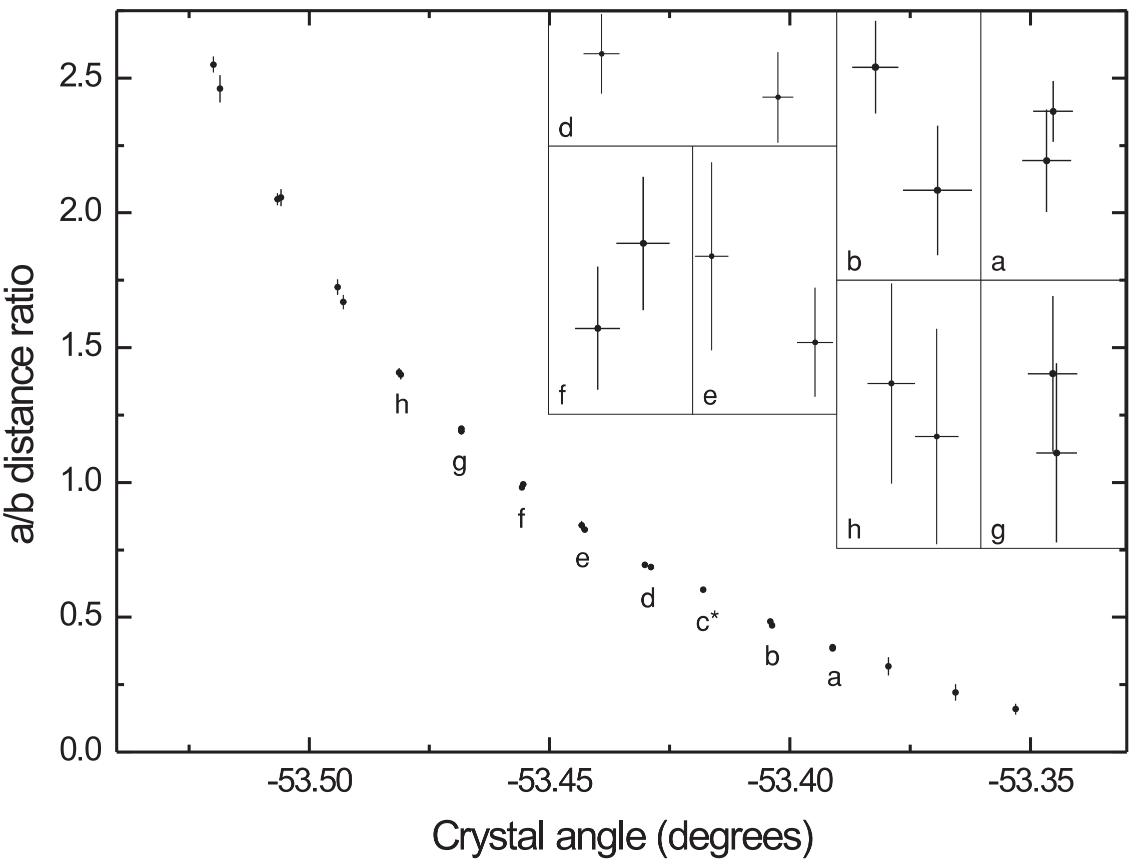

Figure 4.21: a/b distance ratios obtained from the analysis of the Lyman-α spectra. The inserts show magnifications of some of the data points (magnification scaled for best fit to box size). The three rightmost data points as well as datapoint c* do not have a directly neighbouring data point and have not been magnified. The error bars of the three leftmost pairs of data points are visible without magnification. The horizontal differences between each pair of data points are irrelevant for the results, but show the reproducibility of the positioning procedure, despite the long time intervals between the acquisition of the data points.

shown in Fig. 4.21, two data points have been obtained at most crystal orientations at different times. The time gap between two such measurements is about 40 hours, in which exposures at many varying crystal angles (in particular also at orientations where the radiation of the other transitions under study is recorded) have been made. Since the error bars are very small in comparison to the absolute scale of Fig. 4.21, magnifications of most data point pairs are inserted in the figure. The direct neighbour of the data point marked as c* was omitted from the figure because it had a surprisingly large error bar. It turned out that this was due to the fiducial interpolation routine needing to extrapolate because of the way the crystal angle had evolved during the x-ray exposure (Fig. 4.11, bottom left progression). This was the

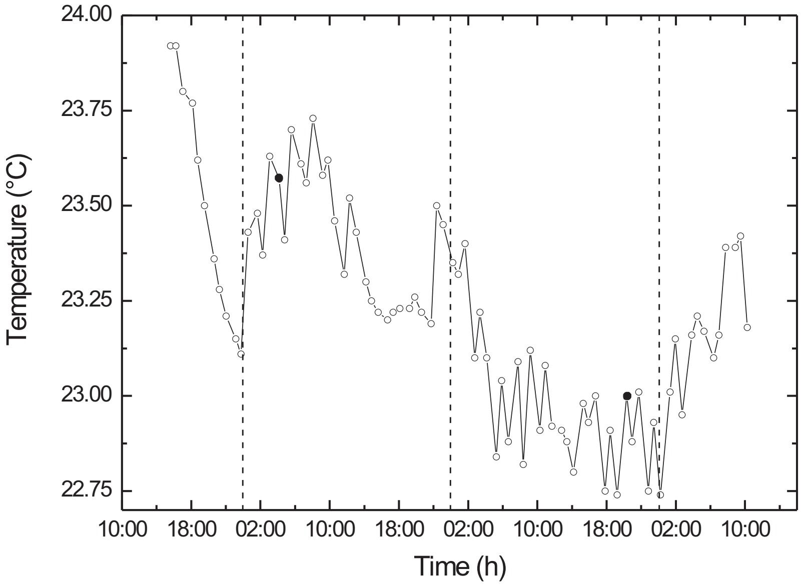

Figure 4.22: Spectrometer temperature during the measurement. A temperature reading was taken after each x-ray exposure. The dashed vertical lines indicate days, the two full points are the temperature readings of the data points labelled "f" in Fig. 4.21.

only data point where an extrapolation has been applied, *i.e.* where the evolution of the crystal angle with time showed an unexpected yet unexplained behaviour, justifying the omittance of this point.

From the spectrometer temperature evolution shown in Fig. 4.22 it is seen that even though the temperature varied by more than 0.5 °C and the time gap between two direct neighbours is almost two full days, the corresponding distance ratios a/b always agree well within their error bars. Moreover, there is no apparent reason that would indicate that the instrument's temperature is systematically higher or lower while recording spectra for different transitions. Hence, the a/b distance ratios were not corrected for the corresponding temperature reading. Such a correction is considered to rather introduce new errors than increase the overall precision, as the temperature dependence would have to be modelled somewhat arbitrarily.

As described in Chapter 3.2.1, the a/b distance ratio curve of the transition under study has to be fitted simultaneously with the a/b distance ratio curve of the reference transition. This is displayed in Fig. 4.23 for the Lyman-α_1 and the w transition of argon. In the data fit the parameters L, p and q were shared, with the constraints that p and q are both half the mean value of the fiducial distances, in units of pixels.

Whereas L is in principle known from an independent measurement, it was left as a free parameter in the fit to account for the misalignment between the fiducials'

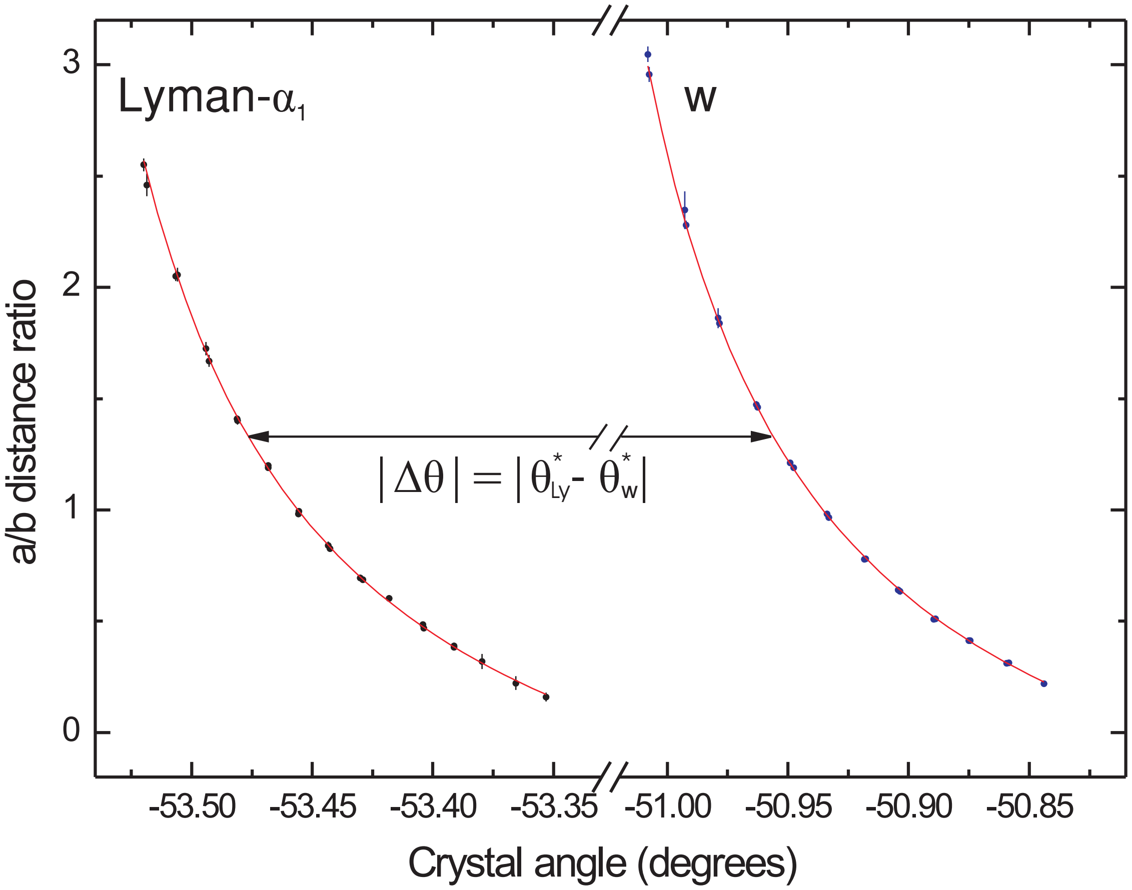

Figure 4.23: a/b distance ratios of the Lyman-α_1 transition (left) and the w transition (right). The curve is a fit of Eq. (3.1) to this data, sharing the parameters p, q and L. Hence, the horizontal distance of both curves is the same at all distance ratios a/b. Since the distance ratio a/b is a measure for the reflection position of the x-rays on the crystal, this distance corresponds to the difference of the Bragg angles of the two transitions. The corresponding plot for the z transition is very similar and thus not shown here.

virtual source volume and the EBIT source volume. Following the scheme described in Chapter 3.2.1, two fits of the Lyman-α_1 a/b distance ratios together with those of the w and z transitions were made, respectively. The results of both fits and the difference of the Bragg angles derived thereof are listed in Table 4.8. With the specified pixel size of 24 μm, the values for L found in the fits correspond to a fitted distance between trapped ions and the CCD camera of 1874(4) mm, as compared to a measured value of 1815(2) mm. The discrepancy is believed to originate from the light fiducial source point being located closer to the x-ray spectrometer than the trap, leading to a different curvature of the a/b distance ratio than if it were positioned correctly.

Table 4.8: Results of the fits of Eq. (3.1) to the distance ratio curves.

	Lyman-α_1 $\leftrightarrow$ w	Lyman-α_1 $\leftrightarrow$ z
L	77943(271) pixel	78210(249) pixel
$\theta^*_{Ly\alpha1}$	$-53.45594(16)^\circ$	$-53.45595(14)^\circ$
$\theta^*_{w/z}$	$-50.93543(7)^\circ$	$-50.40348(1)^\circ$
χ^2	1.02	1.06
$\Delta\theta$	$2.52051(17)^\circ$	$3.05246(14)^\circ$

4.5.4 From Bragg-angle differences to wavelengths

To obtain the wavelengths of the w and the z transitions from these angular differences, the lattice constant d of the Si-(111) crystal is needed. However, the Si-(111) crystal used in this work has not been characterised, and its lattice constant was not known from a measurement. Precision crystal characterisation has been performed by the x-ray optics group of the University of Jena [För] on several crystals of the same batch as the Si-(111) crystal used in this work (among them another Si-(111) crystal). This study confirmed all crystals to have low mosaicity and hardly any impurities, justifying to assume the crystal used in this work to be a single crystal of good quality. Due to the high level of perfection reached in the industrial production of silicon crystals, the literature value of the silicon lattice constant d found in CODATA [MT00] is generally taken to be valid for any Si single crystal on a level of 1 ppm [Bec]. The value of the Si lattice constant recommended by CODATA, $2d = 6.27120273(18)$ Å (in vacuum at 22.5°C) was corrected for using the linear temperature expansion coefficient of silicon at room temperature, $2.56 \cdot 10^{-6}\,\mathrm{K}^{-1}$ [MT00]. The mean temperature measured during the measurement was 23.2(3)°C, with the error being the standard deviation of the measured temperatures from the mean value. Thus, the lattice constant used in the data analysis of this work was $2d = 6.271214(8)$ Å, with the standard deviation of 1.3 ppm being dominated by the temperature shifts during the measurement. In order to reach the ppm or even sub-ppm accuracy level, work is in progress to stabilise the spectrometer temperature to ±0.1°C.

With this value of the Si-111 crystal lattice constant the Bragg angle of the Lyman-α_1 reference line was obtained using the relation

$$\lambda = 2d \sin\theta \left(1 - \frac{\delta_\lambda}{\sin\theta^2}\right) \ , \qquad (4.9)$$

Table 4.9: The error budget of the Ar^{16+} w and z transition energy measurement.

	w		z	
Error source	(ppm)	(meV)	(ppm)	(meV)
Uncertainty of reference	4.6	14	4.5	14
Crystal lattice constant	0.2	0.7	0.3	0.8
Statistical uncertainty	3.8	12	3.0	9.2
Specified accuracy of ang. measurement	1.5	4.8	1.5	4.6
Adjustment of visible light assembly	3	9.2	4.2	13.1
Total uncertainty	6.8	21.2	7.0	21.8

and therefore

$$\theta = \arcsin\left[\frac{1}{4d}\left(\lambda + \sqrt{\lambda^2 + 16d^2\delta_\lambda}\right)\right] , \tag{4.10}$$

where δ_λ is the refractive index of the Si-111 crystal with the lattice constant d at the wavelength λ. According to [cxr] the values of δ_λ are $\delta_{\mathrm{Ly}} = 4.47\cdot10^{-5}$, $\delta_w = 4.99\cdot10^{-5}$ and $\delta_z = 5.1\cdot10^{-5}$. The wavelength of the Ar^{17+} Lyman-α_1 reference transition was measured by Beyer *et al.* [BDFL85] as 3731.105(19) mÅ, which corresponds to 3322.989(17) eV, in good agreement with a state-of-the-art theoretical prediction of 3322.991 eV [JS85].

The Bragg angle differences listed in Table 4.8 were added to the reference angle obtained through Eq. (4.10) from the experimental reference wavelength. With these Bragg angles and Eq. (4.9), the wavelengths of the w and z transitions were determined. The total uncertainty of the respective transition wavelengths were estimated using the error propagation law. Error budgets are listed in Table 4.9, where the one named "statistical uncertainty" reflects the error in the determination of the Bragg angle difference. The result for the transition energies of the w and z transitions listed in Table 4.10 are compared with other experimental data and theoretical predictions in Chapter 4.6.

Table 4.10: The transition energies and wavelengths of the Ar^{16+} w and z transitions measured in this work. These energy-wavelength conversion factor used is $hc = 12398.4191\cdot10^{-6}\,\mathrm{eV\,m}$.

	w	z
Result (Energy)	3139.538(21) eV	3104.128(22) eV
Result (Wavelength)	3949.122(27) mÅ	3994.171(28) mÅ

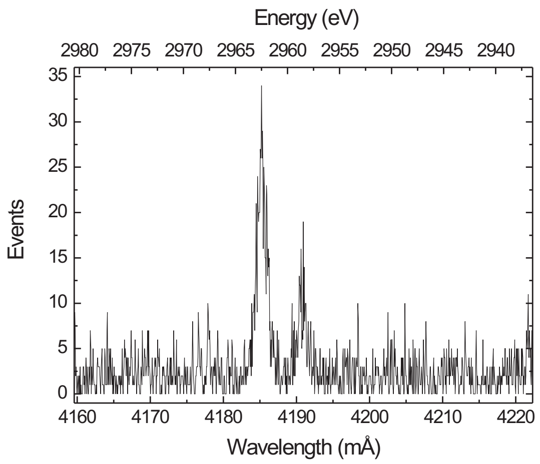

Figure 4.24: An exemplary Cl^{16+} Lyman-α spectrum. The spectrum was acquired in a 60 minutes exposure; in total 16 such spectra were obtained in the measurement.

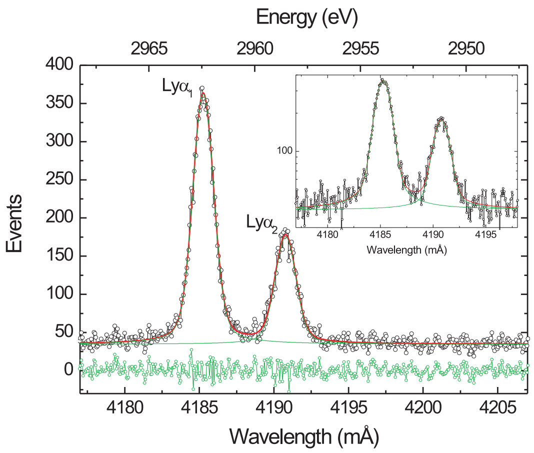

Figure 4.25: Sum spectrum of 16 Cl^{16+} Lyman-α spectra, Voigt fit and residuals. The insert shows the same spectrum on a logarithmic scale.

4.5.5 Completing the measurement: chlorine Lyman-α

The measurement of Ar-ion emission lines was stopped as soon as the statistical uncertainty was below the one in the reference wavelength. For the remaining beamtime, it was decided to inject chloroform vapor instead of argon into the trap to be able to study transitions in chlorine ions. While the laboratory had to be entered to connect the chloroform vial to the gas injection system, it was not necessary to work on the EBIT platform or to perform any other actions that could result in a change of the positions of either trap or spectrometer. In particular, the EBIT electron beam was not turned off and the trapping parameters were left unchanged. Hence, the position of the trapped chlorine ions can be assumed to be to a very good approximation identical to the one of the argon ions that were investigated before.

Since only about 20 hours of measuring time were left, exclusively spectra of the Lyman-α transitions of hydrogen-like Cl^{16+} were taken at slightly different crystal orientations. No spectrum of any other x-ray line, in particular the reference line, was taken during or after this measurement. The only change necessary at the spectrometer to detect the Lyman-α radiation of chlorine ($\approx 2960\,\mathrm{eV} \equiv 4119\,\mathrm{m\mathring{A}}$) was to reprogram the measurement sequence; the spectrometer was left untouched.

An exemplary Lyman-α spectrum of chlorine is shown in Fig. 4.24, the corresponding sum spectrum is presented in Fig. 4.25. The data analysis was carried out automatically in the same way as for the argon spectra. The a/b distance ratios of the Cl^{16+} Lyman-α_1 spectra were fitted using Eq. (3.1) and the distance ratios of the Ar^{17+} Lyman-α_1 transition as the reference. Again, the fit parameters p, q and

L were taken to be shared parameters. The results are listed in table 4.11. The Lyman-α_2 transition energy was not evaluated since the line appeared not always between the visible light fiducials and the statistical significance reached was lower.

The angular difference of 5.35706(12)° between the two distance ratio curves obtained from this fit was added to the Bragg angle of the Ar^{17+} Lyman-α_1 reference transition. In the calculation of the Cl^{16+} Lyman-α_1 transition energy from this angle using Eq. (4.9) the silicon refractive index of $\delta_\lambda = 5.57 \cdot 10^{-5}$ (as given by [cxr]) at that energy was used. Furthermore, since the mean spectrometer temperature during the chlorine run was the same as in the argon experiment (Cl: 23.0(1)°C, Ar: 23.2(3)°C), the same Si-(111) lattice constant value was used.

	$\mathrm{Ly}_{\alpha 1}(\mathrm{Ar}) \leftrightarrow \mathrm{Ly}_{\alpha 1}(\mathrm{Cl})$
L	77747(189) px
$\theta^*_{(\mathrm{Ar})}$	$-53.45596(12)°$
$\theta^*_{(\mathrm{Cl})}$	$-48.09890(1)°$
χ^2	0.94
$\Delta\theta$	5.35706(12)°

Table 4.11: Result of the fit of the distance ratio curves of the Ar and Cl Lyman-α_1 transitions.

The error budget of this data set is listed in table 4.12. In contrast to the argon measurement, it was not possible to check to the reference line continuously. Hence, while all three lines in the argon experiment would be affected by the drift of any parameter (*e.g.* temperature) in the same way, it is possible that the chlorine data were obtained under slightly different geometrical conditions than the Ar Lyman-α_1 reference line. Such a drift would affect the curvature of the a/b distance ratios of the Cl Lyman-α_1 transitions. Since this curvature is defined by the shared fit parameters p, q and L, a different curvature of the chlorine data points should also affect the argon reference data fit. However, the values of the parameters L and $\theta^*_{\text{Ar-Ly}\alpha 1}$ from the simultaneous fit of the chlorine data with the argon Lyman-α_1

Table 4.12: Sources of error and their influence on the final uncertainty of the measurement of the Cl^{16+} Lyman-α_1 transition energy.

Error source	(ppm)	(meV)
Uncertainty of reference	4.1	12.2
Crystal lattice constant	0.4	1.3
Statistical uncertainty	3.8	12
Specified precision of ang. measurement	1.6	4.8
Adjustment of visible light assembly	6.1	18.1
Reference not simult. measured (estimate)	2	5.9
Total uncertainty	8.8	26.1

data agree with the values resulting from the fits to the w and z transitions of He-like argon with the argon Lyman-α_1 data. It is therefore safe to assume that the error due to whatever unrecognised drift is smaller than the statistical uncertainty, since the reduced $\chi^2 \approx 1$ indicates that the data points are statistically distributed around the fitted curve, as they should. Nonetheless, an additional error contribution of 2 ppm has been arbitrarily assumed to account for any other unknown remaining uncertainty. In summary, the Cl^{16+} Lyman-α_1 transition energy obtained is $E(\mathrm{Cl}^{16+}_{Ly\alpha 1}) = 2962.361(26)\,\mathrm{eV}$.

4.6 Discussion of results

As reported in Chapter 1, the theoretical prediction of the energy levels in hydrogen-like ions is highly accurate, especially for ions of low to medium nuclear charge Z. Hence, the measurement of the Cl^{16+} Lyman-α_1 transition energy with respect to the Ar^{17+} Lyman-α_1 transition energy should be discussed first, as it is a good indicator whether or not the experiment was successful. Figure 4.26 and Table 4.13 show the Cl^{16+} Lyman-α_1 transition energy predicted by theory, as well as the result of previous experimental work by Källne *et al.* [KKRS84], Richard *et al.* [RSD$^+$84] and Deslattes *et al.* [DSJ85]. All three experiments used the same reference standard, namely the K_α radiation of gaseous argon. However, while they all used the energies of these transitions as $E(\mathrm{Ar}\ K_{\alpha 1}) = 2957.813(8)\,\mathrm{eV}$ and $E(\mathrm{Ar}\ K_{\alpha 2}) = 2955.684(13)\,\mathrm{eV}$, the most recent experimental literature values for these transitions are $E(\mathrm{Ar}\ K_{\alpha 1}) = 2957.682(16)\,\mathrm{eV}$ and $E(\mathrm{Ar}\ K_{\alpha 2}) = 2955.566(16)\,\mathrm{eV}$ [DK03], a change of about 0.12 eV. Hence, the experimental values given in [KKRS84], [RSD$^+$84] and [DSJ85] should be corrected[2] to the new value of their reference standard.

As can be seen from Fig. 4.26 and Table 4.13, the Cl^{16+} Lyman-α_1 transition energy measured in this work agrees excellently with the theoretical prediction. This shows that it is unlikely that any relevant systematic error source has been ignored in the measurement. This result is by a factor of 4 more accurate than any previous measurement.

The measured z transition energy of the two-electron system Ar^{16+}, where the excited state is comparatively little affected by electronic correlation, agrees within error bars with the theoretical predictions (Fig. 4.27). No other experimental value

---

[2] Using the mean value of the energy differences of their reference transition energies to the recent ones without respecting the given errors and also leaving the errors of the results of [KKRS84], [RSD$^+$84] and [DSJ85] unchanged.

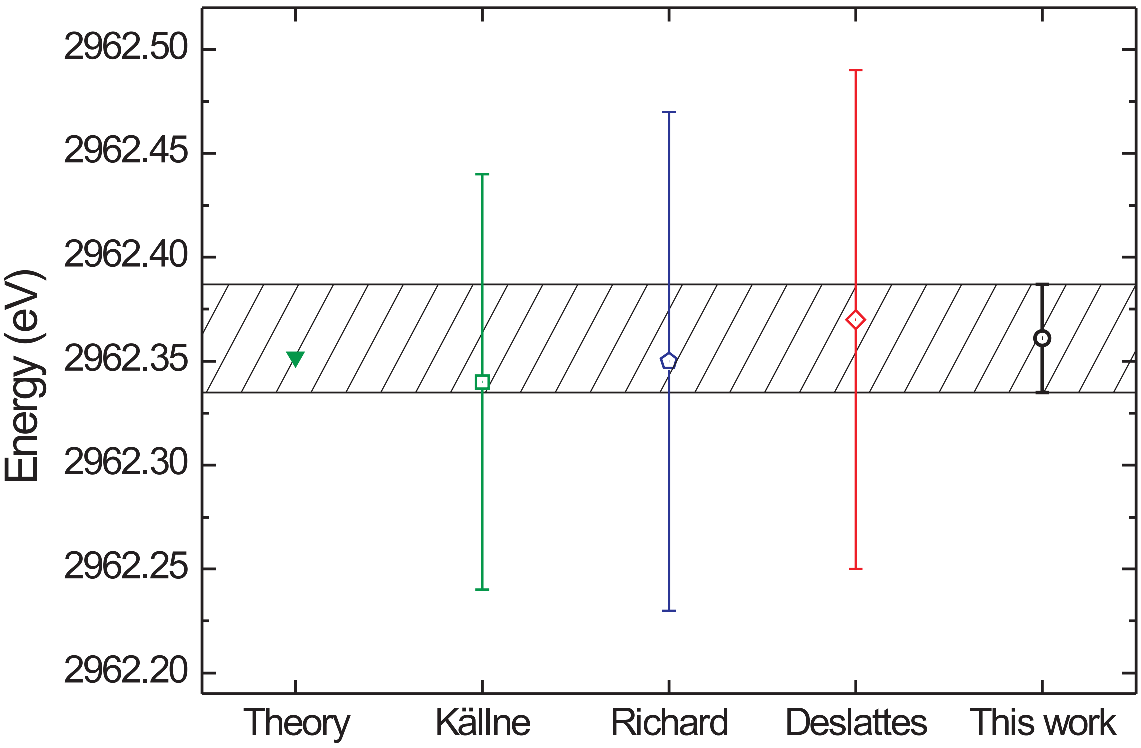

Figure 4.26: Comparison of the present result for the Cl^{16+} Lyman-α_1 transition energy with theoretical and previous experimental work: Theory [JS85]; Källne [KKRS84]; Richard [RSD$^+$84]; Deslattes [DSJ85]. The results from previous experiments were corrected for a change of the recommended values of the Ar K_α reference lines (see text).

Table 4.13: Comparison of the theoretical value and previous experimental results for the Cl^{16+} Lyman-α_1 transition energy with the present data. Note that although the results from previous experiments have been corrected for changes in their reference standard, due to their large error bars, this work also agrees with their uncorrected values.

Cl^{16+} Lyman-α_1	uncorrected	corrected
Reference [KKRS84]	2962.460(100) eV	2962.340(100) eV
Reference [RSD$^+$84]	2962.470(120) eV	2962.350(120) eV
Reference [DSJ85]	2962.490(120) eV	2962.370(120) eV
Avg. previous expt. work	2962.352(65) eV	
Theory [JS85]	2962.352 eV	
This work	2962.361(26) eV	

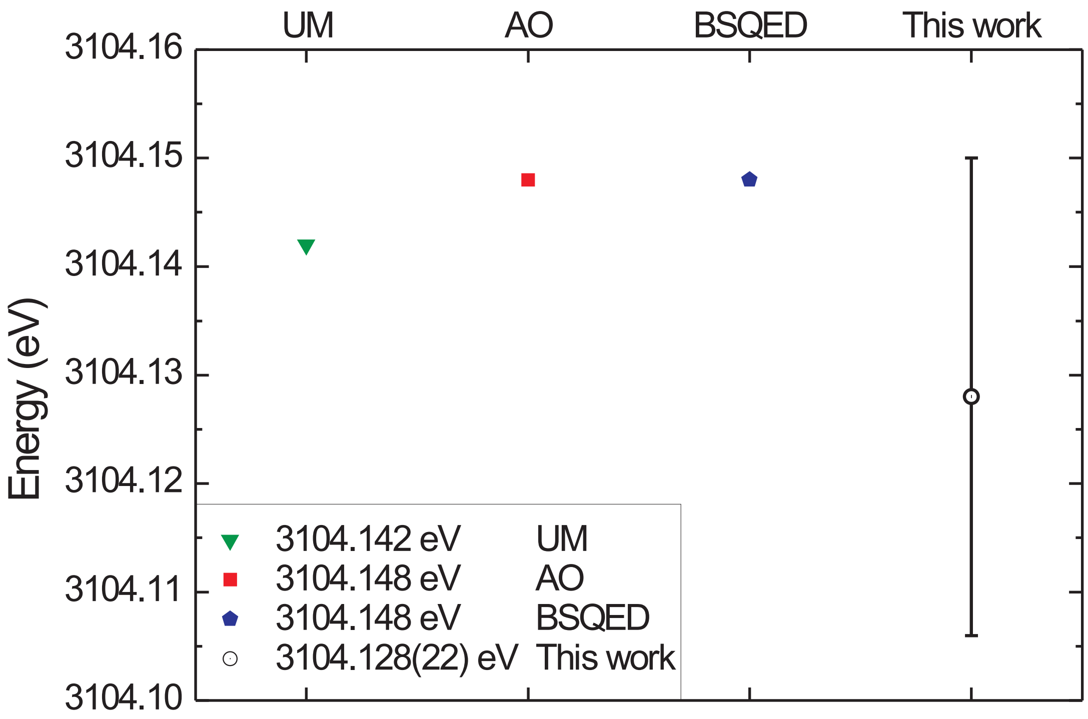

Figure 4.27: Comparison of the present result for the Ar^{16+} z transition energy with theoretical predictions: (UM) unified method [Dra88]; (AO) all-order [PJS94]; (BSQED) bound state QED [ASY$^+$05]; the value found in [Dra88] was converted from cm^{-1} to eV using the conversion factor $hc = 1.23984191 \cdot 10^{-6}\,\mathrm{eV\,m}$.

for this transition to compare with is available for argon and, also for other helium-like ions, only few experimental values are available, namely for vanadium (V^{21+}) [CPH$^+$00], germanium (Ge^{30+}) [MBV$^+$92] and krypton (Kr^{34+}) [WBDB96].

Finally, the w transition energy of Ar^{16+}, where the electronic correlation plays a larger role than in the case of the z transition energy, has been measured in this work. As shown in Fig. 4.28, the value obtained agrees very well with the previous experiment by Deslattes *et al.*, while it disagrees with all predictions.

To summarise, the experimental result for the transition energy in the Cl^{16+} one-electron system is found to be perfectly predicted by theory, the measured value for a transition in a two-electron system little affected by electronic correlation is less satisfactorily described by theory and, finally, the measurement of a line in a two-electron system stronger affected by electronic correlation disagrees with all theoretical results. This gives rise to the conclusion that the theoretical description of electronic correlations in two-electron systems may still be incomplete on the present level of accuracy reached in our experiment.

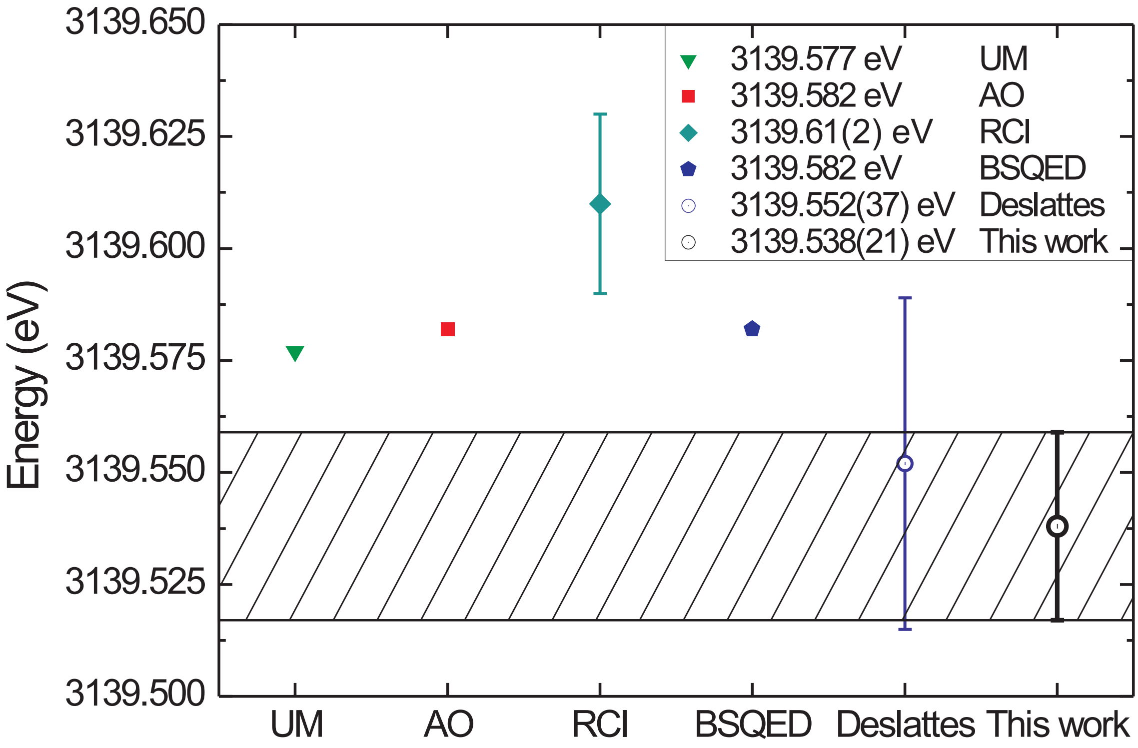

Figure 4.28: Comparison of the present result for the Ar^{16+} w transition energy with theoretical and previous experimental work: (UM) unified method [Dra88]; (AO) all-order [PJS94]; (RCI) relativistic configuration interaction [CCJS94]; (BSQED) bound state QED [ASY+05]; Deslattes *et al.* [DBF84]. The value found in [Dra88] was converted from cm^{-1} to eV using the conversion factor $hc = 1.23984191 \cdot 10^{-6}\,\mathrm{eV\,m}$.

4.6.1 Comparison of the different theoretical approaches

This work's results for the w and z transition in helium-like argon are compared with predictions obtained by means of four different theoretical approaches. The eldest calculation referred to in this work used the unified method (UM) developed by Drake [Dra88]. Drake employed a Hylleraas-type approach (see Chapter 1.3.4), *i.e.* highly correlated non-relativistic wave functions, corrected for relativity and QED effects. Due to the nature of the wave functions, these calculations are particularly useful for low-Z ions, where correlation effects (non-radiative corrections, see Fig. 1.3) are important and relativistic effects play a minor role. As mentioned in Chapter 1.3.6, the QED corrections to the non-relativistic energy levels were obtained by using the leading terms of a series expansion in αZ. The total uncertainty of the calculation given by Drake is $\pm 1.2(Z/10)^4\,\mathrm{cm}^{-1}$, corresponding to 2 meV in the case of argon. This value only takes into account the estimated uncertainties due to the incomplete treatment of the relativistic corrections. It should be emphasised that giving error estimates for predictions is by no means a common feature of theoretical works. It is, though, highly desirable to have such estimates, since they help to distinguish numerical problems resulting from the approximations used from the genuine physics issues related to effects taken or not taken into account.

The relativistic all-order many-body perturbation theory calculations (AO) by Plante *et al.* [PJS94], as well as those obtained through the relativistic configuration interaction approach (RCI) by Cheng *et al.* [CCJS94] base on a no-pair Hamiltonian. The electron correlation is taken into account within the Breit approximation. While the former included the QED values from the previously mentioned work by Drake in their calculations, the latter obtained their QED contributions from one-loop QED corrections in a local screening potential [CC00]. Even though their QED values agree with those of Drake, in the case of argon the uncertainty of those calculations is 0.02 eV [Che] as indicated by the error bar in Fig. 4.28. There is no value available for the z-transition energy in the RCI reference.

The method applied by Artemyev *et al.* [ASY$^+$05] is an *ab initio* bound state QED (BSQED) calculation. Here, a non-correlated relativistic calculation delivers the one-electron level energies, and the electron-electron interaction was accounted for through the exchange of one and two virtual photons. This procedure accounts for non-radiative QED effects in the electron-electron interaction, *i.e.* higher-order retardation and negative continuum contributions. The clear emphasis of that work lies on the treatment of the QED contributions to the energy levels, which are likely to be highly accurate.

Generally spoken, Drake's approach is more sophisticated than the other three in the non-relativistic part of the correlation energy, and so it yields more accurate results for low Z, where correlation effects are important. All methods mentioned here include the exact one-electron relativistic energies to all orders in αZ, as well as the lowest order (in α) relativistic corrections to the correlation energy. However, in the UM the higher order relativistic corrections to the correlation energy are neglected in contrast to the other approaches (at least to some extent), and so AO, RCI and BSQED become more accurate than the UM for higher Z values. Thus, for high Z, a difference between the UM and the other calculations can be interpreted in terms of higher-order relativistic corrections to the correlation energy. The leading term missing in the UM is of order $(\alpha Z)^4$. On the other hand, differences at low Z values are a hint to inadequacies in the representation of the non-relativistic correlation energy relativistic approaches use (a comparison between UM and RCI is found in [YD95]). The dividing line between "high Z" and "low Z" is somewhat undefined around $Z = 25$ [Dra04].

In the case of argon, the QED corrections predicted by Drake differ from the BSQED results by about 10 meV (see Tables 4.14 and 4.15). Replacing the QED corrections in Drake's calculations with those of Artemyev *et al.* shifts the result for the w-transition energy to $E_{w,corr} = 3139.585\,\mathrm{eV}$ and that of the z-transition energy to $E_{z,corr} = 3104.150\,\mathrm{eV}$, bringing both to better agreement with the BSQED calculation (within 3 meV). On the other hand the same can be done with the result of the AO calculation, since it also uses Drake's QED corrections. However, as the agreement of the AO and the BSQED calculations was perfect before, such a procedure introduces a disagreement. Hence, the difference between these theoretical approaches cannot be explained simply by the different treatments of the QED corrections.

Consequently, with Drake's UM being accurate especially at low Z and the other methods being better suited for high Z, it is possible that the intermediate $Z = 18$ of argon lies in the region where none of them can yield accurate results. Since the most important difference between AO, RCI and BSQED on one side, and the UM on the other side is the way the electron-electron interaction is treated, this may well be the key issue for understanding the generally poor agreement of the calculated w and z transition energies with this work's experimental results.

Finally, it should be mentioned that Trassinelli *et al.* [TBB$^+$04] have recently measured the w transition energy in helium-like argon with respect to the z-transition energy, which apparently was calculated using an MCDF calculation quoted as $E_z = 3104.13\,\mathrm{eV}$. With respect to this reference, their value for the transition energy of the w line is $E_w = 3139.537(10)\,\mathrm{eV}$. It should be noted that both the predicted value for the z-transition energy (which they use for calibration of their data) as well

Table 4.14: Contributions to the binding energies as calculated by Drake [Dra88], in eV. E_{nr}: non-relativistic level energy; ΔE_{rel}: relativistic corrections; ΔE_{mp}: mass polarisation corrections; ΔE_{QED}: QED corrections; ΔE_{ns}: finite nuclear size; E_{Sum}: total level energy.

State	E_{nr}	ΔE_{rel}	ΔE_{mp}	ΔE_{QED}	ΔE_{ns}	$\mathbf{E_{Sum}}$
$^1S_0$	4106.337	15.377	$-8.5 \cdot 10^{-4}$	−1.046	$-8.4 \cdot 10^{-3}$	**4120.659**
$^3S_1$	1011.297	5.360	$-6.7 \cdot 10^{-5}$	−0.138	$-1.0 \cdot 10^{-3}$	**1016.517**
$^1P_1$	978.996	2.099	$-8.1 \cdot 10^{-3}$	−0.004	$-9.9 \cdot 10^{-6}$	**981.083**
$^3P_1$	993.497	3.617	$+7.9 \cdot 10^{-4}$	+0.007	$+3.6 \cdot 10^{-5}$	**997.130**

Table 4.15: Contributions to the binding energies as calculated by Artemyev *et al.* [ASY+05], in eV. E_{Dirac}: Dirac energy including finite nuclear size; E_{int}: electron-electron interaction correction; E_{QED}: total QED contributions (see table 4.16 for more details); E_{rec}: relativistic recoil correction; E_{sum}: total level energy. (*) The total level energies of the quasi-degenerate levels $^1P_1$ and $^3P_1$ are obtained as the eigenvales of a 2×2 matrix where the diagonal elements are the sum of the single contributions to the respective level and the offdiagonal elements are as given in column E_{sum}.

State	E_{Dirac}	E_{int}	E_{QED}	E_{rec}	$\mathbf{E_{sum}}$
$^1S_0$	4427.4154(3)	−305.6560	−1.0366(1)	−0.0575	**4120.6653(4)**
$^3S_1$	1108.0563	−91.3873	−0.1380(1)	−0.0141	**1016.5170(1)**
$^1P_1$	1103.2520	−118.6220	−0.0032(1)	−0.0162	**981.0832(1)***
$^3P_1$	1108.0575	−114.4514	+0.0082(1)	−0.0108	**997.1309(1)***
off-diag.	0	−6.6353	−0.0026(1)	−0.0078	−6.6456*

Table 4.16: One- and two-electron QED corrections as calculated by Artemyev *et al.* [ASY+05], in eV. Total 1-el.: total one-electron QED contribution; Scr. SE: screened self-energy; Scr. VP: screened vacuum polarisation; 2-ph.exch.: QED contributions due to exchange of two virtual photons; Total 2-el: the sum of these two-electron effects; h.o.: higher order effects.

State	Total 1-el.	Scr. SE	Scr. VP	2-ph.exch.	Total 2-el.	h.o.
$^1S_0$	−1.1310(1)	0.1116	−0.0072	−0.0091(1)	0.0953(1)	−0.0009
$^3S_1$	−0.1525	0.0154	−0.0010	0.0004(1)	0.0148(1)	−0.0003
$^1P_1$	−0.0062	0.0031	−0.0001	0.0001(1)	0.0031(1)	−0.0003
$^3P_1$	0.0043	0.0035	−0.0003	0.0010(1)	0.0042(1)	−0.0001
off-diag.	0	−0.0026	0.0002	−0.0004(1)	−0.0028(1)	0.0002

Table 4.17: Difference between the energy levels $^3S_1$ and $^1P_1$ in helium-like argon. AO claims to be exact to the quoted number of figures.

Reference	$E_w - E_z$
UM [Dra88]	35.434(2) eV
AO [PJS94]	35.4339 eV
BSQED [ASY$^+$05]	35.4339(1) eV
Experiment [TBB$^+$04]	35.407(10) eV
This work	35.410(4) eV

as the measured value of the w-transition energy are in very good agreement with this work's experimental results. Since no more details of the calculation quoted in [TBB$^+$04] than mentioned above are known, it is not compared with the other calculations presented before.

The uncertainty of only 3 ppm in the w-transition energy measured by Trassinelli *et al.* is a consequence of the close-lying reference z-line taken to be exact. If this work's data is analysed in the same way, *i.e.* using the z transition energy $E_z = 3104.13$ eV as reference, the w transition energy obtained is $E_w = 3139.540(4)$ eV, where the error, two and a half times smaller than that of Trassinelli *et al.*, is clearly dominated by the statistical uncertainty. Since setting the reference value fixed seems rather arbitrary, it is more interesting to compare the difference between the w and the z transition energies obtained in the two experiments instead (see Table 4.17). Both differences agree within 3 meV (out of 35 eV) and within both works' error bars, *i.e.*, perfectly.

By all means, the consistency of the results by Deslattes *et al.* [DBF84] and Trassinelli *et al.* [TBB$^+$04] with this work's experimental result is a clear indication that the theoretical description of helium-like argon is still incomplete, despite the apparent simplicity of the system and the claims of accuracy presented in the theoretical papers.

4.6.2 Comparison with measurements in other He-like ions

A number of experimental values for the w transition in helium-like ions of medium nuclear charge Z are found in the available literature. Figure 4.29 shows a compilation of these values, as well as the results of various calculations (UM, AO and RCI) in comparison to the prediction by Artemyev *et al.* [ASY$^+$05] in dependence of the nuclear charge Z. Beiersdorfer *et al.* [BBvH89] studied the w transition in

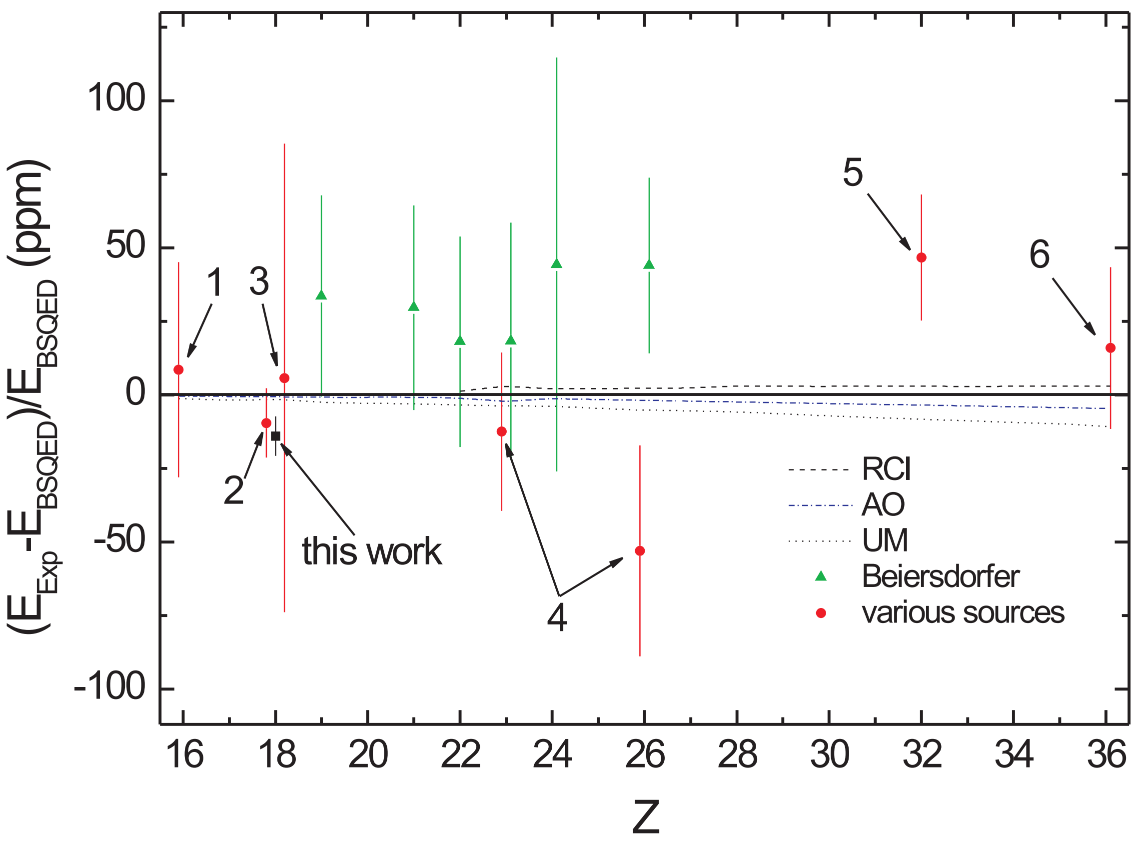

Figure 4.29: Comparison of the present result for the Ar^{16+} w transition energy with previous theoretical and experimental work in the He-like isoelectronic sequence. All data are normalised to the values of the w transition energy E_{BSQED} calculated by Artemyev *et al.* [ASY$^+$05]. RCI: relativistic configuration interaction [CC00]; (AO) all-order [PJS94]; (UM) unified method [Dra88]; Beiersdorfer *et al.* [BBvH89]; (1) Schleinkofer *et al.* [SBB$^+$82]; (2) Deslattes *et al.* [DBF84]; (3) Briand *et al.* [BMI$^+$83]; (4) Chantler *et al.* [CPH$^+$00]; (5) MacLaren *et al.* [MBV$^+$92]; (6) Widmann *et al.* [WBDB96]. Figures given in wavelength units in any of these references were converted to eV using the conversion factor $hc = 1.23984191 \cdot 10^{-6}\,\mathrm{eV\,m}$.

several elements, contributing most of the available data points. The measurements by Beiersdorfer *et al.* were performed in tokamak plasmas at the Princeton Large Torus (PLT) and used hydrogen-like transitions from the same source as reference. Another series of measurements of the w transition in a variety of elements has been performed by Aglitsky *et al.* [AAM$^+$88], employing a low-inductive vacuum spark (LIVS) as source of multiply-charged ions. For vanadium, chrome and iron, values are available from both measurements, agreeing well within their error bars. Still, Beiersdorfer suggests to exclude the LIVS data points from a comparison "because they used theory to account for blends with satellites. Therefore, these results are influenced by theory more than any of the others" [Bei05]. This statement seems

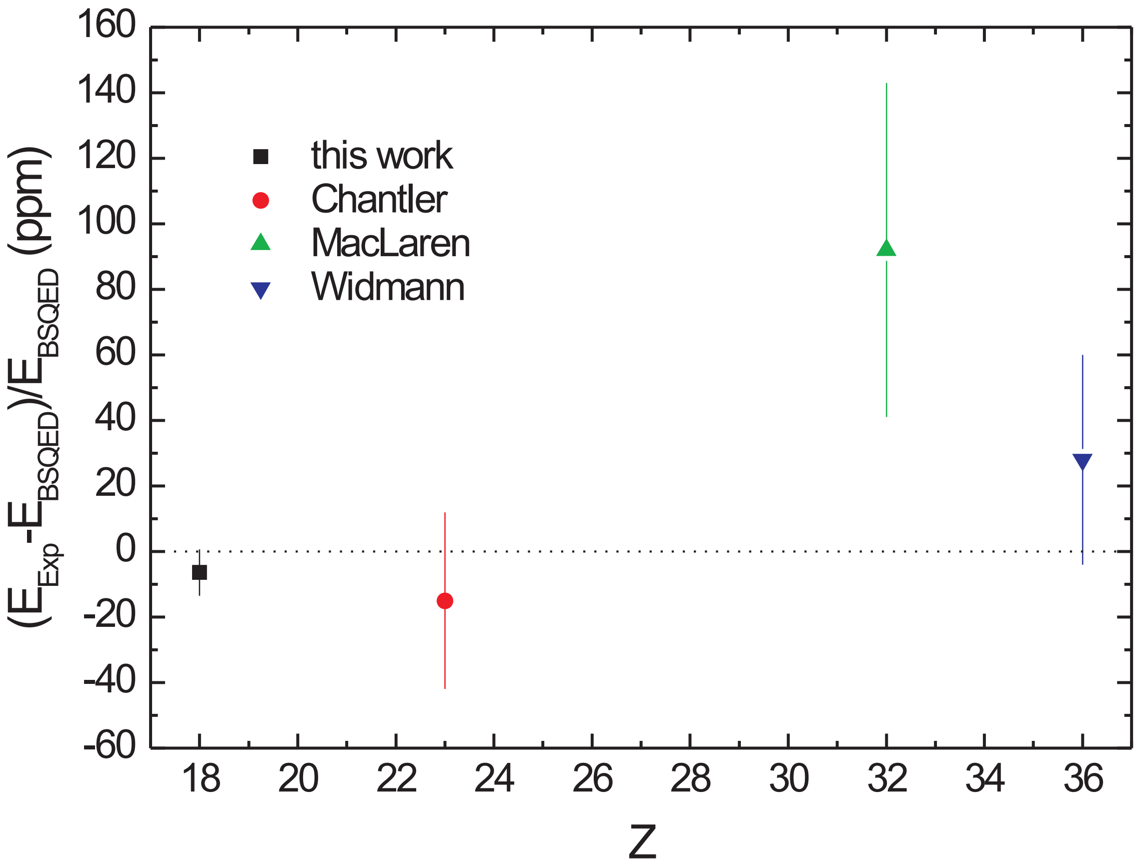

Figure 4.30: Comparison of the present result for the Ar^{16+} z transition energy with previous theoretical and experimental work in the He-like isoelectronic sequence. All data are normalised to the values of the z transition energy E_{BSQED} calculated by Artemyev *et al.* [ASY$^+$05]. Chantler *et al.* [CPH$^+$00]; MacLaren *et al.* [MBV$^+$92]; Widmann *et al.* [WBDB96]. Figures given in wavelength units in any of these references were converted to eV using the conversion factor $hc = 1.23984191 \cdot 10^{-6}\,\mathrm{eV\,m}$.

justified and, hence, the data by Aglitsky *et al.* are not included in the figure. Figure 4.30 shows a similar comparison for the z transition energy, for which less experimental values are available.

From Fig. 4.29 and Fig. 4.30 one can see that the experiment performed in this work is the first one since the Deslattes experiment in 1984 [DBF84] in which a significant reduction of the experimental error bar was achieved. This was only possible due to the use of both, the HD-EBIT as a superior ion source and our novel x-ray spectroscopic technique. Despite the disagreement between experiment and theory for the w transition energy at $Z = 18$ found in this work, a general trend of theory to predict larger energies than the experimental values clearly cannot be claimed. It seems worthwhile to extend these high precision studies to a larger number of elements along the He-like isoelectronic sequence, and we hope our results encourage other groups to independently perform such high precision measurements for an impartial test of the theory of helium-like ions of moderate nuclear charge number Z.

4.6.3 Sensitivity of the measurement

From the values displayed in Tables 4.14 to 4.16, it becomes clear that extreme experimental precision is necessary to probe effects of interest to modern atomic structure physics. In the measurements presented in this work, an accuracy of 7 ppm was reached in the transition energy measurements of the w and z transitions in helium-like argon (21 meV and 22 meV uncertainty, respectively), and an accuracy of 9 ppm, or 26 meV, was reached for the Lyman-α_1 transition in hydrogen-like chlorine (by using the Ar^{17+} Lyman-α_1 transition as reference). The Dirac energy for the Cl^{16+} Lyman-α_1 transition is 2963.310 eV. The total lamb shift of -0.947 eV includes a contribution from the vacuum polarisation of 0.068 eV (both figures taken from [KKRS84]). Since the uncertainties of previous measurements of the latter transition were 100 meV or larger, the present measurement is the first one sensitive to resolving the vacuum polarisation contribution and achieves a sensitivity to the total Lamb shift on a level of better than 3 %.

The precision reached in the w transition energy measurement corresponds to 1.9 % of the one-electron QED contribution to the ground state, and it even probes the two-electron QED contribution at a level of 22 %. In the case of the z transition energy measurement, where the excited ${}^3S_1$ state is even more sensitive to QED effects, the one-electron QED contribution to the excited state can be resolved as well. This is all the more exciting, since it is one of the first measurements of this transition in highly charged ions at all.

Chapter 5

Conclusion and Outlook

The aim of this work was to perform high-precision wavelength measurements on electronic transitions in helium-like ions of medium nuclear charge Z produced and trapped in the Heidelberg-EBIT. In order to reach a competitive accuracy of 10 ppm or better with the existing flat crystal x-ray spectrometer built in [Bra03], it was necessary to develop a novel method of x-ray reflection position determination on the Bragg crystal. This goal was achieved by projecting two beams of visible light, so-called fiducials, onto the position sensitive CCD detector, with the Bragg-crystal acting as a simple mirror for the fiducials. The positions at which the fiducials appear on the CCD camera yield full information about the crystal orientation. The relative position of these with respect to an x-ray line, which in contrast to the fiducials has to fulfill Bragg's law, corresponds to a certain reflection position of the x-ray line on the Bragg crystal. The fact that the fiducials and the x-rays have a common geometrical (virtual) origin allows to use distance ratios according to Thales' theorem. In this way, a large insensitivity to most alignment parameters is achieved, in contrast to all earlier techniques.

By actively changing the crystal's angle the reflection position of the x-rays on the crystal is shifted. This is monitored by observing the varying relative position of the detected x-ray line to the fiducials. By describing this shift of the x-ray line in dependence of the measured crystal angle with an analytical function, the angle fulfilling Bragg's condition to reflect the x-ray line at an arbitrary interpolated position on the crystal can be determined with very high accuracy. If this procedure is performed with two x-ray lines - a reference line and the line of interest - the difference of the Bragg-angles (defined by the crystal lattice spacing and the respective wavelengths) and, hence, the wavelength difference of the two x-ray lines can be measured with high accuracy. An important feature of this method is that no single x-ray photon is lost due to collimation, making this technique ideally suited for measurements at sources with low x-ray flux. Moreover, the fact that the reference line used in this method does not have to lie in close vicinity of the line of interest gives the possibility to accurately measure wavelengths with respect to any reference within the spectral range of the x-ray spectrometer. For the spectrometer configuration used in this work, the spectral range spans from about 5.48 Å($\approx$ 2260 eV) to 3.05 Å($\approx$ 4080 eV) x-ray wavelength. To the best of our knowledge, this x-ray spectrometer is the only one worldwide able to cover such a large spectral range with a precision of $\Delta\lambda/\lambda$ of the order of 10^{-5} and better using a single reference line. This has become possible only by means of our novel method of x-ray reflection position determination.

The idea to rather measure and describe the x-ray reflection position on the Bragg crystal in dependence of its orientation than to define it via collimation was developed in close collaboration with J. Braun [Bra06]. While his work focused on mechanical aspects like the necessary modifications to the original spectrometer design and the vector simulation of the method (needed for error estimates), the emphasis of the present thesis layed on the data acquisition and analysis of the first measurements, requiring several runs with hundreds of CCD spectra being processed and an accordingly large number of spectra to be fitted.

Since the novel method requires to obtain x-ray and visible light spectra at as many different crystal and camera orientations as possible, and since any user interaction with both the x-ray spectrometer and the EBIT are prone to disturb the measurement, the complete instrument's operation has been automatised. With the automatisation (also that of the HD-EBIT) developed in this work, a measurement can run without any user interaction over a complete EBIT cycle of up to ten days defined by a single fillig of the liquid helium dewar needed to cool the EBIT's superconducting magnet for that period of time. In this time span, x-ray and visible light spectra are acquired at an arbitrary number of different crystal angles, ensuring the maximum possible crystal and detector positioning reproducibility and instrumental stability since the EBIT laboratory remains closed and empty of personnel.

Due to the resulting amount of data - two visible light spectra and one x-ray spectrum are obtained at every crystal angle, such that several hundred spectra accumulate in one beamtime - a conventional, interactive data analysis would be extremely time consuming. For this reason, after careful investigation on how the visible light images containing the fiducials and the x-ray spectra need to be analysed, the complete data analysis routine was also automatised. In addition to the obvious benefit that all data sets of a whole beamtime can be analysed within less than one hour, allowing to perform extensive measurements needed for *e.g.* the characterisation of the visible light fiducials, the automated data analysis ensures that all spectra are treated equally, thus excluding any potential biasing towards some desired values.

Moreover, a slightly modified version of the data analysis programme written in this work is also used for the data analysis of other experiments. Here it was possible to directly compare the automated data analysis with a previous manual analysis of the same data set that had required several months of work [Sor05], confirming the correctness of the fitting routines employed.

Using the novel method, it was possible to measure the wavelength of the $1s2p\ ^1P_1 \rightarrow 1s^2\ ^1S_0$ (w) and the $1s2s\ ^3S_1 \rightarrow 1s^2\ ^1S_0$ (z) transitions in helium-like argon with respect to the Lyman-α_1 transition in hydrogen-like argon, being higher in energy by 183.5 eV and 219 eV than the lines of interest, respectively. To complete the experiment, the Lyman-α_1 transition energy in hydrogen-like chlorine was measured with respect to the same reference line. Although the transition energies of these two Lyman-α transitions are separated by about 361 eV, the theoretically predicted value for the Lyman-α_1 transition energy in hydrogen-like chlorine was reproduced within 9 meV, well within the small experimental error bar of 22 meV. As compared to previous measurements, the experimental accuracy of the result for this transition energy was increased by a factor of four, with an uncertainty of $\Delta\lambda/\lambda = 9\,\mathrm{ppm}$ (22 meV). This work's experiment is the first one sensitive to the effect of vacuum polarisation to the ground state in hydrogen-like chlorine.

In case of the two transitions studied in helium-like argon ions, an uncertainty of only 7 ppm for both transitions studied was reached. The precision in these measurements was limited mainly by the uncertainty of the reference line ($[w; z]$: $[4.6; 4.5]$ ppm), followed by the imperfect positioning of the visible light source ($[3.0; 4.2]$ ppm) and the statistical uncertainty of the data ($[3.8; 3.0]$ ppm). The measurement of the w transition energy is in good agreement with the previously most precise measurement, and the error bar size was decreased by almost a factor of 2. The z transition had not been measured in helium-like argon before.

While this work's experimental result for the Lyman-α_1 transition in hydrogen-like chlorine is in excellent agreement with the theoretical prediction, the transition energies in helium-like systems predicted by modern theoretical methods lie just within this work's error bar in case of the z transition, and disagree with the experimental result of the w transition energy by $2\,\sigma$. This work's result is consistent with two other precision measurements of the w transition energy in argon which corroborate, despite their larger error bars, a deviation from the theoretical predictions. This deviation becomes more pronounced with rising mutual electronic interaction contributing to the transition energy. Therefore, the discrepancy between theory and this work's measurement is believed to arise from an incomplete description of helium-like ions of medium nuclear charge Z. The physical reasons underlying these effects are still unknown.

The outlook of these experiments in the near future is driven by the objective of attaining an absolute energy scale independent from any reference lines. At this moment, J. Braun [Bra06] is working on a combination of the novel method of x-ray position reflection determination and a technique devised by W.L. Bond [Bon60]. In this technique, two detectors are needed, and the Bragg crystal is rotated to two different angles: one where the x-ray line of interest is reflected under the Bragg angle θ towards detector 1, and the other where the same x-ray line is reflected under the negative Bragg angle $-\theta$ towards detector 2. The resulting angular difference between the two crystal orientations $\xi_1 - \xi_2 = 180° - 2\theta$ directly yields the Bragg angle and, hence, the wavelength of the radiation under study. Since the only quantity except for the angle needed in this measurement is the crystal lattice constant (which, for Si, is a proxy for the meter's standard) this scheme allows one to completely forgo reference lines and, most importantly, their uncertainties. Using this method of absolute wavelength determination the wavelengths of transitions in helium-like and lithium-like systems will be measured in the future without the need of secondary standards. One might even envision, and there are strong arguments based on the high degree of symmetry of the detected lines which are free of satellites on any observable level, that x-ray lines from highly charged ions in an EBIT are prime candidates to serve as future x-ray standards.

Appendix A

Appendix

A.1 Spectrometer control programme

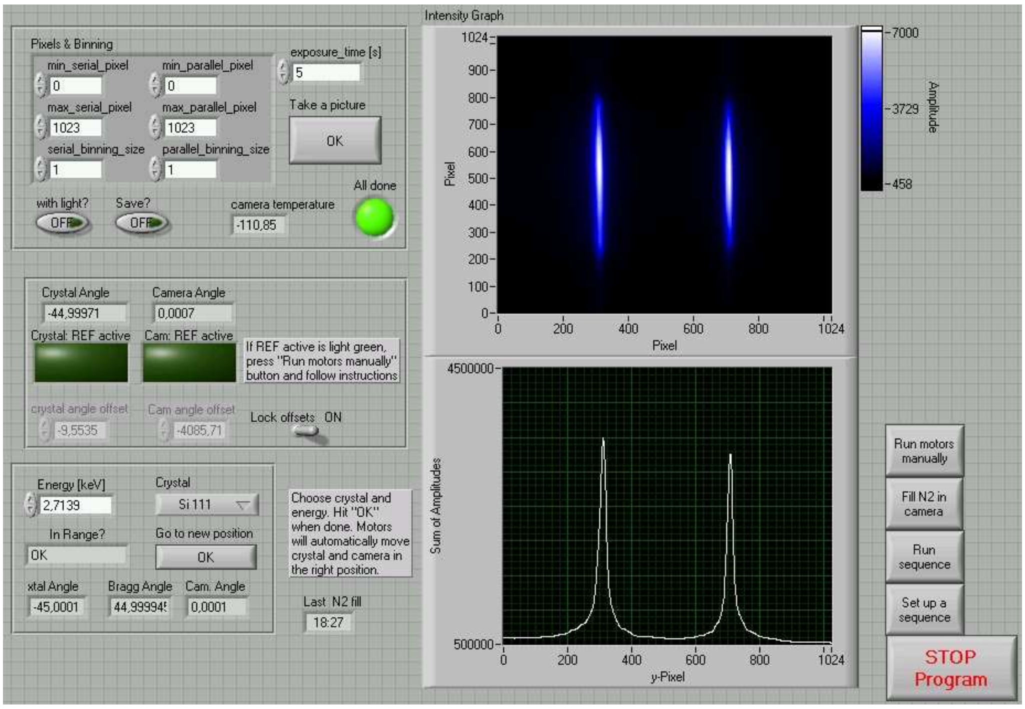

Pixels & Binning

min_serial_pixel 0

min_parallel_pixel 0

max_serial_pixel 1023

max_parallel_pixel 1023

serial_binning_size 1

parallel_binning_size 1

exposure_time [s] 5

with light? OFF

Save? OFF

camera temperature -110,85

Crystal Angle -44,99971

Camera Angle 0,0007

If REF active is light green, press "Run motors manually" button and follow instructions

crystal angle offset -9,5535

Cam angle offset -4085,71

Lock offsets ON

Energy [keV] 2,7139

Crystal Si 111

In Range? OK

Choose crystal and energy. Hit "OK" when done. Motors will automatically move crystal and camera in the right position.

xtal Angle -45,0001

Bragg Angle 44,99994!

Cam. Angle 0,0001

Last N2 fill 18:27

Figure A.1: Screenshot of the spectrometer control programme. With this programme the crystal and camera positions can be modified individually, exposures with and without visible light can be made, a measurement sequence can be set up and run from the interface. If the programme is running idle, liquid nitrogen is filled to the camera as soon as the camera temperature rises above −109°C.

The x-ray spectrometer control programme gives a user interface (UI) for all necessary aspects in the use of the spectrometer and is shown in Fig. A.1. First, there are two options to bring the crystal and camera into position. One can either use the "Run motors manually" button on the right hand side of the UI that starts a dialogue allowing the positioning of crystal and camera to arbitrary positions independently. This is especially important if the readout heads of the angular measurement devices have to be moved over their respective reference marks for calibration of the angle measurement. Once the angular readout is calibrated, the crystal and camera angle are shown on the main UI (middle left in the figure). The offsets of the angles read can be changed if necessary (*e.g.* after setting up the instrument). Once the angular readout is calibrated, crystal and camera can also be positioned by choosing an x-ray energy of interest as well as the crystal installed (lower left in the figure). The Bragg angle as well as the corresponding camera and crystal positions are calculated from this information, and if these positions are within the spectral range of the instrument (which is defined by the maximum bend of the camera bellow) both camera and crystal are driven to their respective positions by pressing the "Go to new position" button.

Once camera and crystal are in position and the camera temperature indicated is as desired, images can be taken with a chosen exposure time, camera region to be read out as well as pixel binning by pressing the "Take a picture" button (upper left in the figure). Depending on the position of the switch "with light?" the LED in the visible light assembly will be turned on during the exposure; if the switch "save?" is in the ON position the image will be saved to a location defined by the user in a dialogue. The image and its projection are shown in the intensity and x-y graphs, respectively. If the camera is not cold enough, or if the user fears that according to the "Last N2 fill" indicator the camera may become warm during a long exposure, liquid nitrogen will be filled by pressing the "Fill N2 in camera" button (bottom right in the figure).

One of the main features of the spectrometer control programme is its ability to run a sequence of exposures of arbitrary exposure time at user-defined crystal and camera positions automatically. The information about each exposure in the sequence needs to be entered as a single line into the file "c:\johannes\messungen\measurements.txt" in the form <exposuretime in seconds>:<crystalnumber>:<energy in keV>, *e.g.* "1800:5:3, 1395". Note that since the computer is running a german copy of the OS Windows 98, the decimal seperator needs to be entered as a comma instead of a point. The numbers assigned to the different crystals are listed in Table A.1. For the a/b-method, many different values around the central line energies must be entered into this file. Since this is a cumbersome process prone for errors when done manually, a subprogramme started when pressing the “set up a sequence” button in the main programme was included, helping in the creation of this file.

The interface of the sequence setup programme is shown in Fig. A.2. Here, an arbitrary number of lines of interest can be entered in the corresponding numeric control. The table where the line energies and the corresponding exposure times are entered expands according to the number of lines chosen. The “ok?” indicator on the right hand side of that list shows whether the energies entered are within the spectral range of the instrument. Also, exposure times of more than 7200 seconds are not allowed. Invalid entries are ignored when the measurement sequence information file is created. The range of energies around the central energy as well as the step width can be chosen arbitrarily.

Crystal	Number
LiF 420	0
LiF 220	1
Ge 220	2
Ge 111	3
Si 220	4
Si 111	5

Table A.1: Numbers of the crystals as needed for the sequence file.

A measurement sequence set up this way is started from the main programme by pressing the “run sequence” button.

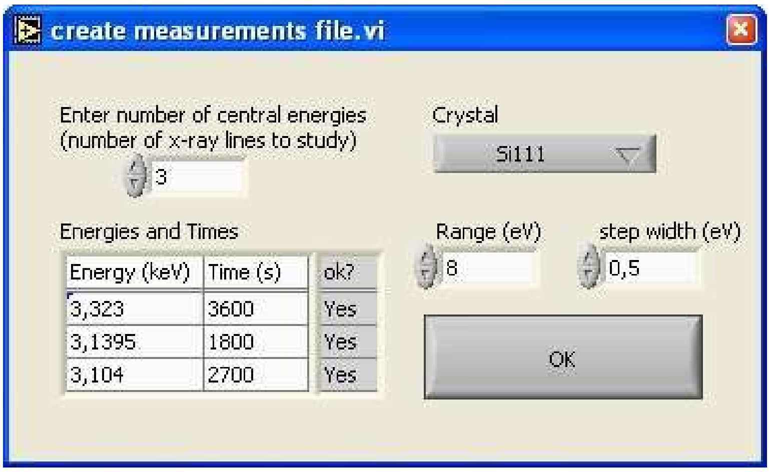

create measurements file.vi

Enter number of central energies (number of x-ray lines to study): 3

Crystal: Si111

Energies and Times

Energy (keV)	Time (s)	ok?
3,323	3600	Yes
3,1395	1800	Yes
3,104	2700	Yes

Range (eV): 8

step width (eV): 0,5

Figure A.2: Programme to set up a measurement sequence.

A.2 Tables

Table A.2: Ar^{17+} Lyman-α_1 automated fit results.

Crystal angle	Fiducial 1	Fiducial 2	x-ray Peak	χ^2	a/b
−53.519875(151)	308.007	703.651	592.21(77)	1.14	2.5501(295)
−53.518555(086)	308.748	704.364	590.03(85)	1.11	2.4602(511)
−53.506569(080)	308.010	703.657	573.97(85)	1.14	2.0508(220)
−53.505852(130)	308.270	703.946	574.50(81)	1.05	2.0568(315)
−53.494045(124)	308.294	703.913	558.70(75)	1.07	1.7244(294)
−53.492878(121)	308.765	704.387	556.16(75)	1.05	1.6690(270)
−53.481266(155)	307.990	703.658	539.39(80)	1.19	1.4086(159)
−53.480968(143)	308.549	704.144	539.33(79)	1.12	1.4002(172)
−53.468353(127)	307.775	703.460	523.54(74)	1.08	1.1993(097)
−53.468334(104)	307.910	703.553	522.85(78)	1.06	1.1894(112)
−53.455742(121)	307.778	703.437	503.86(78)	1.12	0.9825(082)
−53.455494(145)	307.899	703.538	505.09(77)	1.14	0.9937(088)
−53.443348(103)	307.452	703.140	488.18(84)	1.10	0.8408(165)
−53.442715(111)	308.283	703.880	487.20(80)	1.11	0.8257(096)
−53.430195(130)	307.901	703.504	469.94(78)	1.23	0.6938(069)
−53.428925(112)	308.462	704.068	469.45(83)	1.10	0.6862(079)
−53.418064(175)	307.435	703.110	456.11(85)	1.19	0.6019(083)
−53.404091(121)	307.664	703.277	436.68(79)	1.20	0.4839(055)
−53.403770(179)	308.433	704.046	434.78(81)	1.06	0.4692(077)
−53.391190(119)	308.009	703.648	417.71(83)	1.11	0.3837(061)
−53.391159(097)	307.269	702.920	418.17(74)	1.06	0.3895(036)
−53.379524(120)	306.375	702.145	401.96(88)	1.16	0.3184(342)
−53.365612(125)	309.495	705.014	381.25(71)	1.12	0.2216(310)
−53.353123(126)	309.149	704.558	363.49(79)	1.08	0.1593(201)

Table A.3: Ar^{16+} w automated fit results.

Crystal angle	Fiducial 1	Fiducial 2	x-ray Peak	χ^2	a/b
−51.008038(163)	307.476	703.046	605.30(62)	0.80	3.0467(349)
−51.007561(140)	307.554	703.115	603.12(63)	0.80	2.9559(344)
−50.992741(144)	308.296	703.796	585.62(59)	0.83	2.3467(845)
−50.992252(104)	307.706	703.266	582.69(63)	0.81	2.2806(193)
−50.978931(087)	307.409	702.955	564.72(62)	0.86	1.8614(447)
−50.978367(095)	307.376	702.970	563.57(64)	0.83	1.8379(149)
−50.963032(173)	307.552	703.145	543.14(63)	0.78	1.4723(176)
−50.962440(182)	307.574	703.153	542.43(61)	0.82	1.4612(104)
−50.949070(093)	307.191	702.767	523.97(62)	0.82	1.2124(082)
−50.947674(092)	307.755	703.326	522.71(64)	0.82	1.1902(086)
−50.933865(103)	307.371	702.934	503.45(63)	0.86	0.9829(080)
−50.933064(093)	308.079	703.616	502.32(64)	0.80	0.9650(109)
−50.918343(135)	307.961	703.481	481.19(61)	0.86	0.7793(108)
−50.917759(124)	308.005	703.541	481.30(64)	0.87	0.7798(069)
−50.904232(089)	307.451	702.990	461.94(65)	0.87	0.6409(051)
−50.903530(112)	307.964	703.498	461.43(64)	0.76	0.6340(129)
−50.889652(102)	307.539	703.086	441.02(63)	0.86	0.5093(057)
−50.888855(114)	307.228	702.771	440.97(65)	0.86	0.5109(039)
−50.875011(178)	307.212	702.775	422.75(62)	0.89	0.4126(057)
−50.874485(113)	306.805	702.369	422.41(64)	0.91	0.4129(033)
−50.859432(096)	307.637	703.190	401.50(67)	0.92	0.3111(042)
−50.858414(138)	306.980	702.548	401.34(64)	0.91	0.3133(029)
−50.843887(122)	307.652	703.187	378.93(65)	0.90	0.2198(031)

Table A.4: Ar^{16+} z automated fit results.

Crystal angle	Fiducial 1	Fiducial 2	x-ray Peak	χ^2	a/b
−50.467453(203)	308.719	704.024	594.04(69)	1.22	2.5943(452)
−50.466682(106)	308.069	703.609	593.79(74)	1.26	2.6017(250)
−50.450764(156)	308.359	703.894	570.59(75)	1.18	1.9672(171)
−50.450703(097)	308.303	703.841	570.99(72)	1.16	1.9774(168)
−50.436916(137)	307.704	703.247	550.27(73)	1.16	1.5856(143)
−50.436272(098)	308.071	703.599	550.48(74)	1.19	1.5831(128)
−50.422024(087)	307.352	702.883	530.58(72)	1.11	1.2955(099)
−50.421341(089)	307.967	703.516	529.44(73)	1.13	1.2723(097)
−50.406292(107)	308.019	703.540	509.75(70)	1.15	1.0410(106)
−50.405533(094)	307.833	703.375	509.57(74)	1.12	1.0409(081)
−50.391224(105)	307.511	703.050	488.91(71)	1.08	0.8471(066)
−50.390091(133)	308.145	703.666	487.16(79)	1.10	0.8268(070)
−50.375931(087)	306.944	702.469	467.83(72)	1.10	0.6857(440)
−50.375690(113)	308.217	703.712	467.65(77)	1.15	0.6754(074)
−50.360615(147)	307.718	703.248	447.19(72)	1.13	0.5447(045)
−50.359894(121)	307.306	702.821	446.84(71)	1.08	0.5451(056)
−50.344349(136)	307.476	702.970	424.40(69)	1.13	0.4197(040)
−50.344166(086)	308.199	703.707	423.82(72)	1.10	0.4131(050)
−50.330265(115)	306.165	701.662	405.11(74)	1.17	0.3336(209)
−50.329502(145)	307.879	703.380	403.98(80)	1.12	0.3210(036)
−50.313629(120)	307.423	702.954	384.12(72)	1.11	0.2406(042)
−50.313190(135)	308.148	703.659	381.44(71)	1.05	0.2275(028)
−50.299767(118)	307.637	703.139	362.59(73)	0.98	0.1614(029)

Table A.5: Cl^{16+} Lyman-α_1 automated fit results.

Crystal angle	Fiducial 1	Fiducial 2	x-ray Peak	χ^2	a/b
−48.193127(153)	306.891	702.241	634.87(75)	1.15	4.8680(1001)
−48.176998(104)	306.788	702.114	611.75(75)	1.11	3.3748(1399)
−48.158840(131)	306.756	702.105	586.38(78)	1.08	2.4163(0359)
−48.140285(150)	306.913	702.292	559.19(77)	1.20	1.7629(0183)
−48.124134(132)	306.627	701.993	538.94(80)	1.14	1.4248(0130)
−48.105335(125)	307.221	702.586	515.47(75)	1.06	1.1129(0121)
−48.088818(130)	307.470	702.790	491.45(73)	1.16	0.8706(0232)
−48.071758(135)	306.720	702.097	467.20(72)	1.19	0.6832(0060)
−48.053509(111)	306.599	702.005	441.87(80)	1.09	0.5200(0052)
−48.035744(169)	307.102	702.474	418.53(72)	1.16	0.3925(0060)
−48.019352(162)	307.121	702.467	397.06(86)	1.19	0.2945(0081)
−48.002071(267)	306.744	702.111	374.08(83)	1.20	0.2053(0054)
−47.984081(185)	306.848	702.226	347.35(75)	1.13	0.1141(0031)
−47.966194(169)	307.351	702.713	323.65(77)	1.13	0.0430(0086)
−47.949787(093)	306.660	702.034	301.82(79)	1.20	0.0121(0022)
−47.931141(097)	306.962	702.338	277.67(78)	1.01	0.0690(0018)

Bibliography

[AAM+88] Aglitsky, E.V. ; Antsiferov, P.S. ; Mandelstam, S.L. ; Panin, A.M. ; Safronova, U.I. ; Ulitin, S.A.: Comparison of Calculated and Measured Wavelengths of Resonance Transitions in He-Like Ions for $Z = 16 - 39$. In: *Phys. Scr.* 38 (1988), 136–142

[AGIS03] Anagnostopoulos, D.F. ; Gotta, D. ; Indelicato, P. ; Simons, L.M.: Low-Energy X-Ray Standards from Hydrogenlike Pionic Atoms. In: *Phys. Rev. Lett.* 91 (2003), 240801

[ALPS04] Andreev, O.Y. ; Labzowsky, L.N. ; Plunien, G. ; Soff, G.: Calculation of quasidegenerate energy levels of two-electron ions. In: *Phys. Rev. A* 69 (2004), 062505

[And33] Anderson, C.D.: The Positive Electron. In: *Physical Review* 43 (1933), 491–494

[Ang04] Angeli, I.: A consistent set of nuclear rms charge radii: properties of the radius surface $R(N, Z)$. In: *At. Data Nucl. Data Tables* 87 (2004), 185–206

[ASS+03] Artemyev, A.N. ; Shabaev, V.M. ; Sysak, M.M. ; Yerokhin, V.A. ; Beier, T. ; Plunien, G. ; Soff, G.: Evaluation of the two-photon exchange diagrams for the $(1s)^2 2p_{3/2}$ electron configuration in Li-like ions. In: *Phys. Rev. A* 67 (2003), 062506

[ASY+05] A.N.Artemyev ; Shabaev, V.M. ; Yerokhin, V.A. ; Plunien, G. ; Soff, G.: QED calculation of the $n = 1$ and $n = 2$ energy levels in He-like ionse. In: *Phys. Rev. A* 71 (2005), 062104

[BBP01] Bhatti, M.I. ; Bucardo, M. ; Perger, W.F.: MCDF calculations of the specific mass shift in helium-like ions. In: *J.Phys.B: At. Mol. Phys.* 34 (2001), 223–231

[BBT+05] Braun, J. ; Bruhns, H. ; Trinczek, M. ; Crespo López-Urrutia, J.R. ; Ullrich, J.: Novel technique for high-precision Bragg-angle determination in crystal x-ray spectroscopy. In: *Rev. Sci. Instrum.* 76 (2005), 073105

[BBvH89] Beiersdorfer, P. ; Bitter, M. ; von Goeler, S. ; Hill, K.W.: Experimental study of the x-ray transitions in the heliumlike isoelectronic sequence. In: *Phys. Rev. A* 40 (1989), 150–157

[BDFL85] Beyer, H.F. ; Deslattes, R.D. ; Folkmann, F. ; LaVilla, R.E.: Determination of the 1s Lamb shift in one-electron argon recoil ions. In: *J.Phys.B: At. Mol. Phys.* 18 (1985), 207–215

[Bec] Becker, P. Physikalisch technische Bundesanstalt (PTB), Braunschweig, Germany. private communication

[Bei05] Beiersdorfer, P. Lawrence Livermore National Laboratory, California. private communication. 2005

[BIF+91] Beyer, H.F. ; Indelicato, P. ; Finlayson, K.D. ; Liesen, D. ; Deslattes, R. D.: Measurement of the 1s Lamb shift in hydrogenlike nickel. In: *Phys. Rev. A* 43 (1991), January, Nr. 1, 223–227

[BJ03] Brandsen, B.H. ; Joachain, C.J.: *Physics of Atoms and Molecules.* second edition. Essex : Pearson Education Limited, 2003

[BKS97] Beyer, H.F. ; Kluge, H.-J. ; Shevelko, V.P. ; Springer (Hrsg.): *X-Ray Radiation of Highly Charged Ions.* 1. Berlin : Springer, 1997

[BMI+83] Briand, J.P. ; Mossé, J.P. ; Indelicato, P. ; Chevallier, P. ; Girard-Vernhet, D. ; Chetioui, A. ; Ramos, M.T. ; Desclaux, J.P.: Spectroscopy of hydrogenlike and heliumlike argon. In: *Phys. Rev. A* 28 (1983), September, Nr. 3, 1413

[Boh13] Bohr, N.: On the Constitution of Atoms and Molecules. In: *Philosophical Magazine* 26 (1913), July, Nr. 6, 1–25

[Boh14] Bohr, N.: The spectra of helium and hydrogen. In: *Nature* 92 (1914), 231–232

[Bon60] Bond, W.L.: Precision lattice constant determination. In: *Acta Cryst.* 13 (1960), 814

[Bra03] Braun, Johannes: "Entwicklung eines Kristallspektrometers für röntgenspektroskopische Untersuchungen an hochgeladenen Ionen", Universität Heidelberg, Diplomarbeit, 2003

[Bra06] Braun, Johannes: "Absolute Wellenlängenmessungen an elektronischen Übergängen in heliumartigen Ionen", Max-Planck-Institut für Kernphysik, Heidelberg, Diss., 2006

[BRF02] Biedermann, C. ; Radtke, R. ; Fournier, K.B.: Spectroscopy of heliumlike argon resonance and satellite lines for plasma temperature diagnostics. In: *Phys. Rev. E* 66 (2002), 066404

[CC00] Cheng, K.T. ; Chen, M. H.: Energy levels of the low-lying states of mid-Z heliumlike ions. In: *Phys. Rev. A* 61 (2000), 044503

[CCJS94] Cheng, K.T. ; Chen, M. H. ; Johnson, W.R. ; Sapirstein, J.: Relativistic configuration-interaction calculations for the ground state and $n = 2$ singlet states in heliumlike ions. In: *Phys. Rev. A* 50 (1994), Nr. 1, 247

[CGD+04] Cancio-Pastor, P. ; Giusfredi, G. ; De Natale, P. ; Hagel, G. ; de Mauro, C. ; Inguscio, M.: Absolute Frequency Measurement of the $2^3S_1 \rightarrow 2^3P_{0,1,2}$ Atomic Helium Transitions around 1083 nm. In: *Phys. Rev. Lett.* 92 (2004), 023001

[Che] Cheng, K.T. Lawrence Livermore National Laboratory, Livermore, USA. private communication

[CPH+00] Chantler, C.T. ; Paterson, D. ; Hudson, L.T. ; Serpa, F. G. ; Gillaspy, J. D. ; Takács, E.: Absolute measurement of the resonance line in heliumlike vanadium on an electron beam ion trap. In: *Phys. Rev. A* 62 (2000), 042501

[cxr] http://www-cxro.lbl.gov/

[DBF84] Deslattes, R.D. ; Beyer, H.F. ; Folkmann, F.: Precision x-ray wavelength measurements in helium-like argon recoil ions. In: *J.Phys.B: At. Mol. Phys.* 17 (1984), L689–L694

[Dem00] Demtröder, W. ; Verlag, Springer (Hrsg.): *Experimentalphysik 3: Atome, Moleküle und Festkörper*. 2. Berlin : Springer, 2000

[Dir28] Dirac, P.A.M.: The Quantum Theory of the Electron. In: *Proc. Roy. Soc.* A117 (1928), 610

[Dir30] Dirac, P.A.M.: A Theory of Electrons and Protons. In: *Proc. Roy. Soc.* A126 (1930), 360

[DK03] Deslattes, R.D. ; Kessler, E.G.: X-ray transition energies: new approach to a comprehensive evaluation. In: *Rev. Mod. Phys.* 75 (2003), 35–99

[Dra88] Drake, G.W.F.: Theoretical energies for the n=1 and 2 states of the helium isoelectronic sequence up to Z=100. In: *Can. J. Phys.* 66 (1988), 586

[Dra02] Drake, G.W.F.: Progress in helium fine-structure calculations and the fine-structure constant. In: *Can. J. Phys.* 80 (2002), 1195–1212

[Dra04] Drake, G.W.F. University of Windsor, Windsor, Canada. private communication. 2004

[DSJ85] Deslattes, R.D. ; Schuch, R. ; Justiniano, E.: Application of decelerated bare nuclei to precision spectroscopy of one-electron ions. In: *Phys. Rev. A* 32 (1985), 1911–1913

[EGS01] Eides, M.I. ; Grotch, H. ; Shelyuto, V.A.: Theory of light hydrogenlike atoms. In: *Physics Reports* 342 (2001), 63–261

[FFD$^+$02] Fischer, D. ; Feuerstein, B. ; DuBois, R.D. ; Moshammer, R. ; Crespo López-Urrutia, J.R. ; Draganic, I. ; Lörch, H. ; Perumal, A.N. ; Ullrich, J.: State-resolved measurements of single-electron capture in slow Ne^{7+}- and Ne^{8+}-helium collisions. In: *J. Phys. B: At. Mol. Opt. Phys.* 35 (2002), 1369–1377

[Fis04] Fischer, M.C.: *Höchstauflösende Laserspektroskopie an atomarem Wasserstoff*, LMU München, Diss., May 2004

[FKKM01] Flowers, J.L. ; Klein, H. A. ; Knight, D.J.E. ; Margolis, H.S. *Hydrogenic Systems for Calculable Frequency Standards: Status and Options.* NPL Report CBTLM 11. March 2001

[FKZ$^+$04] Fischer, M. ; Kolachevsky, N. ; Zimmermann, M. ; Holzwarth, R. ; Udem, T. ; Hänsch, T.W. ; Abgrall, M. ; Grünert, J. ; Maksimovic, I. ; Bize, S. ; Marion, H. ; Pereira Dos Santos, F. ; Lemonde, P. ; Santarelli, G. ; Laurent, P. ; Clairon, A. ; Salomon, C. ; Haas, M. ; Jentschura, U.D. ; Keitel, C.H.: New Limits on the Drift of Fundamental Constants from Laboratory Measurements. In: *Phys. Rev. Lett.* 92 (2004), 230802

[FLD+04] Fleischmann, A. ; Linck, M. ; Daniyarov, T. ; Rotzinger, H. ; Enss, C. ; Seidel, G.M.: Metallic magnetic calorimeters: detectors for high resolution x-ray spectroscopy. In: *Nucl. Instrum. Meth. A* 520 (2004), 27–33

[För] Förster, E. FSU Jena. private communication

[Gab72] Gabriel, A.H.: Dielectronic satellite spectra for highly-charged helium-like ion lines. In: *Mon. Not. R. Astron. Soc.* 160 (1972), 99

[GCB+05] González Martínez, A.J. ; Crespo López-Urrutia, J.R. ; Braun, J. ; Brenner, G. ; Bruhns, H. ; Lapierre, A. ; Mironov, V. ; Orts, R. S. ; Tawara, H. ; Trinczeck, M. ; Ullrich, J. ; Scofield, J.: Quantum interference observed in the recombination of highly charged $\mathrm{Hg}^{75+\dots78+}$ mercury ions in an electron beam ion trap. In: *Phys. Rev. Lett.* 94 (2005), May, 203201. – to be published

[GLN+01] Goidenko, I. ; Labzowsky, L. ; Nefiodov, A. ; Plunien, G. ; Soff, G. ; Zschocke, S.: Evaluation of the Two-Photon Self-Energy Correction for Hydrogenlike Ions. In: *Hyperfine Interactions* 132 (2001), 397–400

[Gon05] González Martínez, A.J.: Quantum interference in the dielectronic recombination of heavy highly charged ions, Universität Heidelberg, Diss., June 2005

[GSB+04] Gumberidze, A. ; Stöhlker, T. ; Banas, D. ; Beckert, K. ; Beller, P. ; Beyer, H.F. ; Bosch, F. ; Cai, X. ; Hagmann, S. ; Kozhuharov, C. ; Liesen, D. ; Nolden, F. ; Ma, X. ; Mokler, P.H. ; Orsic-Muthig, A. ; Steck, M. ; Sierpowski, D. ; Tashenov, S. ; Warczak, A. ; Zou, Y.: Electron-Electron Interaction in Strong Electromagnetic Fields: The Two-Electron Contribution to the Ground-State Energy in He-like Uranium. In: *Phys. Rev. Lett.* 92 (2004), 203004

[GSB+05] Gumberidze, A. ; Stöhlker, T. ; Banas, D. ; Beckert, K. ; Beller, P. ; Beyer, H.F. ; Bosch, F. ; Hagmann, S. ; Kozhuharov, C. ; Liesen, D ; Nolden, F. ; Ma, X. ; Mokler, P.H. ; Steck, M. ; Sierpowski, D. ; Tashenov, S.: Quantum Electrodynamics in Strong Electric Fields: The Ground-State Lamb Shift in Hydrogenlike Uranium. In: *Phys. Rev. Lett.* 94 (2005), 223001

[Har] Harney, H.L. Max-Planck-Institut für Kernphysik, Heidelberg, Germany. private communication

[Har03] Harney, H.L. ; Springer (Hrsg.): *Bayesian Inference.* 1. Berlin : Springer, 2003 (Advanced Texts in Physics)

[Hei26] Heisenberg, W.: Über quantentheoretische Umdeutung kinematischer und mechanischer Bewegungen. In: *Zeitschrift f. Physik* 33 (1926), 879–893

[Hei27] Heisenberg, W.: Über den anschaulichen Inhalt der quantentheoretischen Kinematik und Mechanik. In: *Zeitschrift f. Physik* 43 (1927), 172–198

[HFD$^+$97] Hölzer, G. ; Fritsch, M. ; Deutsch, M. ; Härtwig, J. ; Förster, E.: K$\alpha_{1,2}$ and K$\beta_{1,3}$ emission lines of the $3d$ transition metals. In: *Physical Review A* 56 (1997), December, Nr. 6, 4554

[HFK$^+$98] Hölzer, G. ; Förster, E. ; Klöpfel, D. ; Beiersdorfer, P. ; Brown, G. V. ; Crespo López-Urrutia, J.R. ; Widmann, K.: Absolute wavelength measurement of the Lyman-α transitions of hydrogenic Mg^{11+}. In: *Phys. Rev. A* 57 (1998), February, Nr. 2, 945–948

[JS85] Johnson, W.R. ; Soff, G.: The Lamb shift in hydrogen-like atoms, 1<Z<110. In: *At. Data Nucl. Data Tables* 33 (1985), Nr. 2, 405–446

[KHFB97] Klöpfel, D. ; Hölzer, G. ; Förster, E. ; Beiersdörfer, P.: A quartz quasimonolith for absolute x-ray wavelength measurements. In: *Rev. Sci. Instrum.* 68 (1997), July, 3669–3675

[KKRS84] Källne, E. ; Källne, J. ; Richard, P. ; Stöckli, M.: Precision measurement of the H-like x-ray spectrum of Cl and the 1s Lamb shift. In: *J. Phys. B.: At. Mol. Phys.* 17 (1984), L115–L120

[LASM01] Lindgren, I. ; Asen, B. ; Salomonson, S. ; Martensson-Pendrill, A.M.: QED procedure applied to the quasidegenerate finestructrue levels of He-like ions. In: *Phys. Rev. A* 64 (2001), 062505

[Leo93] Leo, W.R. ; Springer (Hrsg.): *Techniques for Nuclear and Particle Physics Experiments.* 2. New York : Springer, 1993

[LJ$^+$] LaPierre, A. ; ; Jentschura, U.D. ; Crespo López-Urrutia, J.R. ; Braun, J. ; Brenner, G. ; Bruhns, H. ; Fischer, D. ; González Martínez, A.J. ; Harman, Z. ; Johnson, W.R. ; Keitel, C.H. ; Mironov, V. ; Osborne, C.J. ; Sikler, G. ; Soria Orts, R. ;

TAWARA, H. ; TUPITSYN, I.I. ; ULLRICH, J. ; VOLOTKA, A.: *Relativistic Electron Correlation, Quantum Electrodynamics and the Lifetime of the* $1s^2 2s^2 2p^2 P^0_{3/2}$ *Level in Boronlike Argon.* – to be published in Phys. Rev. Lett.

[LPS95] LINDGREN, I. ; PERSSON, H. ; SALOMONSON, S.: Full QED calculations of two-photon exchange for heliumlike-systems: Analysis in the Coulomb and Feynman gauges. In: *Phys. Rev. A* 51 (1995), 1167–1195

[LR47] LAMB, W.E. ; RETHERFORD, R. C.: Fine Structure of the Hydrogen Atom by a Microwave Method. In: *Physical Review* 72 (1947), 241–243

[MBV⁺92] MACLAREN, S. ; BEIERSDORFER, P. ; VOGEL, D.A. ; KNAPP, D. ; MARRS, R.E. ; WONG, K. ; ZASADZINSKI, R.: Precision measurement of the $K\alpha$ transitions in heliumlike Ge^{30+}. In: *Phys. Rev. A* 45 (1992), 329–332

[MES95] MARRS, R.E. ; ELLIOT, S.R. ; STÖHLKER, T.: Measurement of two-electron contributions to the ground-state energy of heliumlike ions. In: *Phys. Rev. A* 52 (1995), 3577–3585

[Moh85] MOHR, P.J.: Quantum electrodynamics of high-Z few-electron atoms. In: *Phys. Rev. A* 32 (1985), 1949–1957

[MPS98] MOHR, P.J. ; PLUNIEN, G. ; SOFF, G.: QED corrections in heavy atoms. In: *Phys. Rep.* 293 (1998), 227–369

[MRK⁺86] MARMAR, E.S. ; RICE, J.E. ; KÄLLNE, E. ; KÄLLNE, J. ; LAVILLA, R.E.: Precision measurement of the $1s$ Lamb shift in hydrogenlike argon. In: *Phys. Rev. A* 33 (1986), January, Nr. 1, 774–777

[MT00] MOHR, P.J. ; TAYLOR, B.N.: CODATA Recommended Values of the Fundamental Physical Constants: 1998. In: *Reviews of Modern Physics* 72 (2000), Nr. 2, 351–495

[MWD⁺04] MUELLER, P. ; WANG, L.-B. ; DRAKE, G.W.F. ; BAILEY, K. ; LU, Z.-T. ; O'CONNOR, T.P.: *Fine Structure of the* $1s3p\,{}^3P_J$ *Level in Atomic* ^{4}*He: Theory and Experiment.* 2004. – arxiv.org/pdf/physics/0407114

[NHR⁺00] NIERING, M. ; HOLZWARTH, R. ; REICHERT, J. ; POKASOV, P. ; UDEM, T. ; WEITZ, M. ; HÄNSCH, T.W. ; LEMONDE, P. ; SANTARELLI, G. ; ABGRALL, M. ; LAURENT, P. ; SALOMON, C. ; CLAIRON, A.: Measurement of the Hydrogen $1S-2S$ Transition Frequency by Phase Coherent

Comparison with a Microwave Cesium Fountain Clock. In: *Phys. Rev. Lett.* 84 (2000), 5496–5499

[NLPS96] Nefiodov, A. V. ; Labzowsky, L. N. ; Plunien, G. ; Soff, G.: Nuclear polarization effects in spectra of multicharged ions. In: *Phys. Lett. A* 222 (1996), 227–232

[PJS94] Plante, D.R. ; Johnson, W.R. ; Sapirstein, J.: Relativistic all-order many-b ody calculations of the n=1 and n=2 states of heliumlike ions. In: *Phys. Rev. A* 49 (1994), May, Nr. 5, 3519–3530

[PS03] Pachucki, K. ; Sapirstein, J.: Higher-Order recoil corrections to helium fine structure. In: *J. Phys. B: At. Mol. Opt. Phys.* 36 (2003), 803–809

[PSS$^+$97] Persson, H. ; Salomonson, S. ; Sunnergren, P. ; Lindgren, I. ; Gustavsson, M.G.H.: A theoretical survey of QED tests in highly charged ions. In: *Hyperfine Interactions* 108 (1997), 3–17

[RSD$^+$84] Richard, P. ; Stöckli, M. ; Deslattes, R.D. ; Cowan, P. ; LaVilla, R.E. ; Johnson, B. ; Jones, K. ; Meron, M. ; Mann, R. ; Schartner, K.: Measurement of the 1s Lamb shift in hydrogenlike chlorine. In: *Phys. Rev. A* 29 (1984), 2939–2942

[SAB$^+$98] Shabaev, V.M. ; Artemyev, A. N. ; Beier, T. ; Plunien, G. ; Yerokhin, V. A. ; Soff, G.: Recoil correction to the ground-state energy of hydrogenlike atoms. In: *Phys. Rev. A* 57 (1998), 4235–4239

[SBB$^+$82] Schleinkofer, L. ; Bell, F. ; Betz, H.-D. ; Trollmann, G. ; Rothermel, J.: Precision wavelength determination of $2\ ^1P_1 - 1\ ^1S_0$ and $2\ ^3P_1 - 1\ ^1S_0$ transitions in helium-like sulfur ions. In: *Phys. Scr.* 25 (1982), 917

[Sch26] Schrödinger, E.: An undolatory theory of the mechanics of atoms and molecules. In: *Physical Review* 28 (1926), Nr. 6, 1049–1070

[Sha90] Shabaev, V.M.: Rayleigh-Schrödinger perturbation theory for a relativistic atom. In: *Theor. Math. Phys.* 82 (1990), 57–62

[Sha93a] Shabaev, V.M.: Finite nuclear size corrections to the energy levels of the multicharged ions. In: *J. Phys. B* 26 (1993), 1103–1108

[Sha93b] Shabaev, V.M.: Schrödinger-like equation for the relativistic few-electron atom. In: *J. Phys. B* 26 (1993), 4703–4718

[Sha02] Shabaev, V.M.: Two-time Green's function method in quantum electrodynamics of high-Z few-electron atoms. In: *Physics Reports* 356 (2002), 119–228

[Sor05] Soria Orts, R.: *Isotopic effect of B-like and Be-like argon ions*, Universität Frankfurt, Diss., 2005

[SOT+04] Shigeoka, N. ; Oohashi, H. ; Tochio, T. ; Ito, Y. ; Mukoyama, T. ; Vlaicu, A. M. ; Fukushima, S.: Experimental investigation of the origin of the Ti Kα'' satellites. In: *Phys. Rev. A* 69 (2004), May 2004, 052505

[TBB+04] Trassinelli, M. ; Biri, S. ; Boucard, S. ; Covita, D.S. ; Gotta, D. ; Leoni, B. ; Hirtl, A. ; Indelicato, P. ; Le Bigot, E.-O. ; dos Santos, J.M.F. ; Simons, L.M. ; Stingelin, L. ; Veloso, J.F.C.A. ; Wasser, A. ; Zmeskal, J.: *High Resolution He-like Argon And Sulfur Spectra From The PSI ECRIT.* 2004. – to be published, http://www.oeaw.ac.at/smi/download/0410250.pdf - arXiv:physics/0410250

[TBPS01] Tarbutt, M.R. ; Barnsley, R. ; Peacock, N.J. ; Silver, J.D.: Wavelength measurements of the satellite transitions to the $n = 2$ resonance lines of helium-like argon. In: *J. Phys. B: At. Mol. Opt. Phys.* 34 (2001), 3979–3991

[TCH87] Thompson, P. ; Cox, D.E. ; Hastings, J.B.: Rietveld refinement of Debye-Scherrer synchrotron X-ray data from Al_2O_3. In: *J. Appl. Cryst.* 20 (1987), 79–83

[TCM+00] Tarbutt, M.R. ; Crosby, D. ; Myers, E.G. ; Nakamura, N. ; Ohtani, S. ; Silver, J.D.: X-ray spectroscopy of hydrogen-like ions in an electron beam ion trap, proceedings of the Hydrogen atom II meeting, 2000

[TKB+02] Tschischgale, J. ; Klöpfel, D. ; Beiersdorfer, P. ; Brown, G.V. ; Förster, E. ; Schulte-SChrepping, H. ; Utter, S.B.: Absolute wavelength measurement of the Lyman-α transition of hydrogen-like silicon. In: *Can. J. Phys.* 80 (2002), 867–874

[WBDB96] Widmann, K. ; Beiersdorfer, P. ; Decaux, V. ; Bitter, M.: Measurements of the Kα transition energies of heliumlike krypton. In: *Phys. Rev. A* 53 (1996), 2200–2205

[YAB$^+$03] YEROKHIN, V.A. ; ARTEMYEV, A. N. ; BEIER, T. ; GOIDENKO, I. A. ; LABZOWSKY, L. N. ; NEFIODOV, A. V. ; PLUNIEN, G. ; SHABAEV, V. M. ; SOFF, G.: Towards tests of QED in Lamb-shift measurements of highly charged ions. In: *X-Ray Spectrom.* 32 (2003), Nr. 2, 83–88

[YD95] YAN, Z.-C. ; DRAKE, G.W.F.: High Precision Calculation of Fine Structure Splittings in Helium and He-Like Ions. In: *Phys. Rev. Lett.* 74 (1995), 4791–4794

Acknowledgements

Zunächst möchte ich Prof. Ullrich dafür danken, daß ich diese Arbeit in seiner Gruppe durchführen konnte. Ganz abgesehen von den vielen guten Fragen, Ratschlägen und Erklärungen, die eigentlich immer punktgenau sassen, denke ich insbesondere an ein spontanes, längeres Gespräch gegen Ende des ersten Jahres, das mich trotz anfänglicher Rückschläge dazu ermutigte, die Arbeit zu Ende zu führen.

José danke ich dafür, daß er immer mit Rat und Tat zur Stelle war und wesentlich dazu beigetragen hat, daß das Projekt auch über die in dieser Arbeit geschilderten Messungen hinaus beste Aussichten auf eine erfolgreiche Zukunft hat.

Unseren Feinmechanikern Herrn Bechberger und Herrn Müller und unserem Elektroniker Herrn Busch möchte ich für ihre stets schnelle und hochwertige Arbeit danken.

Ich danke Zoltan für eine stets offene Tür bei Fragen zur theoretischen Physik, die er immer geduldig und verständlich beantwortete.

Ohne Johannes hätte es die neue Methode der Positionsreferenz nicht gegeben, und wir wären ohne ihne heute nicht kurz davor, Absolutmessungen von Wellenlängen durchzuführen. In einem Satz gesagt: seine Mitarbeit am Spektrometer war unverzichtbar - und alles weitere bereden wir mal an einem ruhigen Wochenende auf der Terrasse vor seiner Gartenhütte. Danke.

Von Beginn an hat Karl mich durch das Studium begleitet. Abgesehen von dem einen oder anderen guten Vorschlag zum Spektrometer möchte ich mich an dieser Stelle hauptsächlich für seine langjährige Freundschaft bedanken.

Der gesamten Ullrich-Gruppe gilt mein Dank für ein tolles Arbeitsklima. Wann immer man hier eine helfende Hand braucht, bekommt man sie sofort.

Meiner Familie möchte ich für ihre Unterstützung und Zuneigung danken, aber auch für die Freiheit, daß ich mir meine Ziele immer selbst wählen konnte.

Zu guter Letzt danke ich Ramona für ihre Liebe und die vielen Freuden, die mir das Leben so lebenswert machen.

Erklärung

Ich versichere, dass ich diese Arbeit selbständing verfaßt und keine anderen als die angegebenen Quellen und Hilfsmittel benutzt habe.

Heidelberg, den November 2005

Hjalmar Bruhns